

DOI: [10.29026/oes.2022.220006](https://doi.org/10.29026/oes.2022.220006)

Perovskite-transition metal dichalcogenides heterostructures: recent advances and future perspectives

Ahmed Elbanna^{1,2†}, Ksenia Chaykun^{3†}, Yulia Lekina^{2,4}, Yuanda Liu¹, Benny Febriansyah⁶, Shuzhou Li⁵, Jisheng Pan¹, Ze Xiang Shen^{2,3,4*} and Jinghua Teng^{1*}

Transition metal dichalcogenides (TMDs) and perovskites are among the most attractive and widely investigated semiconductors in the recent decade. They are promising materials for various applications, such as photodetection, solar energy harvesting, light emission, and many others. Combining these materials to form heterostructures can enrich the already fascinating properties and bring up new phenomena and opportunities. Work in this field is growing rapidly in both fundamental studies and device applications. Here, we review the recent findings in the perovskite-TMD heterostructures and give our perspectives on the future development of this promising field. The fundamental properties of the perovskites, TMDs, and their heterostructures are discussed first, followed by a summary of the synthesis methods of the perovskites and TMDs and the approaches to obtain high-quality interfaces. Particular attention is paid to the TMD-perovskite heterostructures that have been applied in solar cells and photodetectors with notable performance improvement. Finally through our analysis, we propose an outline on further fundamental studies and the promising applications of perovskite-TMD heterostructures.

Keywords: transition metal dichalcogenides; perovskites; heterostructures; photodetectors; solar cells; 2D materials

Elbanna A, Chaykun K, Lekina Y, Liu YD, Febriansyah B et al. Perovskite-transition metal dichalcogenides heterostructures: recent advances and future perspectives. *Opto-Electron Sci* **1**, 220006 (2022).

Introduction

Hybrid and metal lead halide perovskites have recently attracted a lot of attentions in both academy and industry. Performance of perovskite-based solar cell is pro-

gressing much faster than that of other types of photovoltaics and has reached an energy conversion efficiency of up to 25.2%¹⁻¹³. Moreover, perovskite materials have been shown to be promising for photodetectors

¹Institute of Materials Research and Engineering, Agency for Science, Technology and Research (A*STAR), 2 Fusionopolis Way, Singapore 138634, Singapore; ²Division of Physics and Applied Physics, School of Physical and Mathematical Sciences, Nanyang Technological University, 50 Nanyang Avenue, Singapore 637371, Singapore; ³Interdisciplinary Graduate Program, Energy Research Institute@NTU, Nanyang Technological University, 50 Nanyang Avenue, Singapore 639798, Singapore; ⁴The Photonics Institute and Center for Disruptive Photonic Technologies, Nanyang Technological University, 50 Nanyang Avenue, Singapore 639798 Singapore; ⁵School of Materials Science and Engineering, Nanyang Technological University, 50 Nanyang Avenue, Singapore 639798, Singapore; ⁶Berkeley Educational Alliance for Research in Singapore (BEARS), Ltd., 1 CREATE Way, Singapore 138602, Singapore.

[†]These authors contributed equally to this work.

*Correspondence: ZX Shen, E-mail: zexiang@ntu.edu.sg; JH Teng, E-mail: jh-teng@imre.a-star.edu.sg

Received: 21 March 2022; Accepted: 16 June 2022; Published online: 4 August 2022



Open Access This article is licensed under a Creative Commons Attribution 4.0 International License.

To view a copy of this license, visit <http://creativecommons.org/licenses/by/4.0/>.

© The Author(s) 2022. Published by Institute of Optics and Electronics, Chinese Academy of Sciences.

(PDs)^{14–22}, field-effect transistors (FETs)²³, X-ray detectors^{24,25}, spintronics²⁶, batteries²⁷, light-emitting diodes (LEDs)^{6,28–34}, and lasers^{35–39}. Altering the composition allows tuning the band gap and optical properties of the perovskites^{2,28,40}. However, poor moisture and illumination stability of regular three-dimensional (3D) hybrid organic-inorganic perovskites remain the main obstacle to fabricate the low-cost and long-running devices^{6,26}. Two-dimensional (2D) perovskites have demonstrated better stability, extended chemical engineering capability and better control of the properties such as bandgap, conductivity, and spin-related effects, which are more promising for the next generation solar energy-harvesting^{41–45} and light emitting^{26,45–51}. On the other side, transition metal dichalcogenides (TMDs) have also attracted tremendous interests and shown great potential in many applications including PDs^{52–55}, FETs⁵⁶, LEDs^{57–60}, lasers^{61–67}, and photovoltaic devices^{68–70}. The 2D heterostructures (HSs) create atomically thin p–n junctions and bring up possibilities on non-linearity, many-body phenomenon, polaritons, interlayer valley excitons, Moiré superlattice, etc^{71–80}, and broaden the application scenarios^{72,73}. However, due to their atomic-scale thickness, the light absorption of TMDs is limited^{81,82}.

Combining the various hybrid halide perovskites with TMDs to form HSs provides a way to extend the already fascinating properties of the components and complement each other for novel or improved performance. For instance, the TMDs can encapsulate the perovskites to improve the poor environmental stability of the latter^{83,84}. Interestingly, unlike the pure TMDs HSs, perovskite/TMD HSs do not require accurate lattice match nor rotational alignment due to the soft perovskite lattice, which simplifies the fabrication^{85,86}. TMDs and perovskite normally form a type-II heterojunction with good charge carrier transfer and strong coupling between the layers^{85,87,88}. Recently, the integration of perovskite and TMDs has stimulated interest in multidisciplinary areas and holds great promise for many optoelectronic applications^{89–94}. Particularly, combining the two materials together may improve the optical response of the sensitizing optical devices^{93,95}.

The quickly growing number of works in this field requires a summary of the recent findings. There have been several reviews on various perovskites and 2D materials HSs published recently^{96–102}. However, in a rapidly developing field, reviews quickly become outdated. In addition, many of the reviews focus only on one as-

pect of the HSs such as perovskite-graphene or one of the possible applications, while the intriguing and promising perovskite-TMD HSs are rarely reviewed. In this paper we will review both the fundamentals and the latest development of this fast-growing field of perovskite-TMDs HSs. In the first part, we briefly discuss the fundamental properties of the perovskites and TMDs and their respective HSs. More attention is paid to the unique properties of the perovskite/TMD HSs, particularly the band alignment, interlayer charge and energy transfer. Synthesis of perovskites and TMDs is introduced with a more detailed description on the preparation of perovskite/TMD HSs, followed by the device applications especially on PDs and solar cells. Finally, the perspectives and challenges for the research and development of perovskite/TMDs HSs are outlined.

Fundamental properties

The optoelectronic properties of materials and their HSs directly depend on the electronic band structures. Based on the nature of the components, HSs can be classified as metal-semiconductor, semiconductor-semiconductor, and insulator-semiconductor. Since semiconductors are promising for optoelectronic applications, perovskites and TMDs related to them will be considered in our review. Therefore, HSs of the semiconductor-semiconductor type are meant below. Due to the difference in electronic affinity in the contacting semiconductors, the conduction band minimum (CBM) and the valence band maximum (VBM) of the two respective constituent semiconductors may not coincide at the same level, a gap will be formed giving rise to three types of band alignments, as shown in Fig. 1(a)¹⁰³.

Type I: the straddling gap occurs when both the CBM and VBM of one semiconductor are located between the conduction and valence bands of the other one, respectively.

Type II: the staggered gap is formed when one of the band discontinuities is positive and the other is negative.

Type III: the broken gap formation is similar to the type II, but the overall band gap disappears. This happens when the VBM of one component is higher than the CBM of the other one.

Conventional halide perovskites are semiconductors whose band gaps most often lie in the range from 1.2 to 2.4 eV¹⁰⁴, while 2D TMDs have tunable band gaps in the range from 1.0 to 2.1 eV. Based on first-principles calculations, the interface between the halide perovskite and

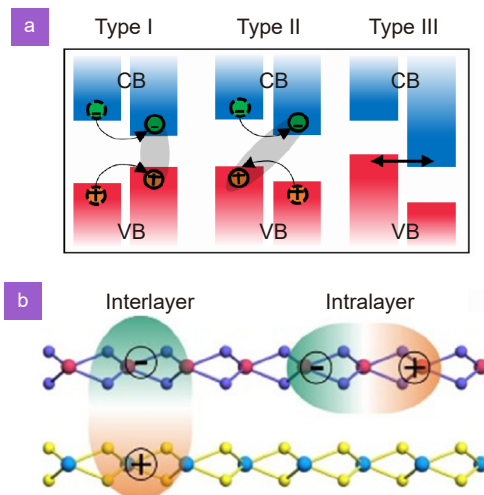


Fig. 1 | (a) Schematic diagram showing the band alignment in type I, II, and III heterostructures. Charge carriers are indicated by circles: green - electrons, orange - holes. Arrows - directions of charge transfer. (b) Schematic of intra- and interlayer excitons. For interlayer excitons, the electron and the hole are spatially separated into two layers.

TMD is mostly a type-II heterojunction, which is in favor of separating charge carriers^{87,88} and can help to improve the performance of e.g. PDs or solar cells over the constituent materials of perovskite or TMD alone, or to add a new property. Table 1 shows some of the notable examples of the perovskite and TMD HSs with significant performance improvement. As seen in Table 1, for PDs, orders of magnitude enhancement of the external quantum efficiency (EQE) and detectivity have been demonstrated using perovskite/TMD HSs. In addition, perovskite/TMD HSs exhibited a great enhancement in the stability of perovskite solar cells. We will briefly review the properties of the TMD and perovskite material and then give a more detailed discussion on the properties of the HSs.

TMDs and their heterostructures

Many of TMDs are semiconductors in nature with a finite bandgap and structure of MX_2 (where M could be Mo, W, Hf; X could be S, Se, Te)^{105–108}. The bandgaps of the majority of TMDs transit from indirect in few layers to direct in monolayers, featuring tightly quantum-confined exciton dynamics and strongly correlated electronic states. The deterministic layer transferring technique allows the preparation of component layers separately and following assembly to form van der Waals (vdWs) HSs. Up to now, there is a vast library of 2D materials including superconducting NbSe₂, semimetal graphene, insulating h-BN (Hexagonal Boron Nitride), magnetic CrI₃, and semiconducting TMDs and BP (Black Phosphorus). The change of surrounding environment caused by the contact with another 2D material can have a profound effect on its electronic structure, leading to carrier redistribution, formation of bounded interlayer excitons and strongly correlated electronic states^{107,109}. Besides, ultrafast charge transfer process has been observed in photoexcited staggered HSs^{110–112}. Femtosecond pump-probe spectroscopy of MoS₂/WS₂ heterobilayer discovered that the holes in the MoS₂ layer transfer to the WS₂ layer within 50 fs after being created by photon excitation¹¹⁰. The femtosecond charge transfer rate provides a promising route for applications that need ultrafast spatial separation of the electrons and holes, for instance, photodetection.

The Coulomb attraction between the electrons in one layer and the holes in another layer results in interlayer excitons (Fig. 1(b)). Due to the energy level offset, the interlayer excitons lie energetically lower than the intralayer excitons. The formation of interlayer exciton has enriched the fascinating exciton physics and provided an atomically thin 2D platform for exploring exciton

Table 1 | Some examples of improved properties by exploiting the heterostructures of perovskite/TMDs.

Heterostructure	Application	Heterostructure advantages	Ref.
CH ₃ NH ₃ PbI ₃ /WSe ₂	PD	External quantum efficiency (%): 3 orders of magnitude enhancement. WSe ₂ : 0.2–5.0 Heterostructure: 999	ref. ²²¹
(PEA) ₂ SnI ₄ /MoS ₂	PD	Detectivity (Jones): 2 orders of magnitude enhancement. (PEA) ₂ SnI ₄ : 5×10 ⁸ Heterostructure: 4×10 ¹⁰	ref. ²⁴³
(PEA) ₂ PbI ₄ /MoS ₂	PD	Detectivity (Jones): 2 orders of magnitude enhancement. MoS ₂ : 8.57×10 ¹¹ Heterostructure: 1.06×10 ¹³	ref. ¹⁵⁸
CH ₃ NH ₃ PbI ₃ /MoS ₂	Solar cell	Lifetime stability after 550 h ($\Delta\eta/\eta$, %): CH ₃ NH ₃ PbI ₃ : -34% Heterostructure: -7%	ref. ³⁰¹

dynamics and developing excitonic devices^{61,112–116}. The photoactive wavelength range of the HSs is determined by the band-energy alignment of the component monolayers, the crystal orientation alignment, and the separation distance of the two layers. For example, Fig. 2 shows the low frequency Raman spectra as well as the PL spectra of MoSe₂/WSe₂ HS without (Fig. 2(a, b)) and with (Fig. 2(c)) inserting dielectric monolayer of h-BN⁸⁶. The observation of the shear mode (SM) and layer-breathing mode (LBM) of the HS as a function of twisting angles indicate the high coupling between the individual materials at specific angles (Fig. 2(a)) which is not observed in the case of inserting 1L h-BN (MoSe₂/1L h-BN/WSe₂ HSs) due to the reduced coupling. Fig. 2(b) shows the PL spectra of MoSe₂/WSe₂ HSs measured at different twisting angles, which exhibit lower energy interlayer exciton peak at specific angles due to the stronger coupling. In contrast, in case of using 1L h-BN (Fig. 2(c)) the interlayer exciton peak disappeared due to the reduced coupling which was further confirmed by the comparable PL intensities of MoSe₂/1L h-BN/WSe₂ HSs and single individual materials (i.e. the PL is combination of both individual material due to the reduced coupling in case of using h-BN). Besides, the selection of the parent materials enables the bandgap engineering from visible to near-infrared (IR) and mid-IR^{66,117,118}. Moreover, the ultrafast charge transfer process separates the photogenerated electrons and holes resulting in less intersection of their wave functions relative to intralayer excitons and sup-

pressed the electron-hole (e–h) interaction, which gives rise to a long interlayer exciton lifetime, for instance, ~1.8 ns observed in MoSe₂/WSe₂ hetero-bilayer¹¹⁹. Furthermore, the interlayer exciton binding energy in 2D HSs is large and over 100 meV, which has enabled the observation of high-temperature exciton dynamics, for example, the Bose-Einstein exciton condensation in MoSe₂/WSe₂¹¹⁹. Additionally, HSs exhibit valley polarization behavior, inheriting from their monolayer components. The spin-valley locking renders an extremely long valley lifetime (40 μs for MoSe₂/WSe₂)¹²⁰. Applying an electrostatic gate voltage is capable to tune the concentration of both electrons and holes in 2D layers and the band energy alignment can be changed individually through biasing individual layers^{119,120}. Besides, recent understanding of moiré interlayer excitons localized in moiré superlattice opens a door to novel correlated states, for example, charge density waves, fractional Chern insulators, stripe phases, and Wigner crystals^{121–125}. Potential applications of interlayer excitons in TMDs HSs appear myriad, with examples demonstrated include ultra-low threshold lasing emission^{66,126,127}, broad-band photodetection^{117,128–132}, exciton transistors^{133–139} and valleytronic devices¹⁴⁰.

Perovskites and their heterostructures

Besides well known for their high efficiency and low cost in solar cell applications¹⁴¹, halide perovskites have also been utilized in LEDs^{6,28–30}, photodetectors^{14,15},

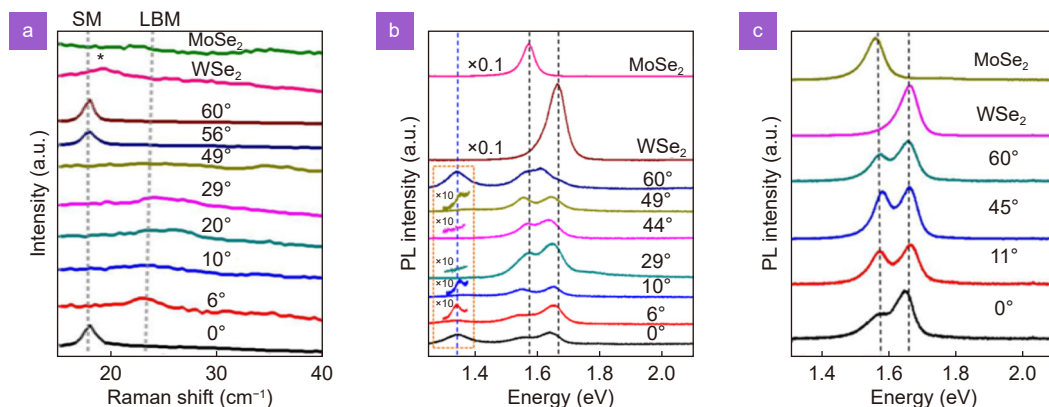


Fig. 2 | TMD/TMD heterostructure. (a) Low frequency Raman spectra of MoSe₂/WSe₂ HSs and individual TMD layers with different twist angles ($0^\circ \leq \theta \leq 60^\circ$) showing the shear mode (SM), layer-breathing mode (LBM), and unassigned peak (marked with asterisk). The pronounced SM at specific twisting angles indicating the strong coupling of the HS at those angles. (b) PL spectra of the same HS showing the emergence of the interlayer exciton peak at ~1.35 eV as a function of different twisting angles. (c) PL spectra of 1L MoSe₂, 1L WSe₂, and 1L h-BN-inserted HSs with various twist angles ($0^\circ \leq \theta \leq 60^\circ$) showing the absence of the interlayer exciton peak at all twisting angles indicating the reduced coupling between MoSe₂ and WSe₂. The intensity of the main peaks at the HS are comparable to individual layers further indicating the PL spectra is a combination of each individual material in case of no coupling. Figure reproduced with permission from ref.⁸⁶, Copyright © 2017, American Chemical Society.

spintronics²⁶, batteries²⁷, laser³⁹, etc. The large variety of applications is facilitated by the outstanding tunability of the composition of the halide perovskites^{2,142}. Three-dimensional (3D) halide perovskites follow a general formula ABX_3 , where X is a halide (I, Br, Cl or a mixture), B is a metal cation (usually Pb, or Sn, Ge, Bi, Mn and others), A is another cation, larger than B, which can be a metal (Cs, Ag, etc.) or an organic one (MA = CH_3NH_3 or FA = NH_2CHNH_2). The A cations are located in the cuboctahedra cavities formed by the corner-sharing BX_6 octahedral network. Altering the composition allows for obtaining a variety of materials with the desirable properties for different applications¹⁴³.

However, intrinsic poor environmental stability remains a limitation for the wider commercialisation of the halide perovskite materials¹⁴³. Creating low-dimensional perovskites is one of the ways to address this problem^{144–146}. Low-dimensional perovskites are obtained by incorporating long organic cations into the perovskite structure. In this case, the perovskite inorganic octahedra form 2D layers, 1D wires, or 0D quantum dots, separated by usually insulating organic layers^{6,26}. As a result, the material exhibits effectively low-dimensional properties, such as confinement effect, stable excitons and others. Extended chemical engineering possibilities allow control of the functional properties, such as bandgap, light emission, conductivity, or spin-related effects^{2,28,40}. The flexibility in property tuning and the improved stability over their 3D counterparts make the low-dimensional perovskites promising materials for applications in various technologically important areas^{26,41,50,51,42–49}.

In 2D perovskites, the layers are held together by weak vdWs interactions between the organic cations. Atomically thin layers can be obtained by solution techniques¹⁴⁷ or by mechanical exfoliation^{148,149}. This brings up the question of whether perovskite layers can form HSs, and the answer is yes. The multidimensional perovskites are HSs in nature, consisting alternate perovskite sheets of different thicknesses, such as 1, 2, 3, and so on perovskite octahedral layers within one sheet¹⁴⁴. They are used in perovskite solar cells to improve environmental stability^{145,146}, in which the interlayer charge transfer is critical¹⁵⁰. Thus, the processes at the perovskite layer interfaces are very important and require additional studies.

Overall, unlike the TMD HSs, the perovskite HSs are much less studied. The preparation of nano-sized HSs

with atomically sharp interfaces is complicated by the intrinsic ion mobility, where incorporating rigid aromatic organic cations suppresses anion diffusion. E. Shi et. al. succeeded in synthesizing various lateral HSs based on such 2D perovskites using solution drop-casting technique¹⁵¹. Vertical HSs with atomically sharp interfaces were first reported in 2018, synthesized by solution grows method¹⁵⁰. Such disorder primarily affects PL, which manifests itself in different spectra and colors of HSs from sample to sample (Fig. 3(a, b and c)). In this case, the organic layers act as a natural barrier to prevent interlayer ion diffusion. The disadvantage of this method is that one can only control the ratio of the components, while the order remains uncontrollable. In fact, it yields multi-dimensional perovskites discussed above. High-quality well controlled vertical perovskite HSs were reported recently in 2021¹⁵². The thin perovskite layers were independently synthesized and then transferred to the substrate and combined by the mechanical exfoliation method.

In the vertical HS, the internal energy transfer from the wider- to narrower band gap layers stays efficient despite the insulating nature of the organic layer¹⁵⁰. This could be explained by a simple emission-reabsorption process. Interestingly, however, charge transfer was reported to be possible across the organic layer in the vertical perovskite HSs. Kuo et al. demonstrated that free carriers can transfer across the heterojunction of 3D/2D perovskite both experimentally and by modelling¹⁵³. Charge and chirality transfer in 2D/3D perovskite HS was applied to create a highly sensitive circular polarization photodetector¹⁵⁴. The “transparency” of the interface is an unexpected phenomenon, which is useful for the TMD/perovskite HSs as well.

Perovskite/TMD heterostructures

Overall monolayer TMDs were reported to exhibit strong coupling with the 2D perovskites with type II band alignment⁸⁵, suitable for separating charge carriers^{87,88}. Except for the single layer, most TMDs are normally indirect bandgap semiconductors with very poor photoluminescence efficiency⁹⁶. By making perovskite-TMD HS, Yang et al. observed significant, up to 150-fold, enhancement of emission from 2D perovskite- WS_2 few-layer HS (Fig. 4(a))⁹³. At the same time, the top few WS_2 layers protect the perovskites from degradation. Using the first-principles calculations, the authors demonstrated the existence of charge transfer between

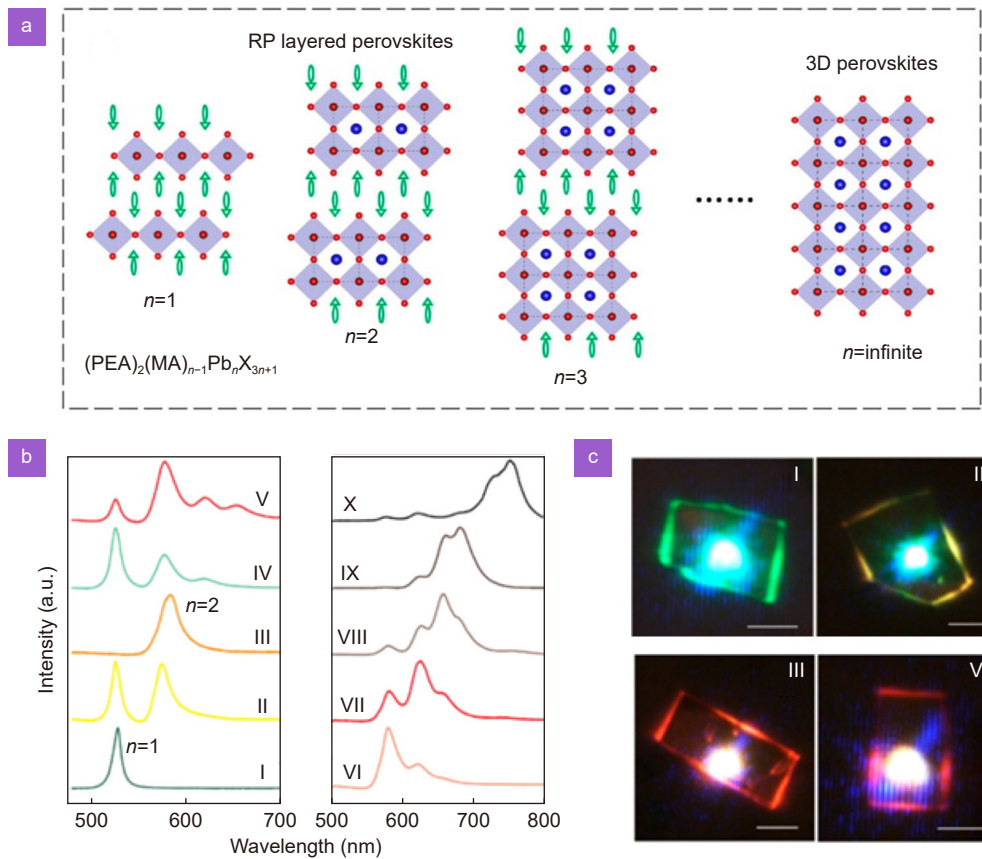


Fig. 3 | Perovskite/perovskite heterostructure. (a) Schematic crystal structures of $(\text{PEA})_2(\text{MA})_{n-1}\text{Pb}_n\text{X}_{3n+1}$ perovskites with different n values. $n = \infty$ - 3D perovskite. (b) PL spectra of various HSS excited by a 442 nm laser. 527 nm peak corresponds to $(\text{PEA})_2\text{PbI}_4$ ($n = 1$), and the 575 nm peak - $(\text{PEA})_2(\text{MA})\text{Pb}_2\text{I}_7$ ($n = 2$). (c) Optical images of different HSS (from Fig. 3 (b)) under 442 nm. Scale bars are 5 μm . Figure reproduced with permission from ref.¹⁵⁰, Copyright © 2018, American Chemical Society.

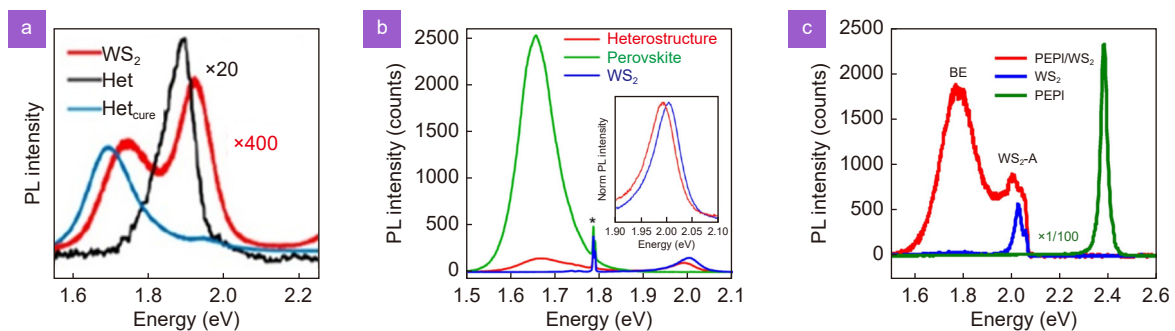


Fig. 4 | Perovskite/TMD heterostructures. (a) Demonstration of PL enhancement: PL spectra of the 2-layers WS_2 (red), and $\text{BA}_2\text{MA}_3\text{Pb}_4\text{I}_{13}/\text{WS}_2$ heterostructure before (black) and after (blue) interface curing using laser annealing. (b) Demonstration of PL quenching: PL spectra of the monolayer WS_2 (blue), MAPbI_3 (green), $\text{MAPbI}_3/\text{WS}_2$ heterostructure (red), the insertion highlights the WS_2 peak shift due to trion emission. The asterisk (*) indicates the peak from the sapphire substrate. (c) PL spectra of the $(\text{C}_6\text{H}_5\text{C}_2\text{H}_4\text{NH}_3)_2\text{PbI}_4$ (PEPI) perovskite (green), 1L WS_2 (blue), broadband emission in the perovskite/ WS_2 heterostructure (red) originated from the interface interlayer excitons at 110 K. Figure reproduced with permission from: (a) ref.⁹³, Copyright © 2019, American Chemical Society; (b) ref.¹⁶¹, Copyright © 2019, American Chemical Society; (c) ref.⁹⁵, Copyright © 2020, American Chemical Society.

the TMD and perovskite components. The charge redistribution creates local electrical fields, which decouple WS_2 layers making them effectively single layers. Single-layer WS_2 is a direct semiconductor, which explains the PL enhancement⁹³. Besides the free charge transfer, ex-

citonic energy transfer from the exciton state of $(\text{C}_6\text{H}_5\text{C}_2\text{H}_4\text{NH}_3)\text{PbI}_4$ to an upper-lying exciton state of WS_2 is also possible^{95,155}. Interestingly, even the deeper perovskite layers contribute to the energy transfer, leading to a large enhancement of PL from WS_2 ⁹⁵.

While the charge transfer may cause the TMD emission enhancement, emission from the perovskite component can undergo PL quenching^{156–161} (Fig. 4(b)). This phenomenon can be explained by interlayer charge transfer between the 2D perovskite layer and the 2D material due to the band alignment: electrons are able to transfer from the perovskite to TMD, and vice versa for holes. Interestingly, some theoretical predictions state that only hole transport is allowed in 2D perovskite-TMD HSs and only in the case of a monolayer direct bandgap TMDs¹⁵⁵, while the electron transport is blocked by the perovskite organic layer. But there are multiple experimental evidences that the electron transfer from the perovskite to TMD does occur resulting in the perovskite PL quenching^{93,156}. Another evidence of the electron transfer from the perovskite to the TMD layer is the relative enhancement of the TMD trion emission^{156,159,161}. The n-type doping of the TMD component results in PL shift due to increased contribution of the trion emission. This can be explained by an excess of free electrons, able to bind with the excitons, in the TMD layer due to the charge transfer from the perovskite.

Zhang et al.⁹⁵ discovered an additional enhanced broadband emission specific only in the HS¹⁵⁶. The broad emission originates from the perovskite-TMD interface states (Fig. 4(c))⁹⁵. Chen et al.⁸⁵ also observed broadband emission, attributed to the interlayer excitons in various 2D perovskite/WS₂ HSs. The authors also reported partly circularly-polarized emission from the heterostructure without an additional magnetic field or circularly polarized excitation. The chiral perovskite is the source of spin-polarized carriers that are injected into the TMD layers through the interface¹⁶².

The computational analysis predicts more unique properties in monolayer perovskite/monolayer MoS₂ system. In-plane anisotropy of the charge transport is expected due to the different electron and hole effective mass along [1 0 0] and [0 1 0] directions. The bandgap of the HS is reduced relative to the constituent materials for which the HS can absorb the majority of the solar irradiation⁸³.

The band alignment in the perovskite-TMD HSs is critical in determining their properties and the performance of the device made. For the majority type-II heterojunctions formed between perovskites and TMDs, the band alignment decides the operation wavelength and bandwidth of the optoelectronic devices. It facilitates the built-in potential and charge separation at the hetero-

junction, which could reduce the dark current and suppress the radiate emission, and thus enhance the sensitivity and detectivity or the speed of the PDs^{87,88,159,163,164}. Combining type I and type II band alignment to enjoy the higher quantum efficiency for stronger absorption in type I alignment while to make use of type II structure to enhance the charged carrier injection and extraction to perovskite or TMD⁹¹. Moreover, changing the thickness of the perovskite material in perovskite-TMDs HSs can modulate the band structure. For instance, theoretical calculations showed that the band offsets of (MA)_{n+1}Pb_nI_{3n+1}/WS₂ HS could be either type-II (for perovskite of $n < 9$) or type-I (for $n \geq 9$)¹⁶⁵. As a result, the HSs composed of thinner perovskite layer have higher photoresponsivity and photoresponse speed¹⁶⁵. Furthermore, the appropriate alignment of the excitonic states in perovskite-TMD HSs not only allows the charge transfer but also activates the energy transfer¹⁶⁶.

Work function tunability

The work function (WF) is one of the essential metrics for device fabrication in both perovskites and TMDs^{167–171}. For different materials, choosing a metal with appropriate WF facilitate the charge transport and extraction^{171,172}. For example, the metal with a higher WF has a lower contact resistance with PtSe₂¹⁷⁰. For 2D semiconductor devices, the WF of the metal used for device fabrication may induce Fermi level pinning. The effect of the Fermi level pinning and ways to improve the device performance for 2D semiconductors was discussed in detail in a recent review¹⁶⁹. In PDs based on perovskite/TMD HSs, TMDs are used as a transport channel layer for improving the charge extraction of the photogenerated charge carriers. Besides, Au is the most used metal for PDs fabrication due to its suitable WF (~5.10–5.47 eV) with many semiconductor materials.

On the other hand, in solar cells, TMDs can be utilised as either a standalone charge transporting layer or a complementary interlayer in perovskite, which will be discussed in Section *Solar cells*. Mainly, the charge transfer efficiency increases with a decrease in the WF of the material used as a hole extraction layer (e.g., TMD), which ultimately boosts the power conversion efficiency of the solar cells. For TMDs, the WF can significantly change due to layering or doping. For example, in the case of MoS₂, it is possible to tune the WF from 3.5 to 4.8 eV, which allows the selection of a material for removing holes for each specific perovskite and improving

electron transfer^{147,173–176}. Therefore, by carefully controlling the WF of the semiconductor material and the WF of the metal contact, the charge transport and extraction can be improved and hence the overall device performance.

Synthesis and fabrication of perovskite/TMD heterostructures

Synthesis of TMDs

The methods to fabricate 2D TMDs can be divided into two main categories of top-down and bottom-up methods with their own unique advantages. The top-down methods include various exfoliation processes such as mechanical and liquid-assisted exfoliation techniques¹⁷⁷. Exfoliation is the most commonly used method until now, in particular the mechanical exfoliation, in labs for fundamental and proof of concept studies. The basic idea of all exfoliation techniques is to apply a force to weaken the vdWs interaction between the layers of bulk crystals while saving the in-plane covalent bonds of each layer. In general most of the exfoliation techniques used have the advantage of obtaining the highest quality of crystals with the cleanest surface and lowest defect densities, which is critical for the fundamental studies of the properties of TMDs¹⁷⁸. The drawbacks of exfoliation method are the low production yield, coexistence of thick flakes along with monolayer or multilayer flakes, and slow production rate along with small 2D crystal size (few tens of micrometers)^{177,178}. Larger 2D crystal size and TMD HSS can be obtained by gold assisted exfoliation method thanks to the bond between gold and 2D TMD layer that is stronger than the vdWs interaction between monolayers of the bulk crystal^{179,180}. **Figure 5** shows a schematic illustration of the Au-assisted exfoliation method as well as comparison of PL spectra with conventional mechanical exfoliation showing good crystal quality¹⁸⁰.

In contrast, chemical vapour deposition (CVD) and wet-chemical syntheses belong to the bottom-up methods¹⁷⁷. Unlike the low yield and production rate of exfoliation method, CVD technique showed the potential to produce TMDs in large lateral sizes, controlled morphology and number of layers, and HSS in lateral and vertical direction of different materials^{177,178,181–183}. **Figure 6(a)** shows a flow chart for TMDs synthesis via CVD method. TMDs growth are categorised into four paths based on distinct mass fluxes of metal precursors and growth rates

described in **Fig. 6(a)**¹⁸⁴. In case of high mass flux of metal precursor, large-scale continuous polycrystalline TMD monolayers can be obtained. Small and large domains for the monolayers can be controlled via controlling the growth rate. While in case of low mass flux of metal precursor, the resultant TMD monolayers are single-crystalline with different sizes which can be also controlled through controlling the growth rate.

In general, all the fabrication strategies have unique advantages and disadvantages. **Figure 6(b)** summarises the pros and cons of various fabrication strategies.

Synthesis and nanoscale morphology control of 3D halide perovskites

As soft ionic materials, halide perovskites possess exceptional structural and compositional tunability. They consist of metal halide octahedra which serve as basic building blocks that can be arranged in different ways, forming materials with various dimensionalities (3D to 0D)^{9,185}. The dimensionality, in this case, refers to the connectivity of the inorganic lattices at the molecular level. For 3D perovskites, the materials adopt a chemical formula of ABX_3 , where A , B , and X represent a monovalent cation, a metallic dication, and a halide, respectively (**Fig. 7(a)**). Structurally, the metal halide octahedron corner shares to each other in three directions forming a continuous hollow anionic framework with the A -site cations sitting in the cuboctahedral cavity, providing charge balances. By controlling their growth kinetics, it is also possible to obtain low dimensional nanostructure forms of the materials, such as quantum dots, 2D platelets, and 1D nanowires^{186,187}. However, these nanostructures differ from low dimensional perovskites in that the framework of the material remains the same at the molecular level (3D), e.g. composition is the same, but with the crystal size changing to the point where the system exhibits size-dependent properties at the nanoscale (i.e., morphological dimensional reduction process; **Fig. 7(b)**).

As a result of their 3D inorganic lattice connectivity, 3D halide perovskites are non-layered materials featuring no vdWs gap with the framework. Such non-layered feature makes it relatively difficult for the top-down synthesis of 3D halide perovskites flakes from their bulk material by mechanical exfoliation, which is a typical strategy to obtain thin layers from 2D layered materials. As such, efforts have been channeled to fabricate the materials through a bottom-up fashion¹⁸⁸. They typically can be divided into two types: colloidal and non-colloidal

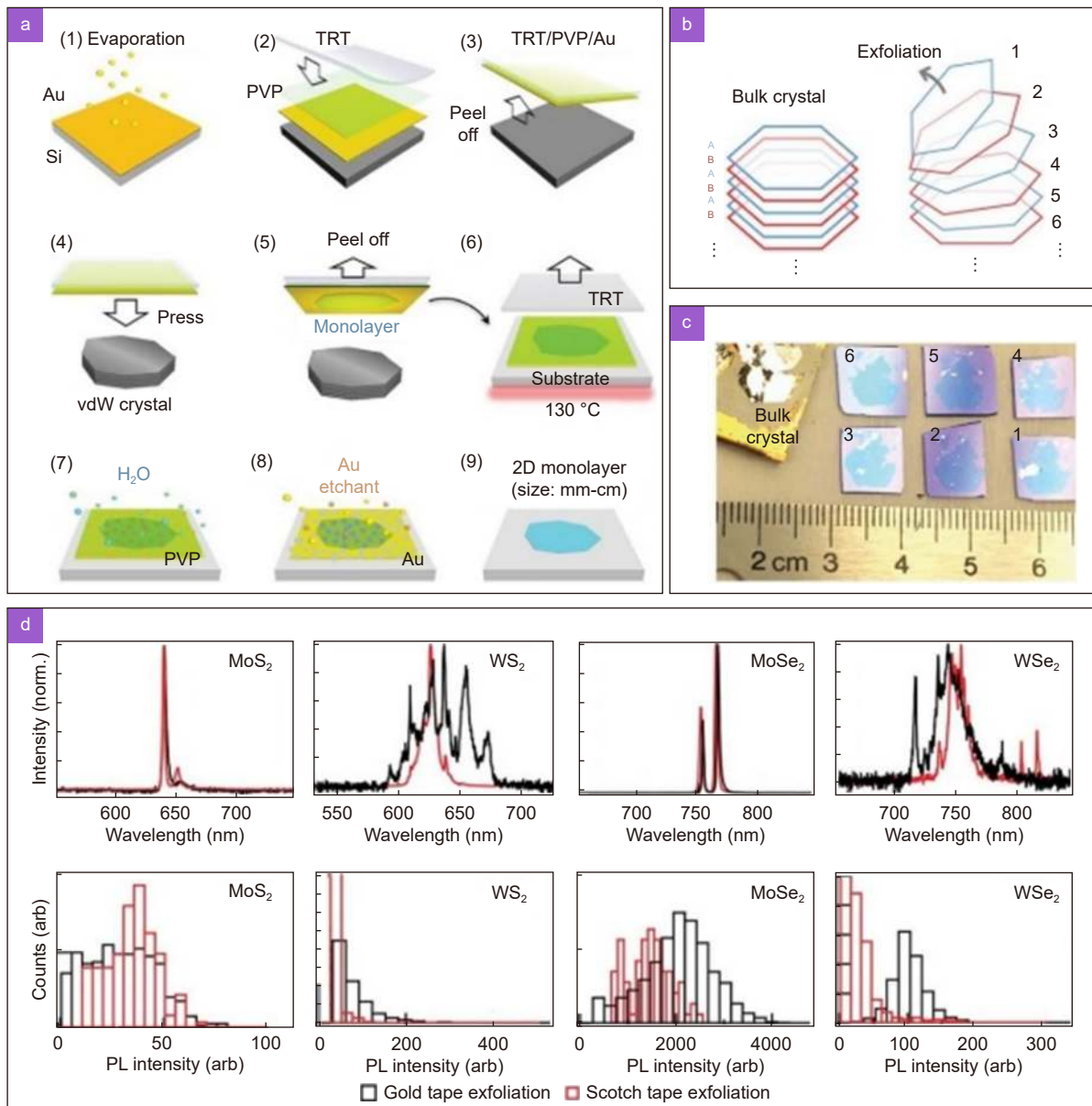


Fig. 5 | Schematic illustration of Au-assisted exfoliation PL for the large area TMDs monolayers. (a) Steps of large area exfoliation of TMDs using Au (TRT stands for thermal release tape). **(b)** Schematic of the layer-by-layer exfoliation technique to yield even and odd layers from an AB-stacked vdWs crystal. **(c)** Photograph for large area monolayers. **(d)** Comparison of PL spectra of Au-assisted exfoliation and traditional exfoliation measured at 4K for different TMDs (top) and intensity distributions (bottom). Black and red colors for Au and Scotch tape-exfoliation, respectively. Figure reproduced with permission from ref.¹⁸⁰, Copyright © 2020, AAAS.

routes. In the former, various solvent and capping agents (i.e., ligands) are used^{189–191}. Therein, the formation of nanocrystals is induced by the low solubility of perovskite precursors in a “bad” solvent system (that does not dissolve the materials) with the capping ligands limiting the growth of nanocrystals (Fig. 7(c)). The non-colloidal method heavily relies on vapor-phase approaches and the final materials can be achieved via one- or sequential two-step depositions^{192–194} (Fig. 7(d)). There also exist studies that combine the solution process and va-

por-phase conversion, providing extra angles over the formability of the materials¹⁹⁵. Due to the enormous number of preceding reviews on the subject^{186,187,196,197}, the above strategies are not elaborated at length in this review. Instead, the focus will be given to the 2D counterparts where relatively rare reports exist discussing the topic. Nonetheless, due to similar chemical and physical features, one could imagine some of the methods developed for 2D halide perovskites can also be applied for the 3D congeners.

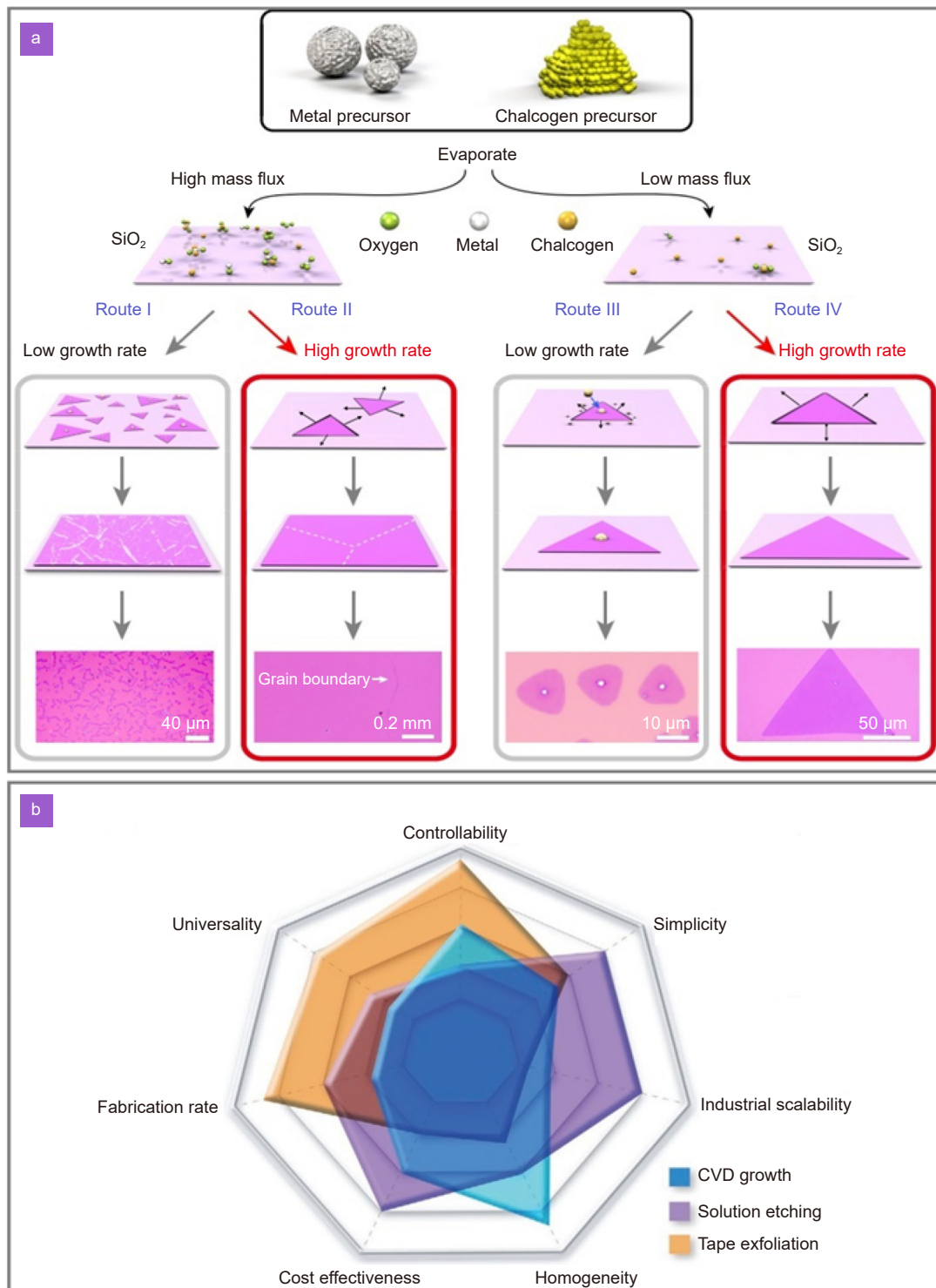


Fig. 6 | Flow chart for TMDs production via CVD method and comparison with various fabrication strategies for TMDs heterostructures. (a) General growth process to produce TMDs via CVD. (b) Comprehensive comparison of various fabrication strategies of TMDs heterostructures. Figure reproduced with permission from: (a) ref.¹⁸⁴. Springer Nature; (b) ref.¹⁸². John Wiley and Sons.

Synthesis of atomically thin 2D halide perovskites

2D halide perovskites have attracted significant interest in the field of optoelectronic devices owing to their strong quantum and dielectric confinement effects together with superior stability relative to their 3D coun-

terparts^{198,199}. 2D halide perovskites are formed as a result of a self-assembling process in which the organic cations are able to spontaneously find their appropriate positions and create a complex supramolecular framework, such that they lie on both sides of the metal-halide

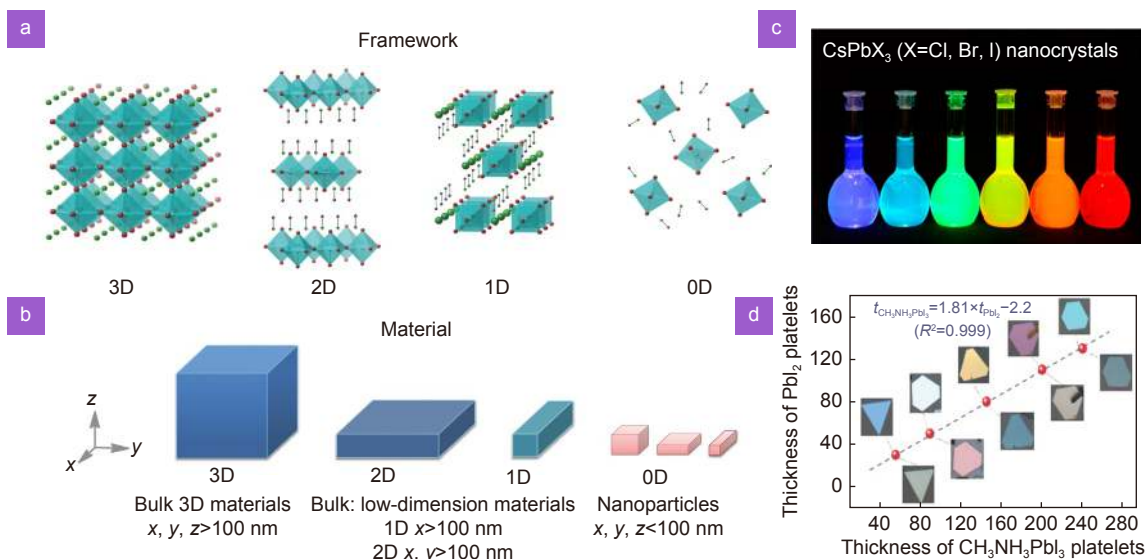


Fig. 7 | (a) Schematic representation of halide perovskite materials with different dimensionalities ranging from 3D to 0D. (b) Schematic representation of materials with different degrees of confinement. (c) Image of colloidal perovskite nanocrystals taken under UV lamp ($\lambda = 365$ nm), which feature tunable emission behavior as a function of composition and particle size. (d) Diagram correlating different thicknesses of PbI₂ platelets and the corresponding CH₃NH₃PbI₃ (images below data line) grown on muscovite mica using van der Waals epitaxial growth. Figure reproduced with permission from: (a, b) ref.³³⁷, John Wiley and Sons; (c) ref.¹⁹⁰, Copyright © 2015, American Chemical Society; (d) ref.¹⁸⁸, John Wiley and Sons.

slabs, forming an alternating organic-inorganic layered structure. Such molecular self-assembly can be not only carried out through a slow process (e.g., single crystal growth) but also achieved with a fast deposition method like spincoating. The driving forces for the process are believed to be collective intermolecular interactions between the constituent ions and molecules. In particular, while ionic bonding among the inorganic ions is responsible for the formation of extended corner-sharing octahedral network, hydrogen bonding and/or Coulombic interactions promote the stabilization of the interface between the organic cations and halometallate lattices. Additionally, vdWs interaction (e.g., π - π stacking), induced by the presence of appropriate organic functional groups, could also provide extra incentive for the materials formation.

Unlike conventional 2D materials where atoms are held together through relatively stronger covalent bonds, the inorganic framework in 2D halide perovskites is more ionic and “soft” in nature. Coupled with the low energetic barrier for the materials formation, various inexpensive and facile processing methods have been developed to fabricate the materials, especially at relatively low temperature²⁰⁰. More importantly, the structural versatility and tunability in 2D halide perovskites allow a plethora of organic cations templating agents with diverse architectures to be used, serving as a rich and fer-

tile “playground” for the preparation of interesting structures with varying chemical and physical properties. This, in turn, would indirectly affect the methods in which they can be fabricated.

For example, it is more straightforward to obtain atomically thin layers of 2D halide perovskites by mechanical exfoliation when the materials are templated by monoammonium-based organics (R-NH₃⁺ where R denotes organic functionality) in place of the diammonium (NH₃⁺-R-NH₃⁺) congeners. This is because, in the former, the organic species assemble into a bilayer structure where the ammonium “heads” form a Coulombic interaction with the inorganic layers (through deep penetration into cuboctahedral cavities built from the four nearest neighbors terminally bound axial halides), while the R “cores” interact with each other *via* vdWs forces^{9,201}. Exfoliating the materials would thus separate the anionic halometallate sheets from the bulk with a single layer of organic cations still capping both ends of the sheets, maintaining charge neutrality of the overall structure.

Similar to that employed in conventional 2D materials (e.g., graphene and TMDs), mechanical exfoliation would require a single crystal or bulk of 2D halide perovskites as the starting samples. The most widely used method to grow high-quality of 2D halide perovskite single crystals is *via* a solution process whose growth

principle typically depends on the solubility variation of the precursor solutes as a function of temperature or solvent content. Some of the approaches include slow cooling of hydrohalogenic-based precursor solutions (i.e., acid precipitation)^{202,203} (Fig. 8(a)), antisolvent vapor-assisted crystallization (AVC)^{204,205} (Fig. 8(b, c)), inverse temperature crystallization (ITC)²⁰⁶, two-step organic cation intercalation²⁰⁷, and induced peripheral crystallization (IPC)^{208–210} (Fig. 8(d)). Seminal works by Niu et al.¹⁴⁸, and Yaffe et al.²¹¹, reported the mechanical exfoliation of ultrathin (PEA)₂PbI₄ and (BA)₂PbI₄ 2D crystals (Fig. 8(e)) (where PEA and BA denote 2-phenylethylammonium and 1-butylammonium, respectively) that were obtained from intercalation of organic cations into preformed PbI₂ microcrystals and slow cooling of the hydroiodic solution containing precursor materials, respectively. The morphology and optical properties of the exfoliated flakes were investigated *via* absorption spectroscopy and atomic force microscopy. Since then, various efforts on mechanically exfoliating different types of 2D halide perovskites have been documented. In general, the method is suitable to obtain ultrathin flakes required for the investigation of materials fundamental properties or the fabrication of nano-scale optoelectronic devices. It can also be applied on “quasi-2D perovskites” to access materials with a specific number of inorganic layers at the molecular level possessing

interesting physical characteristics^{44,148,211}. However, it remains challenging to use mechanical exfoliation for practical material manufacturing because it cannot result in flakes with good control of size and thickness.

To address the issue, Dou et al., attempted to directly synthesize large-area atomically thin 2D halide perovskite sheets *via* a solution route¹⁴⁷. In this method, a ternary solvent mixture was utilized to prepare an ultra-low concentration of perovskite precursor solution. By controlling the evaporation temperature of participating solvents, 2D halide perovskite nanosheets of various compositions and thicknesses could then be grown on Si/SiO₂ substrate (Fig. 8(f)). A more systematic study was reported by Chen et al., who demonstrated that solvent blending ratio, solvent polarity, crystallization temperature are the critical factors affecting the thin crystal formation²¹². It was further shown that the synergetic effects of diffusion dominated branched growth and c-axis suppression dictate the growth of the 2D halide perovskite crystals. Under optimum condition, 2D halide perovskites with relatively large lateral dimension of tens of micrometre, while at the same time featuring a thickness of a few nanometres could be obtained. Nonetheless, although solution-based methods have received considerable attention, it lacks processibility after deposition and it is difficult to transfer the samples to desired substrates.

For this reason, colloidal-based liquid-phase

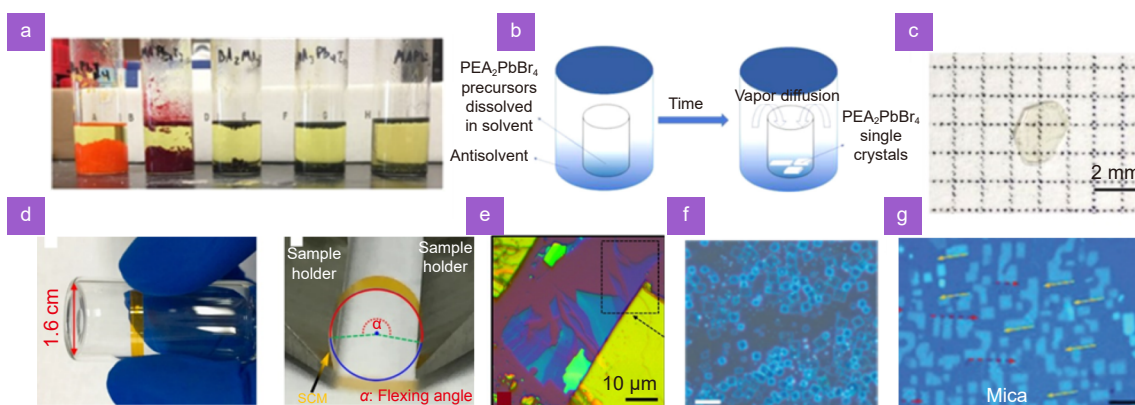


Fig. 8 | Perovskites synthesized by different methods. (a) Photographs of $(\text{CH}_3(\text{CH}_2)_3\text{NH}_3)_2(\text{CH}_3\text{NH}_3)_{n-1}\text{Pb}_n\text{I}_{3n+1}$ crystallites obtained from acid precipitation method. (b) Schematic illustration of antisolvent vapor-assisted crystallization method. (c) Optical image of $(\text{C}_6\text{H}_5\text{CH}_2\text{CH}_2\text{NH}_3)_2\text{PbBr}_4$ single crystal obtained from the technique. (d) Images of a piece of $(\text{C}_6\text{H}_5\text{CH}_2\text{CH}_2\text{NH}_3)_2\text{PbI}_4$ single crystal grown from induced peripheral crystallization (3.5 μm in thickness) that wrapped around a small tube (1.6 cm in diameter; left), demonstrating its flexibility and was used for a flexing angle study (right). (e) Optical micrograph of exfoliated $(\text{C}_4\text{H}_9\text{NH}_3)_2\text{PbI}_4$ flakes grown on SiO_2/Si substrates. (f) Optical image of atomically thin 2D $(\text{C}_4\text{H}_9\text{NH}_3)_2\text{PbBr}_4$ obtained from colloidal method with a scale bar of 10 μm . (g) Epitaxial $(\text{C}_4\text{H}_9\text{NH}_3)_2\text{PbI}_4$ flakes deposited on mica by co-evaporation where the two in-plane orientations were marked by red and orange arrows with an offset θ about 9° (center; scale bar of 5 μm)²¹⁸. Figure reproduced with permission from: (a) ref.²⁰³, Copyright © 2016, American Chemical Society; (b, c) ref.²⁰⁴, Copyright © 2017, American Chemical Society; (d) ref.²¹⁰, under the terms of the Creative Commons CC BY license; (e) ref.²¹¹, American Physical Society; (f) ref.¹⁴⁷, AAAS; (g) ref.²¹⁸, John Wiley and Sons © 2017 WILEY - VCH Verlag GmbH & Co. KGaA, Weinheim.

exfoliation was exploited to grow 2D halide perovskites sheets. It also relies on the use of solvent and optimization to Hansen solubility parameter can be used to effectively reduce exfoliation energy. Additionally, the method involves the insertion of long-chain organic molecules into the preformed 3D perovskites, thus exfoliate or “cleave” the parent inorganic framework to layered structures. The capping ligands prevent the obtained nanoplates from agglomeration and as such, maintain their dispersibility in the organic solvents. Hintermayr et al., demonstrated this concept with oleylammonium cation to induce the formation of quasi-2D perovskites with different inorganic sheet thicknesses²¹³. In general, the colloidal chemistry approach allows better sample processability in comparison to the direct solution synthesis method. However, the preparation of materials with larger sheets remains difficult and fundamentally challenging. This is because the resulting sheets depend strongly on the interaction with the ligand as well as storage condition (e.g., temperature) and as a result, they are reasonably prone to breaking or aggregating in the colloidal suspension.

CVD is also used to grow atomically thin 2D halide perovskite as it is widely used for the fabrication of conventional 2D materials, such as graphene²¹⁴, MoS₂²¹⁵, WS₂²¹⁶, and h-BN²¹⁷, of high quality. In this regard, Chen et al. reported successful preparation of high optical quality atomically thin BA₂PbI₄ grown on mica substrates using CVD method (Fig. 8(g))²¹⁸. The resulting 2D halide perovskite flakes were of rectangular shapes with the lateral size of 5–10 μm and thickness below 80 nm and featured certain epitaxial orientations relative to the underlying substrates. While the method could yield materials exhibiting optical profiles on par with those mechanically exfoliated counterparts, it should be noted that the layered and hybrid nature of 2D halide perovskites complicates its growth during CVD process. There is a risk of cluster formation and phase separation as a result of contrasting physical properties between the organic and inorganic constituents. In particular, the organic cation lacks the diffusivity required for migration to the substrate surface, while the inorganic metal halide possesses vapor pressure several orders lower in magnitude relative to the former. As such, extra attention has to be paid to the deposition condition (e.g., heating temperature and time) to reliably obtain materials with well-defined thickness.

Fabrication of halide perovskite/TMD heterostructures

3D perovskite/TMD heterostructures

Unlike 2D perovskite/TMD HSs, there are relatively more reports on 3D perovskite/TMD HSs^{219,220}. Hereby, we go through some of the fabrication methods to realize 3D perovskite/TMD HSs, providing a bigger picture of the assembly formation. Nonetheless, the fabrication process is generally translatable from one system to another as both 3D and 2D perovskites have similar physical and chemical properties are both soft semiconductors, though further optimization would still be required for optimal device performances. One common technique to realize 3D perovskite/TMD HSs is vapor deposition that involves the conversion of raw materials to a vapor phase at an elevated temperature before condensing it back to form the desired deposit on certain substrates^{163,192,221,222} (Fig. 9(a, b)). The fabrication of HSs typically starts with the deposition of a uniform and flat 2D TMD flake with CVD, followed by another vapor deposition of the perovskite layer through a one- or two-step method. In one-step deposition, dual-source comprising both organic (e.g., methyl ammonium iodide) and metal halide (e.g., PbI₂) salts or one source containing 3D perovskite (e.g., MAPbI₃) is used to form perovskite at target substrate^{221,222}. While in two-step deposition, the metal halide nanoplatelets are grown on the substrates with the 2D TMD flakes before subsequent exposure to the organic halide vapor to induce the reaction and convert the underlying layer to perovskite^{163,192}.

Another common method to construct 3D perovskite/TMD HSs is the dry/wet transfer in which the samples are physically transported from one substrate to another with the help of a solid or liquid medium^{223–225}. In the case of solid medium, polymer films e.g., polydimethylsiloxane (PDMS) or poly(methyl methacrylate) (PMMA) have been widely used as they have good adhesion with the samples to facilitate the transfer process^{226–228}. Upon transfer, the polymer films can be easily removed with organic solvents that are orthogonal to the samples. As such, using this method, layer-by-layer vertically stacked halide perovskites/TMD HSs with desired sequences can be obtained through a few cycles of transfer processes^{89,229}.

Attention has also been paid to solution-based approaches, especially those that can be carried out at a low temperature, in an effort to realize facile and mass

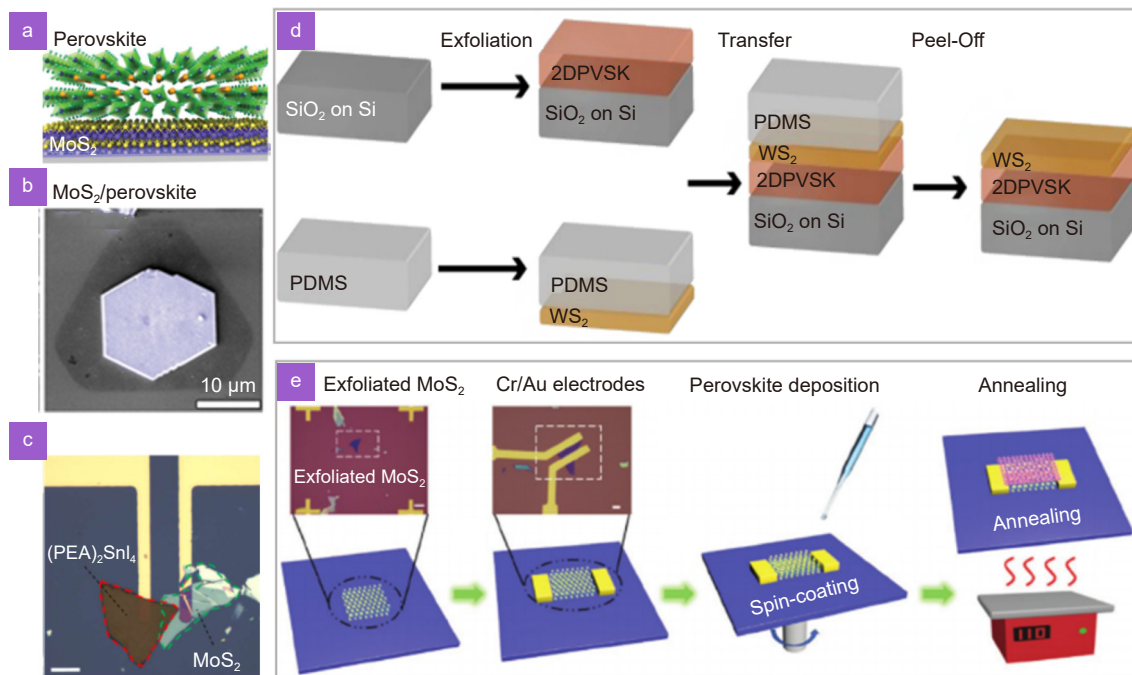


Fig. 9 | Fabrication of TMD-perovskite heterostructures and devices. (a) Structure models of halide perovskite/MoS₂ heterostructure. (b) False-colored scanning electron microscopy image of evaporated perovskite on MoS₂ exhibiting triangular and hexagonal shape. (c) Optical microscope image of the as fabricated (PEA)₂SnI₄/MoS₂ PD (the scale bar is 20 μm). (d) Schematics of typical exfoliation and dry transfer process for perovskite/TMD heterostructure fabrication. (e) Schematic diagram of the facile fabrication process of 2D perovskite/TMD heterostructure with spincoating. Figure reproduced with permission from: (a, b) ref.¹⁹², John Wiley and Sons; (c) ref.²⁴². Copyright © 2019, American Chemical Society; (d) ref.⁹³. Copyright © 2019, American Chemical Society; (e) ref.¹⁵⁸. John Wiley and Sons.

production of 3D perovskite/TMD HSs. Among the various processes reported, spincoating, ex-situ hybridization, and in-situ growth are the most popular. The latter two are similar in that TMD would be mixed in solution with the perovskite materials or precursors to induce binding and interaction between each of the components, thus forming a composite^{230–232}. The difference lies at the stage in which the TMD would be added. In the case of ex-situ hybridization, mixing is between TMD and pre-synthesized perovskite, while in in-situ growth, TMD is usually pre-added into the metal halide precursor solution to form a uniform mixture before the formation of perovskite itself. Because of the nature of the fabrication sequence, the latter is believed to result in a better close contact interface between the perovskite nanocrystals and TMD materials.

One of the biggest advantages that 3D halide perovskites offer is their solution processability^{233–235}. With this regard, the spin-coating method has been shown to be capable of delivering high-quality materials that can yield optoelectronic devices with a record performance of efficiency^{236–238}. Similarly, 3D perovskite/TMD HSs can be obtained by simply spin-coating the halide perovskite on top of the preformed TMD layer. For ex-

ample, one-step spin-coating the perovskite precursor solution has been demonstrated on mechanically exfoliated MoS₂^{239,240}, CVD-deposited WS₂¹⁶³, and chemically exfoliated MoS₂⁹⁰. While the resulting perovskite properties can be tuned with deposition condition (solvent, temperature, and additive) or procedure (one vs two steps), the morphology and orientation of the as-obtained 3D perovskite would interestingly also vary with the underlying TMD. Wang, et al., reported perovskite films showing a fibril-like network morphology on chemically exfoliated MoS₂⁹⁰, while Tang, et al., observed a vdWs-induced epitaxy growth of perovskite films upon deposition on solution-processed multi-layer MoS₂ flakes possessing smooth surface²⁴¹. This suggests that more attention has to be paid to the processing method of the TMD layer when it comes to the fabrication of heterostructure assembly so that devices with certain characteristics can be achieved.

2D perovskite/TMDs heterostructures

In this section, we review the recent reports of 2D perovskite/TMD HSs together with fabrication techniques associated with the assembly (see Table 2 for the summary). Most of the reports utilize the acid precipitation

method to grow single crystal 2D halide perovskites. Typically, stoichiometric amounts of organic and metal iodide (or metal oxide in some cases, such as lead (II) oxide) salts are added to concentrated aqueous hydrogen iodide (together with reducing agents H_3PO_2) to yield sufficient concentrations of the dicationic cation. The resulting mixtures containing insoluble solid are then heated (under inert gas atmosphere for Sn^{2+} -based materials to prevent its oxidation to Sn^{4+} species) until clear solutions are obtained before subsequent slow cooling to room temperature to afford good quality single crystals. Upon isolation of the desired 2D perovskites, a dry transfer technique is then utilized to construct HS assemblies with TMDs. Mechanical exfoliation of 2D perovskite flakes of thickness ca. 100 nm are conducted with either PDMS stamp or Scotch tape before they are transferred and sequentially stacked on top of target substrates, electrodes, or TMD materials.

For example, the first 2D halide perovskite/TMD HS was reported by Fang et al. in early 2019 with a demonstration of vertically integrated PD based on few-layer MoS_2 and lead-free perovskite $(PEA)_2SnI_4$ HS (Fig. 9(c))²⁴². Following that, Yang et al. observed that the HS comprising WS_2 and 2D multilayer $(BA)_2(MA)_3Pb_4I_{13}$

hybrid perovskites with an atomically thin interface exhibits enhanced photoluminescence as well as improved air stability relative to single WS_2 or 2D $(BA)_2(MA)_3Pb_4I_{13}$ perovskite alone⁹³. Figure 9(d) shows a schematic for the fabrication process of the HS. Similar perovskite material was also utilized by Fu et al. to fabricate MoS_2 -perovskite HS based PD featuring a photogating effect with greatly enhanced performance²⁴³. Meanwhile, Ma et al., fabricated chiral 2D perovskite/ MoS_2 HS to detect circularly polarized light (CPL)²⁴⁴. Such capability is attributed to the presence of chiral organic cation (S)/(R)-MBA (MBA is α -methyl benzyl ammonium) that templates the formation of (SMBMBA)₂PbI₄ or (R-MBA)₂PbI₄ perovskite showing opposite-sign circular dichroism (CD) spectra with the degree of circularly polarized PL being up to 17.6% at 77 K.

Spin coating process was introduced in 2D perovskite/TMD HS by Wang et al., who deposited $(PEA)_2PbI_4$ on top of pre-exfoliated MoS_2 from its precursor solution in organic solvent N, N-dimethylformamide (DMF)¹⁵⁸. Figure 9(e) shows the fabrication process of the assembly which was used as a PD. More about the performance of this PD will be explained in Section *Perovskite/TMD heterostructures for optoelectronic applications*.

Table 2 | Synthesis methods of 2D perovskites/TMDs heterostructures.

Year	Architecture	2D perovskite single-crystal synthesis	Heterostructure assembly	Application	Ref.
2019	$MoS_2/(PEA)_2SnI_4$	Aqueous acid method	Exfoliation with polydimethylsiloxane (PDMS) stamp (dry transfer)	PD	ref. ²⁴²
2019	$(BA)_2(MA)_3Pb_4I_{13}/WS_2$	Aqueous acid method	Exfoliation with PDMS stamp	Giant enhancement of photoluminescence emission	ref. ⁹³
2019	$MoS_2/(R-MBA)_2PbI_4$, $MoS_2/(S-MBA)_2PbI_4$, $MoS_2/(rac-MBA)_2PbI_4$	Aqueous acid method	Exfoliation with Scotch tape	Circularly polarized photoluminescence	ref. ²⁴⁴
2019	$MoS_2/(BA)_2(MA)_{n-1}Pb_nI_{3n+1}$	Aqueous acid method	Exfoliation with Scotch tape	PD	ref. ²⁴³
2020	$MoS_2/(PEA)_2PbI_4$	Mixing in organic solvent	Spin-coating	PD	ref. ¹⁵⁸
2020	$WSe_2/(iso-BA)_2PbI_4$, $WSe_2/(BA)_2PbI_4$, and $WSe_2/(S-MBA)_2PbI_4$	Aqueous acid method	Exfoliation with PDMS stamp	Interlayer exciton coupling	ref. ⁸⁵
2020	$(PEA)_2PbI_4/WS_2$	Anti-solvent evaporation and dripping method	Exfoliation with PDMS stamp	Excitonic energy transfer	ref. ⁹⁵
2020	$MoS_2/(R-MBA)_2PbI_4$, $MoS_2/(S-MBA)_2PbI_4$, $MoS_2/(rac-MBA)_2PbI_4$, $WSe_2/(R-MBA)_2PbI_4$, $WSe_2/(S-MBA)_2PbI_4$, $WSe_2/(rac-MBA)_2PbI_4$	Aqueous acid method	Exfoliation with poly (methyl methacrylate) (PMMA) stamp	Manipulation of valley pseudospin	ref. ¹⁶²
2020	$(PEA)_2PbI_4/WS_2$	Anti-solvent evaporation method	Exfoliation with PDMS stamp	Photovoltaic effect and PD	ref. ¹⁵⁶
2021	$(PEA)_2PbI_4/WS_2$	Anti-solvent evaporation method	Exfoliation with PDMS stamp	Upconversion photovoltaic effect	ref. ²⁴⁵

In addition, exfoliation with PDMS or PMMA stamp was used to deposit 2D perovskites and TMDs on top of each other with more efforts have been channeled into understanding the physical properties of 2D perovskite/TMD HSs. For instance, using this technique, Chen et al. observed the presence of strong interlayer emission at the heterostructure region, implying a robust interlayer coupling at the HS interface⁸⁵. They also showed that it is possible to manipulate valley polarization in monolayer TMDs (MoS₂ and WSe₂) *via* selective spin injection without requiring an external magnetic field or specially designed device structures¹⁶². This was achieved by incorporating chiral 2D perovskites in the HS as the valley polarization of monolayer TMD was attributed to selective spin injection from chiral 2D perovskites, which can effectively introduce population imbalance between valleys in the TMD layer.

Furthermore, Zhang et al. and Wang et al. reported experimental observation of excitonic energy transfer and upconversion photovoltaic effect, respectively, in HSs consisting of (PEA)₂PbI₄ and monolayer WS₂^{95,156,245}. In particular, unexpectedly strong PL enhancement factors of up to ~8 were found in the HS assembly. PL excitation spectroscopy revealed a distinct ground exciton resonance feature of perovskite, evidencing energy transfer from 2D perovskite to WS₂. Meanwhile, upconversion photovoltaic effect occurred by below-bandgap two-photon absorption *via* a virtual intermediate state, demonstrating that upconversion by two-photon absorption may potentially be a strategy for boosting the efficiency of 2D photovoltaic devices by virtue of the absorption of photons below the bandgap energy of the channel semiconductors.

Apart from the acid precipitation method, antisolvent vapor-assisted crystallization (AVC) is also explored in 2D perovskite/TMD HS fabrication^{95,156,245}. In general, concentrated solutions of perovskite precursors in some organic solvent (e.g., DMF) are prepared before the vapor of “antisolvents”, such as dichloromethane (DCM), is introduced slowly into the solution. The 2D halide perovskites single crystals would then be formed as a result of the supersaturation process. It is also anticipated that CVD of 2D perovskite/TMD HSs could be reported in the future as the method is scalable and known to produce high-quality materials with a good degree of thickness tunability.

Recently, PbI₂–MoSe₂ HS was reported in which the PbI₂ layer was evaporated under vacuum condition on

MoS₂, growing in a quasi-layer-by-layer epitaxial mode²⁴⁶. Such PbI₂ layer could serve as a starting point to fabricate 2D perovskite via two-step process where reaction with suitable organic halide can be initiated upon exposure of the vapor to the PbI₂ layer. The possibility of epitaxial growth of 2D perovskite with preferred orientation as a function of substrates can also open up a new avenue for interesting physics to be unraveled.

Perovskite/TMD heterostructures for optoelectronic applications

The intriguing properties of perovskites and TMDs as well as their HSs, as introduced in previous sessions, hold great potential for optoelectronic applications. As two mostly investigated and important optoelectronic devices, PDs and solar cells based on perovskite/TMDs HSs will be discussed in the following section.

Photodetectors (PDs)

To better compare the performance of PDs at various configurations at different working conditions, a set of key parameters are defined. These parameters include photoresponsivity (R), which is the ratio of the generated photocurrent to the incident light power; external quantum efficiency (EQE), defined as the ratio of the number of generated charge carriers to the number of photons used to illuminate the device; response time (τ), that is the time required for the photocurrent to change from 10% to 90% (rising) and from 90% to 10% (decay) under modulated light excitation; Gain (G), that is a term used to evaluate the number of multiple carriers generated by a single incident photon; noise equivalent power (NEP), which means the minimum signal that can be detected from the total noise; specific detectivity (D^*), which represents the sensitivity of PDs of different geometries; linear dynamic range (LDR), which is a term to define the responsivity range of the PD. The expressions for all the key parameters are summarised in Table 3.

2D materials have been used as a transport layer to improve the performance of the PDs based on halide perovskites. Since the first report on perovskite/graphene (G) heterojunction PD²⁴⁷, many PDs based on a transport layer of G have been demonstrated thanks to its high carrier mobility^{248–252}. Generally, the perovskite/G PDs are characterized by high photoresponsivity as compared with other perovskite/2D PDs. However, the large dark current due to the gapless nature and high conductivity of graphene has a strong adverse impact on the PDs

Table 3 | Key parameters of merits for photodetectors (PDs).

Parameter	Expression	Unit	Symbol definition
Photoresponsivity (R)	$R = I_p/P$	A/W	I_p : photocurrent. P : illumination power.
External quantum efficiency (EQE)	$EQE = hcI_p / e\lambda P$	-	h : Planck's constant. c : speed of light. λ : illumination wavelength. e : unit charge.
Response time (τ)	τ	s	τ_{rise} : rising time τ_{decay} : decay/fall time. Terms are used to define how fast the detector is.
Gain (G)	$G = \tau_{life} / \tau_{trans}$	-	τ_{life} : lifetime of the generated charge carriers. τ_{trans} : drift transient time. $\tau_{trans} = L^2 / \mu V_{bias}$ where L is the channel length, μ is the carrier mobility, and V_{bias} is the applied bias voltage.
Noise equivalent power (NEP)	$NEP = i_N/R$	W/Hz ^{1/2}	i_N : the noise current at 1 Hz bandwidth (A/Hz ^{1/2}).
Specific detectivity (D^*)	$D^* = A^{1/2}R/i_N$	cm Hz ^{1/2} /W (Jones)	A : the active area of the PD in cm ² .
Linear dynamic range (LDR)	$LDR = 20\log(I_p'/I_{dark})$	-	I_p' : photocurrent at a light intensity of 1 mW/cm ² . I_{dark} : dark current.

detectivity and hinders these devices in some applications^{239,253,254}. On the other hand, devices based on perovskite with TMDs hybrid structures showed a balanced performance^{98,163,219,221,255}. In this section we discuss the state-of-the-art perovskite/TMD PDs starting with MAPbI₃/TMD HSs as the mostly studied perovskite/TMD PDs then CsPbBr₃/TMD HSs followed by other perovskite/TMD HSs. The effect of using different materials and different structures on the PD performance is discussed in detail.

MAPbI₃/TMD heterostructures

A hybrid structure of MAPbI₃ and TMD PD was firstly reported in 2016 using MoS₂²³⁹ and WS₂¹⁶³ underneath the MAPbI₃ absorbing layer. Figure 10(a) shows the device structure of MAPbI₃/MoS₂ PD, which formed a type I band alignment (the photogenerated electrons and holes are both transferred to MoS₂)²³⁹. Great strikingly enhancement in photoresponsivity (from 816.6 to 2.11×10⁴ A/W) of the HS PD was reported after surface treatment to the substrate with (3-aminopropyl) triethoxysilane (APTES) which induces n-type doping in MoS₂ and improve the device performance²³⁹. Figure 10(b) shows the photoresponsivity comparison of MoS₂, MoS₂/APTES, and perovskite/MoS₂/APTES PDs a function of wavelength. Despite the responsivity enhancement, the response time of perovskite/MoS₂/APTES PD is very slow (rise/fall time of 6.17/4.5 s) and can be enhanced using another TMD²³⁹. The slow response time

may be also attributed to the relatively thick perovskite layer which lengthened the electron transport path and increased the nonradiative recombination rate²⁵⁵. Unlike MAPbI₃/MoS₂, MAPbI₃/WS₂ forms type-II band structure¹⁶³. Figure 10(c) shows the device structure of the MAPbI₃/WS₂ PD on sapphire substrate as well as its relative band alignment¹⁶³. The device exhibits a maximum responsivity of 17 A/W under white light illumination with a high on/off ratio of 3 × 10⁵. More importantly, the dark current was one order of magnitude lower than the pristine perovskite PD due to the high mobility of the WS₂ monolayer and the efficient interfacial charge separation which reduced the carrier recombination¹⁶³. Detectivity of 2×10¹² Jones at 505 nm was reported (Fig. 7(d)). The PD speed for the hybrid PD was four orders of magnitude (2.7/7.5 ms) higher than the reference perovskite single layer due to the efficient charge separation at the interface.

Metastable metallic (1T) and stable semiconducting (2H) phases of MoS₂ with MAPbI₃ was demonstrated⁹⁰. Schematic of the device structure with the relative band alignment and the carrier transfer mechanisms are shown in Fig. 10(e). In the case of the metallic 1T-MoS₂, both the photogenerated electrons and holes are injected from perovskite to the MoS₂ layer resulting in high responsivity with a low on/off ratio as compared with 2H-MoS₂ where electrons and holes are injected into the conduction and valance bands of MoS₂, respectively. In general, the responsivity values of the HS PDs are higher

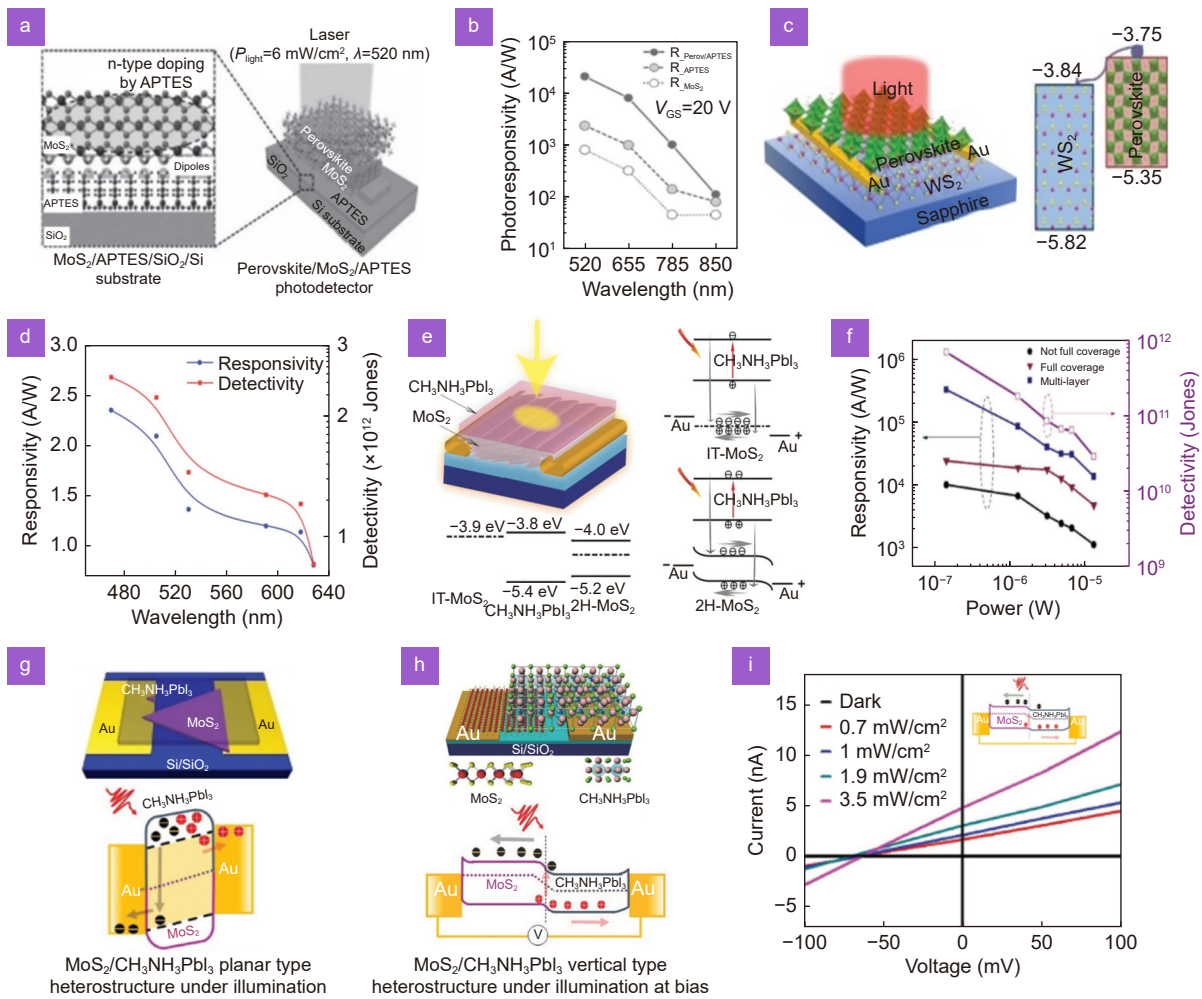


Fig. 10 | (a) MAPbI₃/MoS₂/APTES and cross-sectional structure illustration of APTES doping process. (b) Comparison of the photoresponsivity values of MoS₂, MoS₂/APTES, and perovskite/MoS₂/APTES PDs as a function of wavelength. (c) Structure of MAPbI₃/WS₂ PD on sapphire substrate and the relative type-II band alignment. (d) Spectral responsivity and detectivity of the PD showing its high detectivity. (e) MAPbI₃/MoS₂ PD with their relative band alignment (left panel) and charge transfer mechanisms (right panel) using 1T and 2H phases of MoS₂. (f) Responsivity and detectivity values of MAPbI₃/1T-MoS₂ PD as a function of illumination powers using 500 nm laser. (g–h) Planar (g), and vertical (h) structures of MAPbI₃/MoS₂ PDs and the effect of the drain bias and illumination on carrier transportation and separation. (i) I–V curves of the vertical structure under different power densities showing the photovoltaic characteristics of this hybrid structure. Inset is schematic carrier transportation and separation in this self-power mode. Figure reproduced with permission from: (a, b) ref.²³⁹, (c, d) ref.¹⁶³, (e, f) ref.⁹⁰, (g–i) ref.²⁵⁶, John Wiley and Sons.

in case of using 1T-MoS₂ with a responsivity of 3.3×10^5 A/W at 500 nm (Fig. 10(f)). The main reason for the enhanced responsivity in the case of 1T-MoS₂ is due to it has higher conductivity as compared to the 2H-MoS₂ which led to an increase in the charge transfer and transport. In contrast, the temporal photoresponse of the devices showed rise/decay times of 0.45/0.75 s and <0.025/0.05 s for the 1T-MoS₂ and 2H-MoS₂ phases, respectively. It could be noted that there is a trade-off between responsivity and response speed for PDs. This difference in the response speed in both cases was attributed to the defects that act as generation or recombination centres because 1T-MoS₂ film was prepared by

chemical exfoliation and is indeed more defective than the 2H phase⁹⁰. The annealing of 1T-MoS₂ to obtain 2H-MoS₂ allows relaxation of structural defects and hence the response speed is improved. While the more structural defects in the 1T-MoS₂ film led to high gain than that for the 2H-MoS₂ which contributed to the enhanced responsivity.

The effect of the planar and vertical structures of MAPbI₃/MoS₂ on the performance of PD was also investigated²⁵⁶. Figure 10(g, h) shows the two different structures and the corresponding effect of bias and illumination on the charge transportation and separation. In the case of the planar structure, upon illumination, the

electrons transferred to MoS₂ film which increased its Fermi level and reduced the Schottky barrier at the electrode/material interface and then separated. Though, in the case of vertical structure, the photogenerated electrons transferred to MoS₂ while holes transferred to the perovskite creating a built-in potential across the heterojunction. The vertical structure of the PD showed a better performance than the planer structure in terms of the responsivity and response speed due to the built-in potential across the heterojunction which allowed the PD to operate without any external bias (Fig. 10(i)). Despite the enhancement in the PD performance using the vertical structure, the PD showed slow rise/fall times of 2149/899 ms in the self-power mode which is attributed to defects and trap centres in the film²⁵⁶.

Wang et al. reported MAPbI₃/BP/MoS₂ hybrid 2D photogate photodiode⁹¹. Schematic illustrations of the device architecture and the energy band diagram are shown in Fig. 8(a). This design provides a fast and sensitive 2D photogate photodiode operating under reverse or zero bias. As described in Fig. 11(a), the electronic band structure of the heterojunction demonstrates type I at the MAPbI₃/BP interface and type II at BP/MoS₂ interface. The detector photocurrent is determined by the absorption layer (perovskite material) and the photocarrier ex-

traction at BP/MoS₂ interface. The fact that the binding energy of excitons is relatively small in perovskite materials contributed to the enhancement of the PD performance. Under light illumination, the spontaneously generated carriers in the perovskite layer diffuse into the BP followed by separation and collection due to the built-in electric field at the BP/MoS₂ junction. The BP/MoS₂ HS showed a rectifying behavior with a rectification ratio of 20. The dark current of the device is lowered by approximately two orders of magnitude after capping with the perovskite layer. Under 457 nm laser excitation with a bias of -2 V, the device showed a fast temporal photoresponse with rising and decay times of 150 and 240 μs, respectively (Fig. 11(b)). The maximum reported responsivity at these conditions was calculated to be 11 A/W with a corresponding detectivity of 1.3×10¹² Jones, and the highest on/off ratio was ~6×10⁴. Moreover, as described in Fig. 11(c) for the dynamic photoresponse at different illumination wavelengths, this hybrid device is suitable for broadband photodetection without any external bias due to the effective light absorption of perovskite and the large built-in potential in the BP/MoS₂ junction⁹¹.

Another scheme for enhancing the responsivity is using reduced graphene oxide (rGO) as a channel

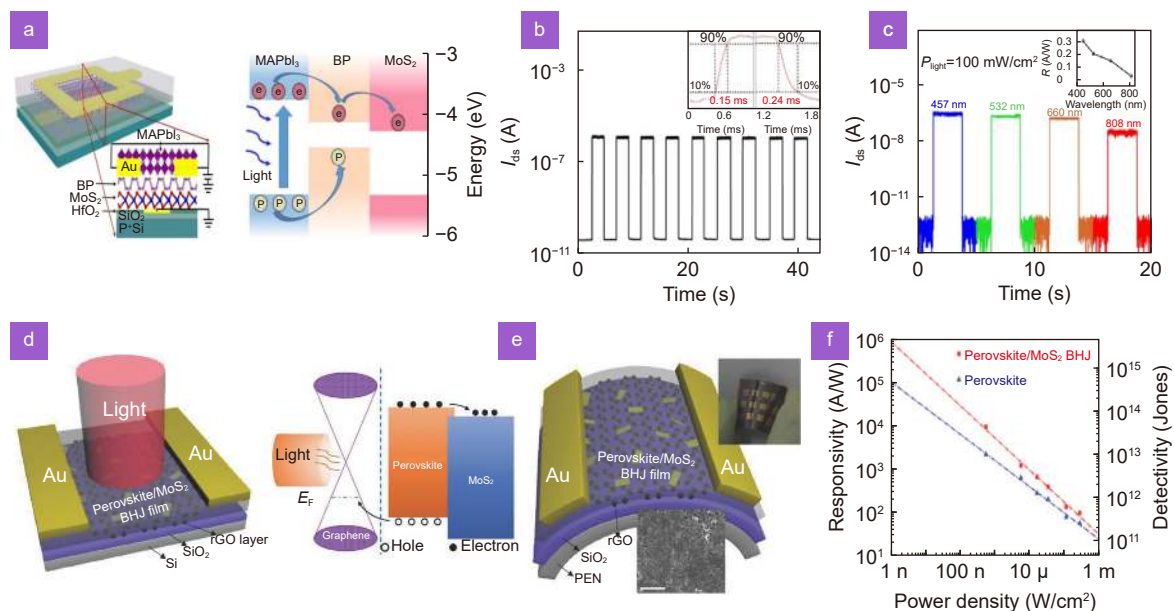


Fig. 11 | (a) MAPbI₃/BP/MoS₂ and charge transfer mechanism showing both type-I and type-II band alignment at perovskite/BP and BP/MoS₂ interfaces, respectively. (b) The temporal response of MAPbI₃/BP/MoS₂ hybrid PD, inset shows the measured rise and fall times under 457 nm excitation. (c) The temporal response of the PD at zero bias mode under different illumination wavelengths. (d, e) Schematic and relative band diagram of MAPbI₃-MoS₂ BHJ/rGO PD on SiO₂/Si and flexible PEN substrates. (f) Comparison of the photoresponsivity and detectivity values at 660 nm as a function of illumination intensity of the PD with and without using MoS₂ on SiO₂/Si substrate. Figure reproduced with permission from: (a–c) ref.⁹¹. Copyright © 2019, American Chemical Society; (d–f) ref.²⁵⁷, John Wiley and Sons.

transport layer underneath MAPbI₃-TMD^{257,258}. The role of the TMDs here is to reduce the carrier recombination rate within the perovskite layer by trapping on type of charge carriers (electrons in these examples), while the other type (holes) transfers to the rGO channel. This results in high gain and enables the efficient separation of the photogenerated e-h pairs by the high carrier mobility rGO channel, hence higher responsivity^{257,258}. Figure 11(d, e) shows an example of the device structure with the relative band diagram for MAPbI₃-MoS₂ BHJ/rGO PD on SiO₂/Si and flexible polyethylene naphthalate (PEN) substrates, respectively²⁵⁷. Under illumination of 660 nm wavelength light ($V_g = 0$ V and $V_{ds} = 2$ V), the PD showed a maximum responsivity and detectivity of 1.08×10^4 A/W and 4.28×10^{13} Jones, respectively, five times higher than the device without MoS₂ (Fig. 11(f)). The maximum EQE was 2×10^6 % and the response time was < 45 ms. Moreover, when the same structure was examined on PEN substrate coated with ~20 nm SiO₂ layer, the device showed a slight change as compared with the rigid substrate with a stable performance after 1000 bending cycles²⁵⁷.

Phototransistor with MoS₂ quantum dots (QDs) encapsulated in a MAPbI₃ PVK film was demonstrated for more enhancement in the photodetection speed and extending the response range to longer wavelength²⁵⁹. The MoS₂ QDs were introduced as one of the commonly used methods to extend the response to IR²⁵⁹. CH₃NH₃I₃ isopropanol solution was used to encapsulate the MoS₂ QDs inside of MAPbI₃. After the dispersion of the MoS₂ QDs inside the solution, where the PbO film was immersed into this solution (to develop the perovskite film). During this growth process, the MoS₂ QDs were encapsulated in the MAPbI₃ granular. In this PD, interdigitated electrodes were utilised for more efficient charge extraction (high speed detection). Through the electric gate and optical light modulation, the effective photo-induced charge between the MAPbI₃/MoS₂ QDs interface enabled the PD to operate in the short wave infrared range with good performance²⁵⁹. At 1200 nm, the PD showed a fast detection speed (rise/fall times of 15/25 μ s) and high detectivity (5×10^{11} Jones) at high frequencies (22 kHz). This is the fastest PD among the reported MAPbI₃/TMD PDs²⁵⁹.

Besides the mostly reported MAPbI₃/ MoS₂ HS PDs, similar structures with WSe₂ were also reported. For instance, MAPbI₃/WSe₂ hybrid PD with a responsivity of 110 A/W was demonstrated, in which laser healing was

utilized to improve the device performance by passivation of unwanted defects in monolayer WSe₂²²¹. MAPbI₃/WSe₂ heterojunction with graphene electrodes exhibited distinct gate-tunable rectifying and photovoltaic effects²²⁹.

CsPbBr₃/TMD heterostructures

As discussed in previous sections, the general formula of halide perovskites is ABX₃. Based on the A cation metal halide perovskites can be divided into two families, organic-inorganic (e.g., MAPbI₃) and all-inorganic (e.g., CsPbI₃) metal halide perovskites. All-inorganic perovskite outperforms organic-inorganic hybrid perovskite in terms of ambient stability which is beneficial for real applications^{260,261}. For example, all-inorganic cesium lead halides represent an emerging class of materials with excellent properties required for PDs such as high carrier mobility, long carrier diffusion length, and excellent visible light absorption^{190,262}. Besides, the optical properties of CsPbX₃ nanocrystals (NCs) depend on their size and composition^{190,260}. Few studies have been conducted on CsPbBr₃/TMD HSs for photodetection application. For example, Song et al. reported CsPbBr₃/MoS₂ hybrid PD with greatly enhanced responsivity¹⁶⁴. The hybrid junction forms type II band alignment with a large band offset of 0.9 eV, which provides a strong driving force to separate the photogenerated carriers at the perovskite layer and suppress the radiative recombination. This led to an enhancement of the responsivity of the CsPbBr₃/MoS₂ hybrid PD (by nearly 20 or 1000 times at different incident optical powers) compared with CsPbBr₃ or MoS₂ based PDs.

Recently, heterojunction PD with 80 nm thickness CsPbBr₃ NCs and monolayer MoS₂ was demonstrated¹⁵⁹. This PD exhibited a superior response speed with 5.48 and 24.01 μ s for the rise and fall time, respectively. This fast response speed is attributed to the efficient charge transfer photogenerated electrons from CsPbBr₃ to MoS₂ and n-doping of the MoS₂. Another important reason for the high detection speed is the high quality of the HSs interface. Most of the reported perovskite/TMD HSs were prepared via wet transfer of the TMD on the substrate before coating with the perovskite material which results in poor interface during the transfer process. However, in this PD 1L MoS₂ was grown via direct CVD provided higher quality interface hence fast speed¹⁵⁹. Therefore, by carefully controlling the band alignment of perovskite/TMDs heterojunction PDs as well as the

interface quality, high speed photodetection of the PD can be achieved.

Most recently, flexible and broadband heterojunction PD (response range from 360 to 1064 nm) of CsPbBr₃ QDs and vertically layered MoS₂/Si (n-V-MoS₂/p-Si) was reported²⁶³. The highest measured responsivity was found to be 0.975 A/W at 808 nm illumination with a response time of 6.8/6.7 ms, and detectivity of 6.56×10^{11} Jones. The effective enhancement of the optoelectronic properties of the flexible PD is attributed to the light-harvesting capability and excellent electrical transporting property of the CsPbBr₃ QDs and efficient charge extraction in the perovskite/MoS₂ HJs as compared with MoS₂ PD²⁶³.

By making use of the high carrier mobility of WS₂ and remarkable optoelectronic properties of CsPbBr₃, single-crystalline CsPbBr₃ nanowires (NWs)/WS₂ PD with a high on/off ratio ($10^{9.83}$) was demonstrated²⁶⁴. This hybrid PD form type-I band structure and exhibited the highest reported detectivity (1.36×10^{14} Jones at 450 nm) among all the reported perovskite/TMDs PDs²⁶⁴. This detectivity exceeds that for the commercial Si PDs at the same wavelength. Upon illumination, the photogenerated charge carriers are transferred to WS₂ which suppresses the radiative recombination in the perovskite and increases the photodetection performance. Moreover, the hybrid PD shows a good switching behaviour under a low bias of 0.5 V with the rise and decay time characteristics of 2 ms. Strain-gated photocurrent and responsivity were also observed for the hybrid device on a flexible PEN substrate. These strain-gated characteristics are ascribed to the piezo-photonic effect of CsPbBr₃ NWs. The fundamental principle of the piezo-photonic effect was firstly proposed by Prof. Zhong Lin Wang in 2010²⁶⁵ which is out of the scope of this review. In brief, a piezoelectric potential is generated by applying a strain to a semiconductor with piezoelectricity to improve the performance of PDs via controlling the carrier generation, transport, separation and/or recombination^{265–267}.

Studies were also conducted to explore the mixed-dimensional structures of perovskite and TMDs for PD application^{255,268,269}. Wu et al.²⁵⁵ constructed hybrid PD of all-inorganic perovskite CsPbI_{3-x}Br_x QDs (PQDs) (cubic shapes with average size ~15 nm) as absorbing layer with channel MoS₂ monolayer. The device structure and the type-II band alignment are shown in Fig. 12(a). Upon illumination, the photogenerated electrons transferred from the PQDs to MoS₂ while holes remained in the

PQDs leading to a photogating effect. Figure 12(b) shows the photoresponsivity (7.7×10^4 A/W), detectivity (5.6×10^{11} Jones) and the EQE (10⁷ %), respectively at 532 nm. The high responsivity and EQE are attributed to the pronounced photogating effect in the heterojunction.

Additionally, mixed-dimensional vdWs nanohybrids of MoSe₂-CsPbBr₃ PD were recently reported¹⁶⁰, which showed a much higher photocurrent (photo/dark current ratio $\sim 2 \times 10^4$) as compared to the control devices owing to the synergistic effect of pronounced light-matter interactions followed by efficient charge separation and transportation¹⁶⁰.

Other perovskite/TMD heterostructures

Newly discovered group-10 transition metal dichalcogenides (such as PtSe₂ and PdSe₂) with tunable bandgaps down to ~0.1 eV are promising candidates for broadband and IR photodetection with high environmental stability, and high carrier mobility^{52,270–277}. A representative example for perovskite/PtSe₂ self-driven PD was demonstrated by Zhang et al. (schematically shown in Fig. 12(c))²⁷⁸. The self-driven PD revealed a wide spectrum response range from UV to NIR (300–1200 nm) with a large on/off ratio (5.7×10^3). Figure 12(d) shows the spectral responsivity and detectivity of the PD at 808 nm with a maximum of 117.7 mA/W and 2.91×10^{12} Jones, respectively. Additionally, the device exhibited an ultrafast response speed of 78/60 ns, which is the fastest among all the reported perovskite/TMDs PD (Fig. 12(e)).

Similarly, self-driven and broadband PD based on FA_{0.85}Cs_{0.15}PbI₃/PdSe₂ has been demonstrated²⁷⁹ (Fig. 12(f)). As compared with perovskite/PtSe₂ PD, using PdSe₂ showed a broader response range from deep UV to NIR (200 to 1550 nm), higher on/off ratio (6.46×10^4), higher responsivity (313 mA/W), and good detectivity (2.72×10^{13} Jones) at 808 nm illumination (Fig. 12(g)). Besides, the device exhibited polarization sensitivity of 6.04 to polarized light. Moreover, fast speed with rise/decay times of 3.5/4 μs, respectively (Fig. 12(h)). It is worth to note that the perovskite/group-10 TMD HJs exhibited the fastest reported PDs among all the reported perovskite/TMD PDs and have a great potential for high speed photodetection applications.

Unlike 3D organic-inorganic perovskite, 2D perovskite exhibit better environmental stability⁸⁴. Recently, a very low dark current (10^{-11} A) 2D (PEA)₂PbI₄/MoS₂ HS PD was reported¹⁵⁸. Such suppressed dark current was the consequence of an efficient interlayer charge

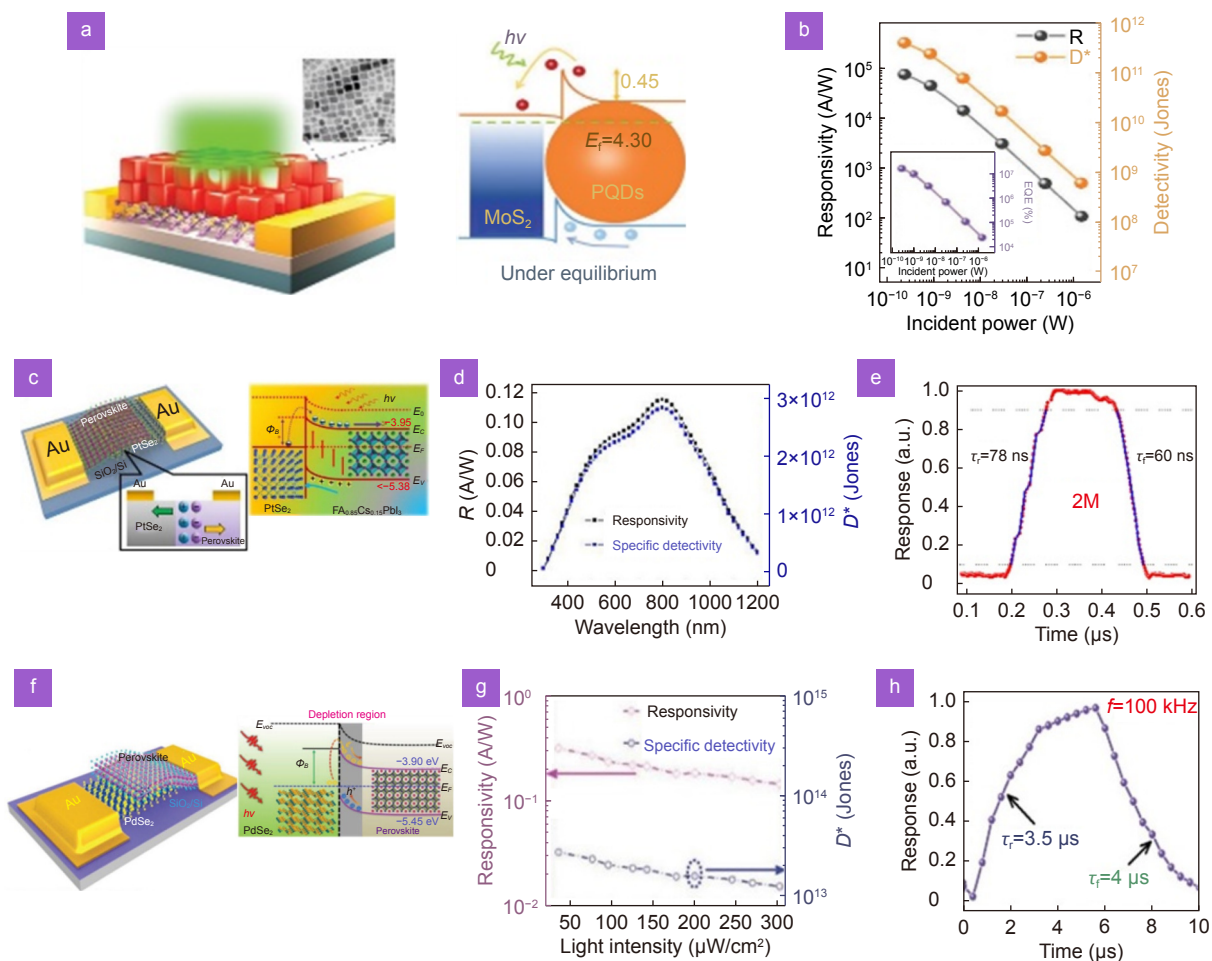


Fig. 12 | (a) Schematic and energy band alignment of CsPbI_{3-x}Br_x QDs/MoS₂ PD. (b) Photoresponsivity, specific detectivity, and EQE (inset) of CsPbI_{3-x}Br_x QDs/MoS₂ PD as a function of illumination powers at 532 nm. (c–e) Schematic (c), spectral responsivity and corresponding detectivity (d), and temporal photoresponse at 808 nm excitation (e) of Cs-doped FAPbI₃/PtSe₂ PD. (f–h) Schematic (f), responsivity and detectivity as a function of illumination intensity at 808 nm (g), and rise/fall times at 808 nm (h) of Cs-doped FAPbI₃/PdSe₂ hybrid PD. Figures reproduced/adapted with permission from: (a, b) ref.²⁵⁵, under the terms of the Creative Commons Attribution License; (c–e) ref.²⁷⁸, Copyright © 2018, American Chemical Society; (f–h) ref.²⁷⁹, under the terms of the Creative Commons Attribution License.

transfer from MoS₂ to (PEA)₂PbI₄. It was also found that the introduction of (PEA)₂PbI₄ reduces the carrier density of MoS₂ as the former could act as an electron reservoir. This subsequently led to devices with ultrahigh detectivity of 1.06×10^{13} Jones at 637 nm. Besides, the ambient stability of 2D perovskite as compared to 3D perovskite makes the 2D (PEA)₂PbI₄ a perfect passivation layer agent to passivate the defects on the surface of the MoS₂ resulting in a faster response time for the PD^{158,280}. Moreover, the PD showed the ability to operate in self-power mode. The photoresponse speed of the order of millisecond was reported, suggesting that with proper optimization spin-coating could produce a high-quality 2D perovskite layer required for high-performance PDs.

Different from non-lead-free perovskites which are harmful to environment, lead-free perovskite/TMD HSs

are good candidates for environmentally friendly materials for PD development^{242,281}. For example, in 2D Ruddlesden–Popper perovskite/MoS₂ PD²⁴², heterojunction of p-type (PEA)₂SnI₄ 2D perovskite on top of few-layer n-type MoS₂ was used as active materials for the PD, while graphene served as electrodes. This PD could operate without any external bias owing to the built-in potential at the heterojunction. Under zero bias at 451 nm illumination, the PD showed a maximum responsivity of 121 mA/W with rising and fall times of 34 and 38 ms, respectively, and the responsivity enhanced to 1100 A/W under 3 V bias. Another example for lead-free perovskite/TMD HSs is MA₃Bi₂Br₉/MoS₂ PD²⁸¹. The PD exhibited a good responsivity of 112 A/W, high detectivity of 3.8×10^{12} Jones, and a good response time of 0.3 ms at 530 nm LED illumination. More lead-free materials of

perovskite/TMD HSs need to be investigated for future lead-free PDs.

To sum up, many perovskite/TMDs heterojunction PDs have been demonstrated by utilizing the excellent absorption of the perovskite material and the superior electronic properties of 2D TMDs. Table 4 summarises the performance metrics of the reported hybrid perovskite/TMDs PDs. It may be observed that there is a trade-off between the performance parameters for different PDs. Apparently, PDs based on perovskite/TMD HSs exhibit high responsivity (orders of magnitude higher than commercially available PDs). However, their response speed is very slow. Figure 13(a) shows the re-

sponsivity and response speed of different perovskite/TMDs PD in comparison to the commercial Si and In-GaAs PDs and how competitive developing technology should proceed. It is known that the gain of the PD is proportional to the carrier mobility and the carrier lifetime. The high responsivity of the perovskite/TMDs PDs is often because of the origin of very high gain due to the very long carrier lifetimes. The carrier lifetime is the main parameter that controls the speed of the PD. The very long carrier lifetime is one of the main drawbacks that prevent these PDs from commercialisation, thus extensive efforts towards responsivity enhancement should be focused on improving the gain through increasing the

Table 4 | Device performance for several perovskite/TMD hybrid photodetectors (PDs).

Structure	Illumination wavelength (nm)	Responsivity (A/W)	Detectivity (Jones)	Response time (s)	Ref.
MAPbI₃/TMD PDs					
CH ₃ NH ₃ PbI ₃ /MoS ₂ /APTES	520	2.11×10 ⁴	1.38×10 ¹⁰	6.17/4.5	ref. ²³⁹
CH ₃ NH ₃ PbI ₃ /MoS ₂	638	1.1	9×10 ¹⁰	-	ref. ³³²
CH ₃ NH ₃ PbI ₃ /MoS ₂	500	3.3×10 ⁵	7×10 ¹¹	<0.025/<0.05	ref. ⁹⁰
CH ₃ NH ₃ PbI ₃ /MoS ₂	532	696×10 ⁻³	-	(50/16)×10 ⁻³	ref. ³³³
CH ₃ NH ₃ PbI ₃ / MoS ₂	White light	68.11	-	2.149/0.899	ref. ²⁵⁶
CH ₃ NH ₃ PbI ₃ /WSe ₂	532	1.1×10 ²	2.2×10 ¹¹	-	ref. ²²¹
CH ₃ NH ₃ PbI ₃ /WS ₂	White light & 470–627	17 @ white light	2×10 ¹² @ 505 nm	(2.7/7.5)×10 ⁻³	ref. ¹⁶³
CH ₃ NH ₃ PbI ₃ /WS ₂	White light	76.7×10 ⁻³	3.4×10 ⁹	(13.5/18.7)×10 ⁻³	ref. ³³⁴
CH ₃ NH ₃ PbI ₃ /WS ₂	532	43.6	-	-	ref. ¹⁶¹
CH ₃ NH ₃ PbI ₃ / MoS ₂ QDs	1200	920	5×10 ¹¹	(15/25)×10 ⁻⁶	ref. ²⁵⁹
CH ₃ NH ₃ PbI ₃ /BP/MoS ₂	457	11	1.3×10 ¹²	(0.15/0.24)×10 ⁻³	ref. ⁹¹
CH ₃ NH ₃ PbI ₃ -MoS ₂ BHJ/rGO	660	1.08×10 ⁴	4.28×10 ¹³	<45×10 ⁻³	ref. ²⁵⁷
CH ₃ NH ₃ PbI ₃ -WS ₂ NCs/ rGO	660	678.8	4.99×10 ¹¹	(<60/780)×10 ⁻³	ref. ²⁵⁸
CsPbBr₃/TMD PDs					
CsPbBr ₃ NS/MoS ₂	442	4.4	2.5×10 ¹⁰	(0.72/1.01)×10 ⁻³	ref. ¹⁶⁴
CsPbBr ₃ QDs/MoS ₂	488	1.02	-	-	ref. ²⁶⁸
CsPbBr ₃ QDs/MoS ₂	405	4.68×10 ⁴	-	(7.5/8)×10 ⁻³	ref. ²⁶⁹
CsPbBr ₃ QDs/V-MoS ₂ /Si	808	0.975	6.56×10 ¹¹	(6.8/6.7)×10 ⁻³	ref. ²⁶³
CsPb _{1-x} Br _x QDs/MoS ₂	532	7.7×10 ⁴	5.6×10 ¹¹	0.59/0.32	ref. ²⁵⁵
CsPbBr ₃ NCs/MoS ₂	405	24.3	3×10 ¹²	(5.5/24)×10 ⁻⁶	ref. ¹⁵⁹
CsPbBr ₃ NCs/MoS ₂	532	6.4×10 ²	3.38×10 ¹¹	0.092/-	ref. ³³⁵
CsPbBr ₃ NW/WS ₂	450	57.2	1.36×10 ¹⁴	(2/2)×10 ⁻³	ref. ²⁶⁴
Other perovskite/TMD PDs					
(CH ₃ NH ₃) ₃ Bi ₂ Br ₉ /MoS ₂	530	112	3.8×10 ¹²	(0.3/0.3)×10 ⁻³	ref. ²⁸¹
(PEA) ₂ PbI ₄ /MoS ₂	637	16.8	1.06×10 ¹³	(6/4)×10 ⁻³	ref. ¹⁵⁸
G/(PEA) ₂ SnI ₄ /MoS ₂ /G	451	0.121	8.09×10 ⁹	(34/38)×10 ⁻³	ref. ²⁴²
Cs-doped FAPbI ₃ /PtSe ₂	808	117.7×10 ⁻³	2.91×10 ¹²	(78/60)×10 ⁻⁹	ref. ²⁷⁸
Cs-doped FAPbI ₃ /PdSe ₂	808	313×10 ⁻³	2.72×10 ¹³	(3.5/4)×10 ⁻⁶	ref. ²⁷⁹
Triple cation perovskites/MoS ₂	520	342	1.14×10 ¹²	(27/21)×10 ⁻³	ref. ³³⁶

PDs: photodetectors, APTES: (3-aminopropyl) triethoxysilane, BHJ bulk heterojunction, G: graphene, rGO: reduced graphene oxide, Triple cation perovskites: Cs_{0.05}(MA_{0.17}FA_{0.83})_{0.95}Pb(I_{0.83}Br_{0.17})₃, PEA: C₆H₅C₂H₄NH₃, NS: nanosheets, QDs: quantum dots, NCs: nanocrystals, V-MoS₂/Si: vertically layered MoS₂/Si, NWs: nanowires.

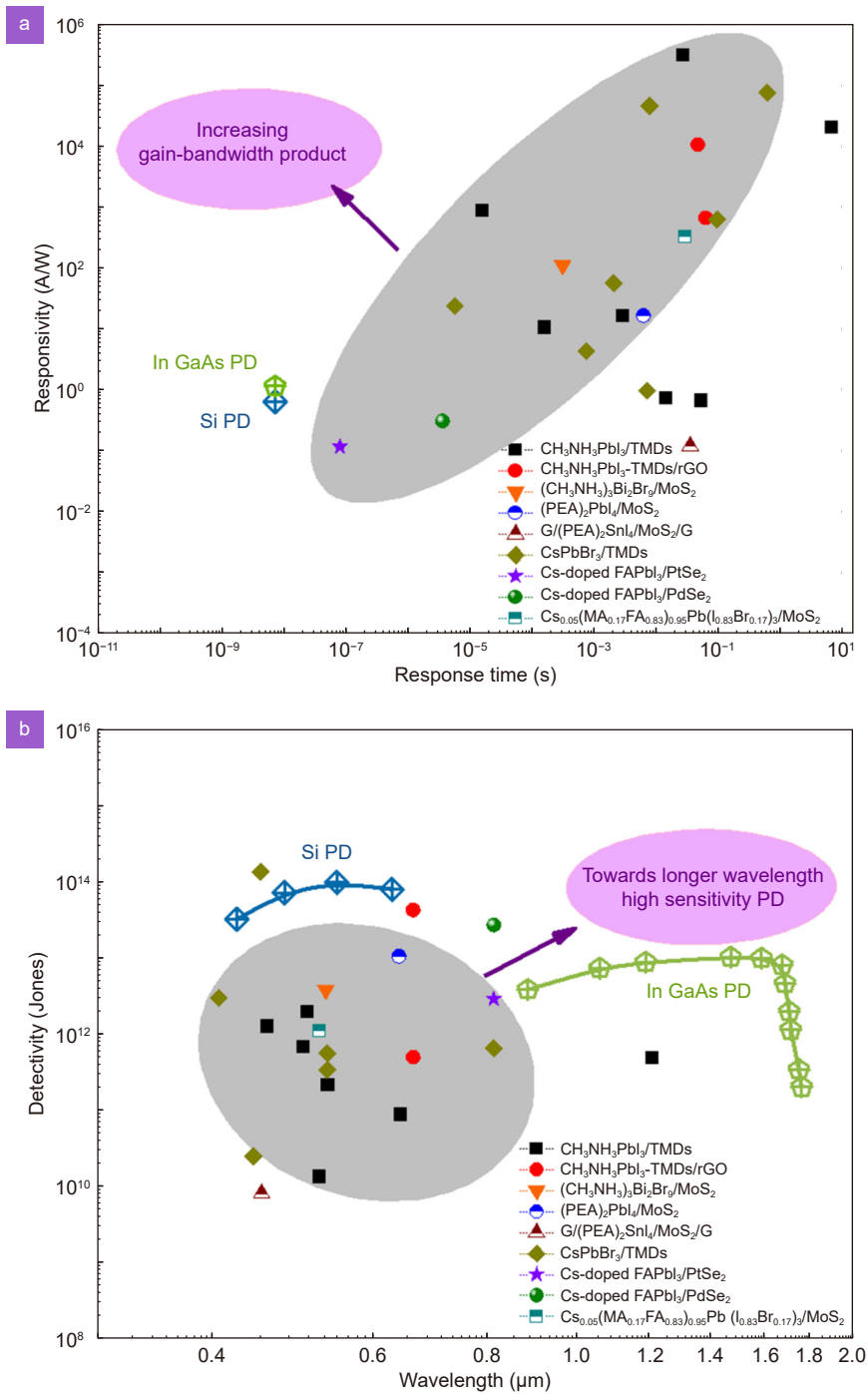


Fig. 13 | Summary of performance metrics of perovskite/TMD PDs in comparison with commercial PDs. (a) Current responsivity against response time of perovskite/TMD PDs in comparison with that for the commercial Si and InGaAs. The marked area on the left showing the goal for future development by improving the gain-bandwidth product. **(b)** Detectivity comparison between perovskite/TMD PDs and commercial Si and InGaAs PDs. The marked area on the right showing the ultimate target for future development through extending the sensitivity range of the PDs to longer wavelength regime which lacks of candidates with suitable bandgap values. The data for perovskite/TMD PDs were taken from the references shown in Table 4.

carrier mobility rather than prolonging carrier lifetime.

Figure 13(b) shows the detectivity of PDs based on perovskite/TMDs at different wavelengths compared to the commercial PDs in the same wavelength range. It is

worth to note that the sensitivity of few heterojunction PDs exceeds the commercial PDs that work in the same wavelength range. However, their response speeds are sacrificed as compared with commercial detectors.

Again, more research is required to enhance the performance of the PDs without sacrificing other key figures of merit. It could be also observed that the sensitivity of most perovskite/TMD PDs are in the visible to near IR range due to the band gap of the parent materials as described in earlier sections. Development of the current materials and structures to demonstrate high performance and highly sensitive PDs in longer wavelengths regime is urgently in need.

Solar cells

By virtue of their high carrier mobility for efficient charge transport^{282,283}, tunable work function *via* composition tuning or surface functionalization or elemental doping^{173,284}, and solution processability^{285–287}, TMD has been used as either a standalone charge transporting layer or a complementary interlayer in perovskite solar cells (PSCs). For ease of comparison, Table 5 shows the main performance parameters of perovskite/TMDs-based solar cells, which are discussed further in detail. Kim et al. demonstrated the use of MoS₂ and WS₂ as hole-transporting materials (HTMs) to replace conventional poly(3,4-ethylene dioxythiophene): poly(styrene sulfonate) (PEDOT: PSS) in planar “inverted” device architecture in which the materials serve as underlying layers to the perovskite solar absorber²⁸⁸. Both TMDs were formed *via* a thermolysis process where the spincoated films of (NH₄)MoS₄ and (NH₄)WS₄ precursor solutions were subjected to H₂ and N₂ atmosphere at elevated temperatures. As a result of their suitable work functions, which were measured to be 4.95 eV and 5.0 eV for MoS₂ and WS₂, respectively, solar cells exhibit similar performances as the control devices with a power conversion effi-

ciency (PCE) of over 9%, suggesting that 2D materials can be promising candidates as HTMs for efficient PSCs.

Following that, several seminal papers were published using the same materials and solar cells stack, though the procedures in which the TMDs were fabricated varied, highlighting the materials advantage in terms of processing versatility^{289–291}. For example, Dasgupta, et al., and Kakavelakis, et al., demonstrated the use of liquid phase exfoliation to produce MoS₂ flakes from their bulk forms^{289,290}. In the process, centrifugation was carried out upon the ultrasonication step to separate the exfoliated MoS₂ flakes from the thicker or unexfoliated particles (i.e., sedimentation-based separation approach) and thus facilitating the formation of uniform and homogeneous thin films of the materials. Meanwhile, Huang, et al., developed water-based method to fabricate the MoS₂ and WS₂ nanosheets. This was achieved through lithium intercalation reaction in which the bulk TMDs were lithiated by n-butyllithium, before the Li-intercalated TMDs were then exfoliated into a few or a single layer *via* forced hydration²⁹¹. In all cases, the TMDs were used as HTMs where improvements in terms of device performance (PCE of over 15%; Fig. 14(a)) and shelf stability (lifetime of almost 60 days; Fig. 14(b)) in comparison to the first report were observed^{289–291}.

TMDs can also serve as electron transporting material (ETM) in PSCs and the first report on its utilization was documented by Singh et al.¹⁷⁶. They synthesized MoS₂ directly on the glass/fluorine doped tin oxide (FTO) substrate *via* microwave irradiation. The resulting thin film was highly transparent (thickness of 50–70 nm) and electrically conductive in the vertical direction. Most importantly, the material features a suitable work function of

Table 5 | Device performance for perovskite/TMD solar cells.

Structure	PCE (%)	J_{sc} (mA cm ⁻²)	V_{oc} (V)	FF (%)	Ref.
MAPbI ₃ /MoS ₂	16.09	20.9	0.98	69	ref. ¹⁷⁴
MAPbI ₃ /MoS ₂	14.7	20.98	0.99	75.83	ref. ²⁹⁷
MAPbI ₃ /MoS ₂	13.3	21.5	0.93	66.7	ref. ³⁰¹
MAPbI ₃ /MoS ₂	13.14	21.7	0.89	63.8	ref. ¹⁷⁶
MAPbI ₃ /SnS ₂	13.04	19.29	0.68	61	ref. ²⁹³
MAPbI _{3-x} Cl _x /MoS ₂	9.53	14.89	0.96	0.67	ref. ²⁸⁸
MAPbI _{3-x} Cl _x /WS ₂	8.02	15.91	0.82	0.64	ref. ²⁸⁸
MAPbI ₃ /MoS ₂ /PTAA	16.42	20.71	1.01	78.41	ref. ²⁸⁹
FASnI ₃ /WSe ₂	10.2	22.3	0.63	73.2	ref. ²⁹⁵
FA _{0.85} MA _{0.15} PbI _{0.85} Br _{0.15} /MoS ₂	14.34	21.47	0.889	64.14	ref. ³⁰²
FA _{0.75} MA _{0.15} CS _{0.1} PbI _{2.65} Br _{0.35} /SnS ₂	20.12	23.55	1.161	73	ref. ²⁹⁴
CS _{0.05} MA _{0.05} FA _{0.9} PbI _{2.7} Br _{0.3} /WS ₂	20.1	22.38	1.15	79.6	ref. ²⁹⁶
CS _{0.05} [MA _{0.13} FA _{0.87}] _{0.95} Pb(I _{0.87} Br _{0.13}) ₃ /WS ₂	18.21	22.24	1.12	0.731	ref. ²⁹²

PCE: power conversion efficiency, J_{sc} : short-circuit current, V_{oc} : open-circuit voltage, FF: fill factor. PTAA: poly(triarylamine).

4.43 eV, which stands between that of conductive FTO electrode (4.7 eV) and perovskite conduction band level (3.75 eV), allowing for spontaneous electron extraction to take place. An average PCE of over 13% was achieved from the solar cells made out of the materials, which was comparable to those fabricated using the TiO_2 and SnO_2 as the ETMs at that time. Malek et al. demonstrated that few-atom thick 2H- WS_2 ETM could also effectively facilitate a fast interfacial photo-generated charge transfer in the device as a result of surface collective motion of exciton²⁹². An ultrasonic spray pyrolysis technique was applied to grow the large-scale planar TMD nanosheets on top of the clean indium-doped tin oxide (ITO) substrate. Although the resulting PSCs performance showed a dependency on the thickness of the WS_2 nanosheet, an average PCE of almost 18% could be obtained from the optimized conditions (Fig. 14(c, d)). Such figure is almost two times better than those devices without the WS_2 nanosheets ETL, providing strong evidence that the WS_2 nanosheets ETL has an excellent capability as an effi-

cient electron extractor.

The devices with TMDs as the HTMs are of “normal” architecture. Therein, the ETM is located below the perovskite layer, which means that the relative position of TMD and perovskite in this case is the same as that when TMD is used as HTM in the inverted stack. Such relative position provides several advantages. First, it allows more diverse deposition techniques to be applied. For example, electro-spraying and hydrothermal methods can be used to directly synthesize the materials on top of the conductive substrates,^{174,293} which otherwise would be difficult to carry out when the perovskite absorber acts as the underlying layer as the conditions in which the processes were carried out would degrade the material. It is also possible to alloy TMDs with conductive species, such as graphene, to construct next-generation of transparent conductive electrode that has high transmittance in the visible region, easily adjustable work function, and mechanical flexibility, while maintaining a low production cost¹⁷⁵. All of these contribute to bringing perovskite

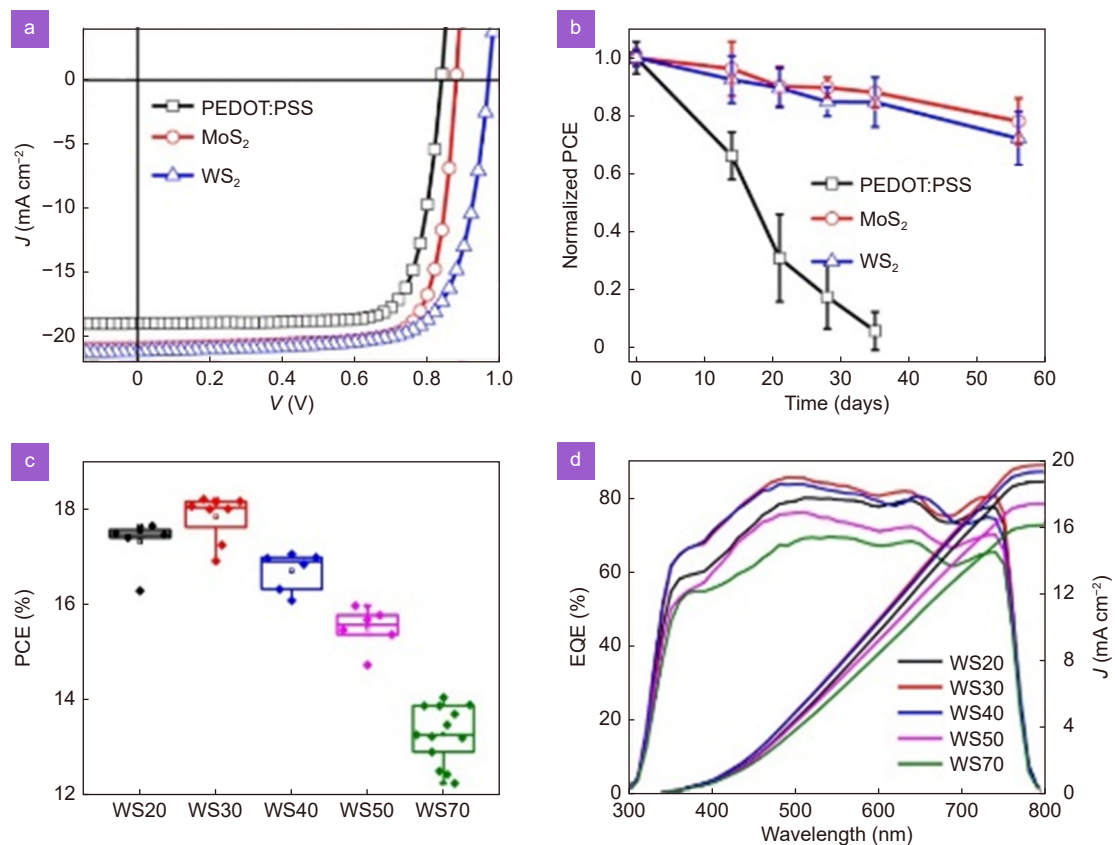


Fig. 14 | (a) Representative J - V curve of PSCs with PEDOT: PSS, MoS_2 , and WS_2 as the hole transporting material. (b) Plots of PCEs of PSCs based on PEDOT: PSS, MoS_2 , and WS_2 as the function of the storage time. For each group of measurements, 20 cells were adopted for analysis. (c) The statistic plot for power conversion efficiency of PSCs using different thicknesses of WS_2 as the electron transporting material. (d) EQE spectra and integrated current density (J) of the corresponding devices. Figure reproduced with permission from: (a, b) ref.²⁹¹, Copyright © 2017, American Chemical Society; (c, d) ref.²⁹², John Wiley and Sons.

photovoltaic technology closer to commercialisation through development of more economical and scalable fabrication of the device or module stack.

More importantly, the underlying TMD layer also allows for better control over perovskite film crystallization. In particular, big perovskite grains with preferred growth orientation or stacking self-assembly can be achieved as a result of interaction with the preformed TMD during the deposition processes^{294–296}. Such templating strategy often gives good PCEs because the resulting perovskite would feature defect-free characteristics which lead to improved optoelectronic properties such as charge transport. For instance, Zhao et al., demonstrated that 2D multilayer SnS₂ sheet structure could trigger a heterogeneous nucleation of the perovskite precursor solution, while being used as an underlying ETM²⁹⁴. The intermolecular Pb-S interactions between perovskite and the 2D material were found to passivate the interfacial trap states, which suppressed charge recombination and subsequently facilitated electron extraction required for balanced charge transport at interfaces between ETM/perovskite and ETM/perovskite. Eventually, highly efficient planar perovskite solar cells,

with PCE of over 20% could be achieved with the proposed material.

Apart from being effective charge transporting layers on their own, TMDs can also be used as interfacial or buffer layers in PSCs in order to enhance the device performance and stability. Most strategies typically place TMDs below the perovskite layer owing to the advantages discussed above^{289,295–297}. A few examples include those reported by Wang et al. who used atomically-thin 2D MoS₂, WS₂, and WSe₂ with smooth and defect-free surfaces as growth templates for spin-coated FASnI₃ perovskite films²⁹⁵. This resulted in vdWs epitaxial growth of perovskite grains along the (100) plane together with increased grain size on top of NiO_x HTM (Fig. 15(a)). Such strategy was found to be effective to optimize perovskite interface property, as evident from the PCE of 10.47% obtained for the champion WSe₂-incorporated device, which is among the highest efficiency for FASnI₃-based PSCs. The same strategy could also be extended to other perovskite systems, such as the prototypical MAPbI₃²⁹⁷ and the well-known “triple cation” composition of chemical formula Cs_xMA_yFA_(1-x-y)PbI₂Br_{3-z}²⁹⁶. It was found that the presence of pre-deposited 2D TMD flakes

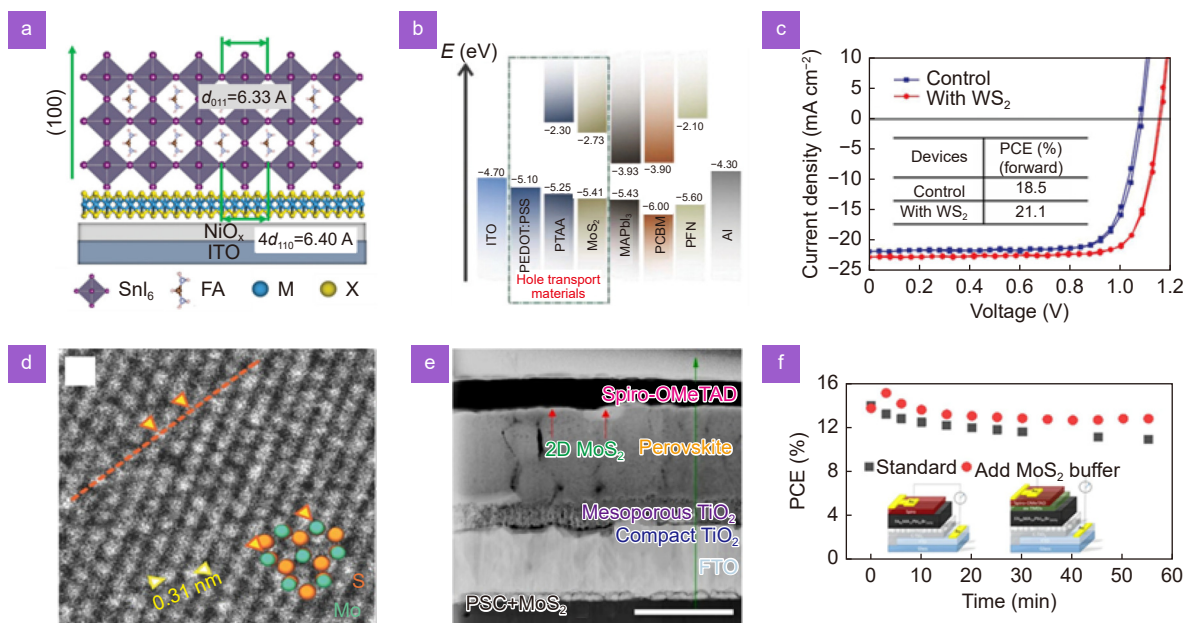


Fig. 15 | (a) Schematic diagram of the vdW epitaxial growth of the perovskite crystallizes on a TMD (e.g., WSe₂) surface. (b) Energy-band diagram under flat-band conditions of the fabricated planar inverted PSCs with different materials as the HTL. (c) *J*–*V* curves the best performing PSCs with and without WS₂ interlayer. (d) HRTEM image of one of the MoS₂ flakes (synthesized via a solvent-exchange process upon liquid phase exfoliation) oriented in the [001] zone axis having a 2H structure (a sketch of the arrangement of Mo and S atoms in this structure and orientation is superimposed on the HRTEM image). (e) The cross-sectional TEM image of a PSC with 2D MoS₂ nanoflakes acting as HTL buffer layer. The scale bar is 1 μm (f) Operational stability of PSCs with and without a MoS₂ buffer layer³⁰². Figures reproduced/adapted with permission from: (a) ref.²⁹⁵, under the terms of the Creative Commons Attribution License; (b) ref.²⁸⁹, (c) ref.²⁹⁶, (d) ref.³⁰¹. John Wiley and Sons; (e, f) ref.³⁰², under a Creative Commons Attribution 4.0 International License.

could result in perovskite films with preferred orientation, high crystallinity, and low defect density, regardless of the nature of the underlying HTM (e.g., PEDOT:PSS or PTAA). The presence of TMDs can also enhance charge extraction at the interface and suppress interfacial charge recombination in PSCs (Fig. 15(b)), which ultimately augmented in PCEs of over 18% and 20% for MAPbI₃- and triple cation-based devices, respectively (Fig. 15(c))^{296,297}.

In addition to improving device performance, the presence of TMD buffer layer also improves PSCs long term stability. This is because it can prevent a direct contact between the perovskite and conventional HTMs (such as PEDOT: PSS or F4TCNQ-doped PTAA) that could otherwise induce degradation of the former as a result of the hydrophilicity and acidic nature of the latter. It was hypothesized that TMD is able to capture water molecules (e.g., MoS₂ basal planes) *via* strong vdWs interaction, providing protective role for the perovskites^{298–300}. Inverted PSCs with configuration of Glass/ITO/PEDOT:PSS/MoS₂/CH₃NH₃PbI₃:MoS₂/PCBM/Bphen/Ag was found to maintain 87% of its initial performance after 20 days of storage, while the device based on pristine CH₃NH₃PbI₃ film without MoS₂ buffer layer only retained 36% of the initial PCE over the same period of testing²⁹⁷. Meanwhile, devices based on ITO/PTAA/MoS₂/perovskite/PCBM/PFN/Al structure retained 80% (T₈₀) of their initial performance after 568 h of continuous stress test, where the reference device without MoS₂ reached T₈₀ after only ≈171 h of the applied stress test²⁸⁹. The findings provide evidence that TMDs can be a promising tool to not only fabricate high efficiency, but also stable perovskite photovoltaic devices.

Although it is more challenging, there are also advantages of putting TMD over a perovskite layer. However, TMDs are typically used as interlayers rather than charge transporting layers through this approach^{301,302}. It has been reported that as a result of their better intrinsic stability, depositing TMD on top of perovskite would serve as a protecting layer that could stabilize the whole device stack^{301,302}. This is particularly important because environmental and operational stabilities of perovskite are one of the key issues to address before the technology can be commercially viable. In this regard, Capasso et al. carried out a solvent-exchange process upon liquid phase exfoliation in order to deposit the MoS₂ flakes on top of the perovskite layer³⁰¹ (Fig. 15(d)). This is because the solvent used for liquid phase exfoliation (i.e., N-methyl-

2-pyrrolidone; NMP) could redissolve the perovskite film during the processing. In addition, NMP has a high boiling point (≈ 202 °C), and post-processing treatments are typically required to remove its residues on the flakes after the process, which could potentially create more damage to the underlying perovskites. Eventually, device stack consisting of glass/FTO/compact-TiO₂/mesoporous-TiO₂/CH₃NH₃PbI₃/MoS₂/Spiro-OMeTAD/Au solar cells could be realized. Here, the MoS₂ flakes have a two-fold function, acting both as a protective layer, by preventing the formation of shunt contacts between the perovskite and the Au electrode, and as an interlayer that promotes charge transport from the perovskite to the Spiro-OMeTAD. As prepared PSC demonstrates a PCE of 13.3%, along with a significantly longer lifetime relative to reference PSC without MoS₂ over 550 hours of storage stability testing (93% of the initial PCE with MoS₂ vs. 66% for the control).

Similar method was also used by Liang et al. who introduced 2D MoS₂ and MoSe₂ nanoflakes as a buffer layer between FA₈₅MA₁₅PbI₈₅Br₁₅ perovskite and Spiro-OMeTAD HTM³⁰² (Fig. 15(e)). As expected, 2D TMDs act both as a protective layer and an additional HTL of PSCs. This kind of PSCs achieved a relatively high PCE of 15 %, together with a much-improved operational stability compared to the standard PSCs (Fig. 15(f)). After 1 hour of continuous Sun light illumination in ambient air at room temperature, for example, the PCE of the PSC with a 2D TMD buffer layer could maintain ca. 93% of initial value, while the PCE of the standard PSC dropped dramatically to around 78% of initial efficiency. The results pave the way towards the implementation of 2D TMD nanoflakes as a material able to boost the shelf life of PSCs and further provide the opportunity to fabricate large-area PSCs in view of their commercialization.

Conclusions and outlook

As two emerging and promising materials for optoelectronic applications, perovskites and TMDs are given a brief review in this paper of the fundamental properties and their respective heterostructures (HSs) and are discussed in details of the perovskite/TMD HSs from their synthesis to device applications in photodetectors (PDs) and solar cells. Comprehensive review of the up-to-date development of the perovskite/TMD HSs is provided with detailed choices of materials, fabrication methods, physical and chemical phenomena, and key performance parameters, assisted with illustration figures and

summary tables.

The field is attracting more interests and continues to develop rapidly. There are many more studies in materials and physics need to be done and many more potential are waiting to be explored. Below are some of our perspectives on the challenges and future research topics.

Some fundamental properties of TMD/perovskite HSs have been studied by now including PL quenching, enhancement, and shift due to interlayer charge transfer, interface-related broadband emission, and selective spin injection. However, some other potential properties, have yet not been confirmed experimentally. For example, some of TMDs³⁰³ and 2D perovskites³⁰⁴ are known to exhibit in-plane anisotropy. Optical anisotropy is important for fabricating novel optoelectronic devices (for example, polarized light detectors). Further studies of the anisotropic properties of the TMD/perovskite HSs are needed.

More fundamental analysis of the optical properties would be useful, particularly at low temperatures. Temperature-dependent analysis can provide useful information about recombination mechanism and interactions with phonons; also, it allows resolving the fine spectral components, which are missing at room temperature. Authors of several works¹⁶¹ attempted to perform a detailed low-temperature study of the HSs, however, it was unsuccessful due to the structural phase transition of the perovskite component. To avoid this, 2D perovskites that do not undergo a phase change should be chosen, for example, $C_6H_5C_2H_4NH_3PbI_4$ 2D perovskite.

High pressure is a powerful tool to manipulate the crystal and band structure of materials, which will allow adjusting band alignment and studying the structure-property relations. In TMDs HSs, applying high pressure enabled direct observation of the transition from intra to interlayer excitons via in-situ PL spectroscopy³⁰⁵. We expect enhancement of interlayer coupling by applying high pressure in perovskite/TMD HSs.

Both TMDs and perovskites are light-emitting materials that have sparked a rise in development for next-generation displays and light-emitters. The HSs with TMDs monolayers and perovskites come out of the expectations to combine the advantages of the two material systems. The strongly bound excitons facilitate the high-efficiency light-emitting. The very best perovskite LEDs can electrically illuminate with an external quantum efficiency of more than 20%^{306–309}. Light emission from TMD monolayers via p-n junctions^{59,310,311} or Joule heat-

ing³¹² as well as lasing from both TMD monolayers and TMDs HSs have been demonstrated^{62,63,65,66,127}. Large area materials growth or synthesis is critical for future device applications. Highly emissive quasi-2D perovskite films can be fabricated using spin-coated self-assembled multiple-quantum-well structure^{313–315}. Wafer scale single-crystal TMD monolayers have been epitaxially grown by chemical vapor deposition^{316,317}. The synthesis and fabrication of perovskite/TMD HSs in large area high quality are still a grand challenge and more research is needed to expand the versatility of choice of materials, and to understand the interface and improve the yield.

In photodetection, there is always a trade-off between the performance parameters for different PDs based on the materials and the structures engaged. Although type-II has the advantage of fast charge separation which is preferable for PDs, the speed of PDs based on perovskite/TMDs HSs is still low and needs innovations to improve while keeping the high responsivity. Other types of 2D materials like semimetals, new interfacial layers to manipulate charge transfer, or incorporation of quantum wire and quantum dots could be approaches for consideration and investigation.

The absorption of perovskites/TMDs HSs are mainly in the visible and near IR range due to the bandgap of the parent materials and their relative band alignment. In the important mid-far-IR range that has finger-print spectral resonance with many molecules, graphene and other narrow gap 2D semiconductors such as black phosphorus (BP) have been employed for PD development, nevertheless with drawbacks including large dark current in graphene-based PDs and low ambient stability in BP based PDs^{52,318}. The unique features of interlayer excitons in 2D TMDs open up many opportunities for fascinating new devices¹¹⁶. Recently, we demonstrated interlayer exciton based PD based on WS_2/HfS_2 HSs with good performance at room temperature in mid-IR range¹¹⁷. Moreover, it was reported recently that type-II interfaces could be engineered to have momentum of the CBM and VBM from two different layers respectively matched at the Γ point³¹⁹. In that case, radiative optical transitions are possible at the interfaces regardless of the type of semiconductor material (direct or indirect), the lattice constant, the rotational and/or translational alignment³¹⁹. Extending these strategies to perovskite/TMD HSs with greatly enriched choice of materials could make it easier to further extend to long wavelengths regime with better performance and improved stability.

For solar cells, a sharp escalation of interest is seen in recent years in scaling up PSCs towards the fabrication of modules as the PCEs of the lab-scale cells starting to plateau at 25% mark^{325,320}. In this regard, deposition methods of high quality TMDs that feature large area coating uniformity, high throughput capability, minimal material wastage, as well as compatibility with sheet-to-sheet and roll-to-roll coating systems would be of great importance in order to enjoy the advantages from the perovskite/TMD HSs³²¹. In addition, more versatile deposition techniques that allow the TMD to be placed on top of perovskite without causing any damage to the underlying layer could also potentially bring a bigger impact as it would significantly improve the devices operational and environmental stabilities^{301,302}. Passing some of the internationally recognized testing protocols, such as International Electrotechnical Commission (IEC) 61215:2016 Damp Heat and Humidity Freeze tests, would bring the perovskite PV technology closer to commercialisation^{322,323}. Besides, from physical point of view, any strategy that can allow PSCs to absorb more light, especially in the IR regime could push the state-of-the-art PCE to higher value as a result of more current generation^{324,325}. This is another big opportunity for perovskite/TMD HSs because the suitable band gap and energy level could be achieved by tuning the chemical composition and layer thickness of the TMDs and the band alignment of the HSs^{105,298,326,327}. Endowed with groups or atoms that can also passivate defects on the perovskite surfaces and interfaces, TMDs represent very promising materials to push the solar cell efficiency higher not only in terms of current density generation, but also other photovoltaic parameters, such as open-circuit potential and fill-factor³²⁸.

Lastly, perovskite/TMDs HSs can potentially be used in photocatalysis applications due to their advantages in the form of high extinction coefficients, optimal and tunable band gaps, high photoluminescence quantum yields and long e-h diffusion lengths. Photocatalysts are critical to many processes such as hydrogen production from water splitting, processing of carbon dioxide and reducing its emissions, and decomposition of polluting organic substances^{329,330}. For instance, MAPbI₃/MoS₂ HS can be utilised as a photocatalyst for the generation of H₂ controlled by visible light³³¹. The highest achieved H₂ release rate is 121 times higher than that of the pristine MAPbI₃ and significantly exceeds that of the MAPbI₃/Pt/C composite, along with good stability with a

continuous H₂ release reaction³³¹. In addition, one of the main reasons for the non-ecology of perovskites is the presence of lead in their composition. Lead-free Cs₂SnI₆/SnS₂ has been tested as a photocatalyst for CO₂ utilisation and the photoelectrochemical performance of the HS are several times higher than the pristine SnS₂, which shows the great potential of using HSs for environmental purposes⁹⁴.

References

1. Green MA, Dunlop ED, Hohl-Ebinger J, Yoshita M, Kopidakis N et al. Solar cell efficiency tables (version 56). *Prog Photovoltaics Res Appl* **28**, 629–638 (2020).
2. Niemann RG, Kontos AG, Palles D, Kamitsos EI, Kaltzoglou A et al. Halogen effects on ordering and bonding of CH₃NH₃⁺ in CH₃NH₃PbX₃ (X = Cl, Br, I) hybrid perovskites: a vibrational spectroscopic study. *J Phys Chem C* **120**, 2509–2519 (2016).
3. Jung EH, Jeon NJ, Park EY, Moon CS, Shin TJ et al. Efficient, stable and scalable perovskite solar cells using poly(3-hexylthiophene). *Nature* **567**, 511–515 (2019).
4. Saliba M, Matsui T, Domanski K, Seo JY, Ummadisingu A et al. Incorporation of rubidium cations into perovskite solar cells improves photovoltaic performance. *Science* **354**, 206–209 (2016).
5. Jiang Q, Zhao Y, Zhang XW, Yang XL, Chen Y et al. Surface passivation of perovskite film for efficient solar cells. *Nat Photonics* **13**, 460–466 (2019).
6. Chen Q, De Marco N, Yang Y, Song TB, Chen CC et al. Under the spotlight: the organic–inorganic hybrid halide perovskite for optoelectronic applications. *Nano Today* **10**, 355–396 (2015).
7. Serpetzoglou E, Konidakis I, Kourmoulakis G, Demeridou I, Chatzimanolis K et al. Charge carrier dynamics in different crystal phases of CH₃NH₃PbI₃ perovskite. *Opto-Electron Sci* **1**, 210005 (2022).
8. Marshall KP, Walker M, Walton RI, Hatton RA. Enhanced stability and efficiency in hole-transport-layer-free CsSnI₃ perovskite photovoltaics. *Nat Energy* **1**, 16178 (2016).
9. Saparov B, Mitzi DB. Organic–inorganic perovskites: structural versatility for functional materials design. *Chem Rev* **116**, 4558–4596 (2016).
10. Zhao YX, Zhu K. Organic–inorganic hybrid lead halide perovskites for optoelectronic and electronic applications. *Chem Soc Rev* **45**, 655–689 (2016).
11. Tsai H, Asadpour R, Blancon JC, Stoumpos CC, Durand O et al. Light-induced lattice expansion leads to high-efficiency perovskite solar cells. *Science* **360**, 67–70 (2018).
12. Yang S, Chen SS, Mosconi E, Fang YJ, Xiao X et al. Stabilizing halide perovskite surfaces for solar cell operation with wide-bandgap lead oxysalts. *Science* **365**, 473–478 (2019).
13. Tress W, Domanski K, Carlsen B, Agarwalla A, Alharbi EA et al. Performance of perovskite solar cells under simulated temperature-illumination real-world operating conditions. *Nat Energy* **4**, 568–574 (2019).
14. Birowosuto MD, Cortecchia D, Drozdowski W, Brylew K, Lachmanski W et al. X-ray scintillation in lead halide perovskite crystals. *Sci Rep* **6**, 37254 (2016).

15. Yakunin S, Sytnyk M, Kriegner D, Shrestha S, Richter M et al. Detection of X-ray photons by solution-processed lead halide perovskites. *Nat Photonics* **9**, 444–449 (2015).
16. Yang ZQ, Deng YH, Zhang XW, Wang S, Chen HZ et al. High-performance single-crystalline perovskite thin-film photodetector. *Adv Mater* **30**, 1704333 (2018).
17. Li XM, Yu DJ, Chen J, Wang Y, Cao F et al. Constructing fast carrier tracks into flexible perovskite photodetectors to greatly improve responsivity. *ACS Nano* **11**, 2015–2023 (2017).
18. Hu X, Zhang XD, Liang L, Bao J, Li S et al. High-performance flexible broadband photodetector based on organolead halide perovskite. *Adv Funct Mater* **24**, 7373–7380 (2014).
19. Lan CY, Dong RT, Zhou ZY, Shu L, Li DP et al. Large-scale synthesis of freestanding layer-structured PbI_2 and MAPbI_3 nanosheets for high-performance photodetection. *Adv Mater* **29**, 1702759 (2017).
20. Wangyang PH, Gong CH, Rao GF, Hu K, Wang XP et al. Recent advances in halide perovskite photodetectors based on different dimensional materials. *Adv Opt Mater* **6**, 1701302 (2018).
21. Ji L, Hsu HY, Lee JC, Bard AJ, Yu ET. High-performance photodetectors based on solution-processed epitaxial grown hybrid halide perovskites. *Nano Lett* **18**, 994–1000 (2018).
22. Tan ZJ, Wu Y, Hong H, Yin JB, Zhang JC et al. Two-dimensional $(\text{C}_4\text{H}_9\text{NH}_3)_2\text{PbBr}_4$ perovskite crystals for high-performance photodetector. *J Am Chem Soc* **138**, 16612–16615 (2016).
23. Lin YH, Pattanasattayavong P, Anthopoulos TD. Metal-halide perovskite transistors for printed electronics: challenges and opportunities. *Adv Mater* **29**, 1702838 (2017).
24. Pan WC, Wu HD, Luo JJ, Deng ZZ, Ge C et al. $\text{Cs}_2\text{AgBiBr}_6$ single-crystal X-ray detectors with a low detection limit. *Nat Photonics* **11**, 726–732 (2017).
25. Wei HT, Huang JS. Halide lead perovskites for ionizing radiation detection. *Nat Commun* **10**, 1066 (2019).
26. Pedesseau L, Saporì D, Traore B, Robles R, Fang HH et al. Advances and promises of layered halide hybrid perovskite semiconductors. *ACS Nano* **10**, 9776–9786 (2016).
27. Ramirez D, Suto Y, Rosero-Navarro NC, Miura A, Tadanaga K et al. Structural and electrochemical evaluation of three- and two-dimensional organohalide perovskites and their influence on the reversibility of lithium intercalation. *Inorg Chem* **57**, 4181–4188 (2018).
28. Smith MD, Connor BA, Karunadasa HI. Tuning the luminescence of layered halide perovskites. *Chem Rev* **119**, 3104–3139 (2019).
29. Li ZT, Cao K, Li JS, Tang Y, Ding XR et al. Review of blue perovskite light emitting diodes with optimization strategies for perovskite film and device structure. *Opto-Electron Adv* **4**, 200019 (2021).
30. Lai ML, Tay TYS, Sadhanala A, Dutton SE, Li GR et al. Tunable near-infrared luminescence in Tin halide perovskite devices. *J Phys Chem Lett* **7**, 2653–2658 (2016).
31. Wong AB, Lai ML, Eaton SW, Yu Y, Lin E et al. Growth and anion exchange conversion of $\text{CH}_3\text{NH}_3\text{PbX}_3$ nanorod arrays for light-emitting diodes. *Nano Lett* **15**, 5519–5524 (2015).
32. Leyden MR, Meng LQ, Jiang Y, Ono LK, Qiu LB et al. Methylammonium lead bromide perovskite light-emitting diodes by chemical vapor deposition. *J Phys Chem Lett* **8**, 3193–3198 (2017).
33. Yuan S, Wang ZK, Zhuo MP, Tian QS, Jin Y et al. Self-assembled high quality CsPbBr_3 quantum dot films toward highly efficient light-emitting diodes. *ACS Nano* **12**, 9541–9548 (2018).
34. Cho H, Kim YH, Wolf C, Lee HD, Lee TW. Improving the stability of metal halide perovskite materials and light-emitting diodes. *Adv Mater* **30**, 1704587 (2018).
35. Raghavan CM, Chen TP, Li SS, Chen WL, Lo CY et al. Low-threshold lasing from 2D homologous organic-inorganic hybrid ruddlesden-popper perovskite single crystals. *Nano Lett* **18**, 3221–3228 (2018).
36. Wei Q, Li XJ, Liang C, Zhang ZP, Guo J et al. Recent progress in metal halide perovskite micro- and nanolasers. *Adv Opt Mater* **7**, 1900080 (2019).
37. Wang KY, Xing GC, Song QH, Xiao SM. Micro- and nano-structured lead halide perovskites: from materials to integrations and devices. *Adv Mater* **33**, 2000306 (2021).
38. Qin CJ, Sandanayaka ASD, Zhao CY, Matsushima T, Zhang DZ et al. Stable room-temperature continuous-wave lasing in quasi-2D perovskite films. *Nature* **585**, 53–57 (2020).
39. Xing GC, Mathews N, Lim SS, Yantara N, Liu XF et al. Low-temperature solution-processed wavelength-tunable perovskites for lasing. *Nat Mater* **13**, 476–480 (2014).
40. El-Ballouli AO, Bakr OM, Mohammed OF. Structurally tunable two-dimensional layered perovskites: from confinement and enhanced charge transport to prolonged hot carrier cooling dynamics. *J Phys Chem Lett* **11**, 5705–5718 (2020).
41. Quan LN, Yuan MJ, Comin R, Voznyy O, Beauregard EM et al. Ligand-stabilized reduced-dimensionality perovskites. *J Am Chem Soc* **138**, 2649–2655 (2016).
42. Jung MH. Photovoltaic effect of 2D homologous perovskites. *Electrochim Acta* **240**, 98–107 (2017).
43. Tsai H, Nie WY, Blancon JC, Stoumpos CC, Asadpour R et al. High-efficiency two-dimensional ruddlesden-popper perovskite solar cells. *Nature* **536**, 312–316 (2016).
44. Blancon JC, Tsai H, Nie W, Stoumpos CC, Pedesseau L et al. Extremely efficient internal exciton dissociation through edge states in layered 2D perovskites. *Science* **355**, 1288–1292 (2017).
45. Stoumpos CC, Soe CMM, Tsai H, Nie WY, Blancon JC et al. High members of the 2D ruddlesden-popper halide perovskites: synthesis, optical properties, and solar cells of $(\text{CH}_3(\text{CH}_2)_3\text{NH}_3)_2(\text{CH}_3\text{NH}_3)_4\text{Pb}_5\text{I}_{16}$. *Chem* **2**, 427–440 (2017).
46. Gan XY, Wang O, Liu KY, Du XJ, Guo LL et al. 2D homologous organic-inorganic hybrids as light-absorbers for planar and nanorod-based perovskite solar cells. *Sol Energy Mater Sol Cells* **162**, 93–102 (2017).
47. Wei Y, Audebert P, Galmiche L, Lauret JS, Deleporte E. Photostability of 2D organic-inorganic hybrid perovskites. *Materials* **7**, 4789–4802 (2014).
48. Wang NN, Cheng L, Ge R, Zhang ST, Miao YF et al. Perovskite light-emitting diodes based on solution-processed self-organized multiple quantum wells. *Nat Photonics* **10**, 699–704 (2016).
49. Yuan MJ, Quan LN, Comin R, Walters G, Sabatini R et al. Perovskite energy funnels for efficient light-emitting diodes. *Nat Nanotechnol* **11**, 872–877 (2016).
50. Li D, Liao PZ, Shai XX, Huang WC, Liu SS et al. Recent progress on stability issues of organic-inorganic hybrid lead perovskite-based solar cells. *RSC Adv* **6**, 89356–89366 (2016).

51. Wang ZP, Lin QQ, Chmiel FP, Sakai N, Herz LM et al. Efficient ambient-air-stable solar cells with 2D–3D heterostructured butylammonium-caesium-formamidinium lead halide perovskites. *Nat Energy* 2, 17135 (2017).
52. Long MS, Wang P, Fang HH, Hu WD. Progress, challenges, and opportunities for 2D material based photodetectors. *Adv Funct Mater* 29, 1803807 (2019).
53. Huo NJ, Konstantatos G. Recent progress and future prospects of 2D-based photodetectors. *Adv Mater* 30, 1801164 (2018).
54. Wang FK, Zhang Y, Gao Y, Luo P, Su JW et al. 2D metal chalcogenides for IR photodetection. *Small* 15, 1901347 (2019).
55. Xie C, Mak C, Tao XM, Yan F. Photodetectors based on two-dimensional layered materials beyond graphene. *Adv Funct Mater* 27, 1603886 (2017).
56. Mitta SB, Choi MS, Nipane A, Ali F, Kim C et al. Electrical characterization of 2D materials-based field-effect transistors. *2D Mater* 8, 012002 (2021).
57. Shang JZ, Cong CX, Wu LS, Huang W, Yu T. Light sources and photodetectors enabled by 2D semiconductors. *Small Methods* 2, 1800019 (2018).
58. Lien DH, Amani M, Desai SB, Ahn GH, Han K et al. Large-area and bright pulsed electroluminescence in monolayer semiconductors. *Nat Commun* 9, 1229 (2018).
59. Ross JS, Klement P, Jones AM, Ghimire NJ, Yan JQ et al. Electrically tunable excitonic light-emitting diodes based on monolayer WSe₂ p–n junctions. *Nat Nanotechnol* 9, 268–272 (2014).
60. Withers F, Del Pozo-Zamudio O, Mishchenko A, Rooney AP, Gholinia A et al. Light-emitting diodes by band-structure engineering in van der Waals heterostructures. *Nat Mater* 14, 301–306 (2015).
61. Mak KF, Shan J. Photonics and optoelectronics of 2D semiconductor transition metal dichalcogenides. *Nat Photonics* 10, 216–226 (2016).
62. Wu SF, Buckley S, Schaibley JR, Feng LF, Yan JQ et al. Monolayer semiconductor nanocavity lasers with ultralow thresholds. *Nature* 520, 69–72 (2015).
63. Ye Y, Wong ZJ, Lu XF, Ni XJ, Zhu HY et al. Monolayer excitonic laser. *Nat Photonics* 9, 733–737 (2015).
64. Liu ML, Wu HB, Liu XM, Wang YR, Lei M et al. Optical properties and applications of SnS₂ SAs with different thickness. *Opto-Electron Adv* 4, 200029 (2021).
65. Li YZ, Zhang JX, Huang DD, Sun H, Fan F et al. Room-temperature continuous-wave lasing from monolayer molybdenum ditelluride integrated with a silicon nanobeam cavity. *Nat Nanotechnol* 12, 987–992 (2017).
66. Liu YD, Fang HL, Rasmitha A, Zhou Y, Li JT et al. Room temperature nanocavity laser with interlayer excitons in 2D heterostructures. *Sci Adv* 5, eaav4506 (2019).
67. Shang JZ, Cong CX, Wang ZL, Peimyoo N, Wu LS et al. Room-temperature 2D semiconductor activated vertical-cavity surface-emitting lasers. *Nat Commun* 8, 543 (2017).
68. Bernardi M, Palummo M, Grossman JC. Extraordinary sunlight absorption and one nanometer thick photovoltaics using two-dimensional monolayer materials. *Nano Lett* 13, 3664–3670 (2013).
69. Sumesh CK. Towards efficient photon management in nanostructured solar cells: role of 2D layered transition metal dichalcogenide semiconductors. *Sol Energy Mater Sol Cells* 192, 16–23 (2019).
70. Lin YB, Adilbekova B, Firdaus Y, Yengel E, Faber H et al. 17% efficient organic solar cells based on liquid exfoliated WS₂ as a replacement for PEDOT: PSS. *Adv Mater* 31, 1902965 (2019).
71. Rivera P, Yu HY, Seyler KL, Wilson NP, Yao W et al. Interlayer valley excitons in heterobilayers of transition metal dichalcogenides. *Nat Nanotechnol* 13, 1004–1015 (2018).
72. Flöry N, Ma P, Salamin Y, Emboras A, Taniguchi T et al. Waveguide-integrated van der Waals heterostructure photodetector at telecom wavelengths with high speed and high responsivity. *Nat Nanotechnol* 15, 118–124 (2020).
73. Zhang L, Wu FC, Hou SC, Zhang Z, Chou YH et al. Van der Waals heterostructure polaritons with moiré-induced nonlinearity. *Nature* 591, 61–65 (2021).
74. Jiang CY, Xu WG, Rasmitha A, Huang ZM, Li K et al. Microsecond dark-exciton valley polarization memory in two-dimensional heterostructures. *Nat Commun* 9, 753 (2018).
75. Shimazaki Y, Schwartz I, Watanabe K, Taniguchi T, Kroner M et al. Strongly correlated electrons and hybrid excitons in a moiré heterostructure. *Nature* 580, 472–477 (2020).
76. Tran K, Moody G, Wu FC, Lu XB, Choi J et al. Evidence for moiré excitons in van der Waals heterostructures. *Nature* 567, 71–75 (2019).
77. Jin CH, Regan EC, Yan AM, Utama MIB, Wang DQ et al. Observation of moiré excitons in WSe₂/WS₂ heterostructure superlattices. *Nature* 567, 76–80 (2019).
78. Brotons-Gisbert M, Baek H, Molina-Sánchez A, Campbell A, Scerri E et al. Spin–layer locking of interlayer excitons trapped in moiré potentials. *Nat Mater* 19, 630–636 (2020).
79. Alexeev EM, Ruiz-Tijerina DA, Danovich M, Hamer MJ, Terry DJ et al. Resonantly hybridized excitons in moiré superlattices in van der Waals heterostructures. *Nature* 567, 81–86 (2019).
80. Li WJ, Lu X, Dubey S, Devenica L, Srivastava A. Dipolar interactions between localized interlayer excitons in van der Waals heterostructures. *Nat Mater* 19, 624–629 (2020).
81. Chhowalla M, Shin HS, Eda G, Li LJ, Loh KP et al. The chemistry of two-dimensional layered transition metal dichalcogenide nanosheets. *Nat Chem* 5, 263–275 (2013).
82. Eda G, Maier SA. Two-dimensional crystals: managing light for optoelectronics. *ACS Nano* 7, 5660–5665 (2013).
83. Singh R, Singh P, Balasubramanian G. Effect of heterostructure engineering on electronic structure and transport properties of two-dimensional halide perovskites. *Comput Mater Sci* 200, 110823 (2021).
84. Ricciardulli AG, Yang S, Smet JH, Saliba M. Emerging perovskite monolayers. *Nat Mater* 20, 1325–1336 (2021).
85. Chen YY, Liu ZY, Li JZ, Cheng X, Ma JQ et al. Robust interlayer coupling in two-dimensional perovskite/monolayer transition metal dichalcogenide heterostructures. *ACS Nano* 14, 10258–10264 (2020).
86. Nayak PK, Horbatenko Y, Ahn S, Kim G, Lee JU et al. Probing evolution of twist-angle-dependent interlayer excitons in MoSe₂/WSe₂ van der Waals Heterostructures. *ACS Nano* 11, 4041–4050 (2017).
87. Lo SS, Mirkovic T, Chuang CH, Burda C, Scholes GD. Emergent properties resulting from type-II band alignment in semiconductor nanoheterostructures. *Adv Mater* 23, 180–197 (2011).
88. Liu HY, Tan YS, Cao MH, Hu HC, Wu LZ et al. Fabricating CsPbX₃-based type I and type II heterostructures by tuning the

- halide composition of janus CsPbX₃/ZrO₂ nanocrystals. *ACS Nano* **13**, 5366–5374 (2019).
89. Fang QY, Shang QY, Zhao LY, Wang R, Zhang ZP et al. Ultrafast charge transfer in perovskite nanowire/2D transition metal dichalcogenide heterostructures. *J Phys Chem Lett* **9**, 1655–1662 (2018).
90. Wang Y, Fullon R, Acerce M, Petoukhoff CE, Yang J et al. Solution-processed MoS₂/organolead trihalide perovskite photodetectors. *Adv Mater* **29**, 1603995 (2017).
91. Wang LM, Zou XM, Lin J, Jiang JY, Liu Y et al. Perovskite/black phosphorus/MoS₂ photogate reversed photodiodes with ultrahigh light on/off ratio and fast response. *ACS Nano* **13**, 4804–4813 (2019).
92. Wu HL, Kang Z, Zhang ZH, Zhang Z, Si HN et al. Interfacial charge behavior modulation in perovskite quantum dot-monolayer MoS₂ 0D-2D mixed-dimensional van der waals heterostructures. *Adv Funct Mater* **28**, 1802015 (2018).
93. Yang A, Blancon JC, Jiang W, Zhang H, Wong J et al. Giant enhancement of photoluminescence emission in WS₂-two-dimensional perovskite heterostructures. *Nano Lett* **19**, 4852–4860 (2019).
94. Wang XD, Huang YH, Liao JF, Jiang Y, Zhou L et al. In situ construction of a Cs₂SnI₆ perovskite nanocrystal/SnS₂ nanosheet heterojunction with boosted interfacial charge transfer. *J Am Chem Soc* **141**, 13434–13441 (2019).
95. Zhang Q, Linardy E, Wang XY, Eda G. Excitonic energy transfer in heterostructures of quasi-2D perovskite and monolayer WS₂. *ACS Nano* **14**, 11482–11489 (2020).
96. Wang HZ, Ma JQ, Li DH. Two-dimensional hybrid perovskite-based van der waals heterostructures. *J Phys Chem Lett* **12**, 8178–8187 (2021).
97. Shi EZ, Gao Y, Finkenauer BP, Akriti, Coffey AH et al. Two-dimensional halide perovskite nanomaterials and heterostructures. *Chem Soc Rev* **47**, 6046–6072 (2018).
98. Xie C, Liu CK, Loi HL, Yan F. Perovskite - based phototransistors and hybrid photodetectors. *Adv Funct Mater* **30**, 1903907 (2020).
99. Omprakash P, Viswesh P, Devadas BP. Review—a review of 2D perovskites and carbon-based nanomaterials for applications in solar cells and photodetectors. *ECS J Solid State Sci Technol* **10**, 031009 (2021).
100. Ghosh J, Giri PK. Recent advances in perovskite/2D materials based hybrid photodetectors. *J Phys Mater* **4**, 032008 (2021).
101. Bellani S, Bartolotta A, Agresti A, Calogero G, Grancini G et al. Solution-processed two-dimensional materials for next-generation photovoltaics. *Chem Soc Rev* **50**, 11870–11965 (2021).
102. Rogdakis K, Karakostas N, Kymakis E. Up-scalable emerging energy conversion technologies enabled by 2D materials: from miniature power harvesters towards grid-connected energy systems. *Energy Environ Sci* **14**, 3352–3392 (2021).
103. Pant A, Mutlu Z, Wickramaratne D, Cai H, Lake RK et al. Fundamentals of lateral and vertical heterojunctions of atomically thin materials. *Nanoscale* **8**, 3870–3887 (2016).
104. Unger EL, Kegelmann L, Suchan K, Sörell D, Korte L et al. Roadmap and roadblocks for the band gap tunability of metal halide perovskites. *J Mater Chem A* **5**, 11401–11409 (2017).
105. Jiang Y, Chen SL, Zheng WH, Zheng BY, Pan AL. Interlayer exciton formation, relaxation, and transport in TMD van der Waals heterostructures. *Light Sci Appl* **10**, 72 (2021).
106. Tartakovskii A. Excitons in 2D heterostructures. *Nat Rev Phys* **2**, 8–9 (2020).
107. Mueller T, Malic E. Exciton physics and device application of two-dimensional transition metal dichalcogenide semiconductors. *npj 2D Mater Appl* **2**, 29 (2018).
108. Rasmussen FA, Thygesen KS. Computational 2D materials database: electronic structure of transition-metal dichalcogenides and oxides. *J Phys Chem C* **119**, 13169–13183 (2015).
109. Chaves A, Azadani JG, Alsalmán H, Da Costa DR, Frisenda R et al. Bandgap engineering of two-dimensional semiconductor materials. *npj 2D Mater Appl* **4**, 29 (2020).
110. Hong XP, Kim J, Shi SF, Zhang Y, Jin CH et al. Ultrafast charge transfer in atomically thin MoS₂/WS₂ heterostructures. *Nat Nanotechnol* **9**, 682–686 (2014).
111. Ceballos F, Bellus MZ, Chiu HY, Zhao H. Ultrafast charge separation and indirect exciton formation in a MoS₂-MoSe₂ van der waals heterostructure. *ACS Nano* **8**, 12717–12724 (2014).
112. Jin CH, Ma EY, Karni O, Regan EC, Wang F et al. Ultrafast dynamics in van der waals heterostructures. *Nat Nanotechnol* **13**, 994–1003 (2018).
113. Mak KF, Shan J. Opportunities and challenges of interlayer exciton control and manipulation. *Nat Nanotechnol* **13**, 974–976 (2018).
114. Excitation that lasts. *Nat Nanotechnol* **13**, 973 (2018).
115. Liu Y, Weiss NO, Duan XD, Cheng HC, Huang Y et al. Van der waals heterostructures and devices. *Nat Rev Mater* **1**, 16042 (2016).
116. Liu YD, Elbanna A, Gao WB, Pan JS, Shen ZX et al. Interlayer excitons in transition metal dichalcogenide semiconductors for 2D optoelectronics. *Adv Mater* **34**, 2107138 (2022).
117. Lukman S, Ding L, Xu L, Tao Y, Riis-Jensen AC et al. High oscillator strength interlayer excitons in two-dimensional heterostructures for mid-infrared photodetection. *Nat Nanotechnol* **15**, 675–682 (2020).
118. Karni O, Barré E, Lau SC, Gillen R, Ma EY et al. Infrared interlayer exciton emission in MoS₂/WSe₂ heterostructures. *Phys Rev Lett* **123**, 247402 (2019).
119. Wang ZF, Rhodes DA, Watanabe K, Taniguchi T, Hone JC et al. Evidence of high-temperature exciton condensation in two-dimensional atomic double layers. *Nature* **574**, 76–80 (2019).
120. Kim J, Jin CH, Cai H, Zhao T, Lee P et al. Observation of ultralong valley lifetime in WSe₂/MoS₂ heterostructures. *Sci Adv* **3**, e1700518 (2017).
121. Jin CH, Tao Z, Li TX, Xu Y, Tang TH et al. Stripe phases in WSe₂/WS₂ moiré superlattices. *Nat Mater* **20**, 940–944 (2021).
122. Regan EC, Wang DQ, Jin CH, Utama MIB, Gao BN et al. Mott and generalized wigner crystal states in WSe₂/WS₂ moiré superlattices. *Nature* **579**, 359–363 (2020).
123. Abouelkomsan A, Liu Z, Bergholtz EJ. Particle-hole duality, emergent fermi liquids, and fractional chern insulators in moiré flatbands. *Phys Rev Lett* **124**, 106803 (2020).
124. Xu Y, Liu S, Rhodes DA, Watanabe K, Taniguchi T et al. Correlated insulating states at fractional fillings of moiré superlattices. *Nature* **587**, 214–218 (2020).
125. Tartakovskii A. Moiré or not. *Nat Mater* **19**, 581–582 (2020).
126. Khelifa R, Back P, Flöry N, Nashashibi S, Malchow K et al. Coupling interlayer excitons to whispering gallery modes in van der waals heterostructures. *Nano Lett* **20**, 6155–6161 (2020).
127. Paik EY, Zhang L, Burg GW, Gogna R, Tutuc E et al. Interlayer exciton laser of extended spatial coherence in atomically thin heterostructures. *Nature* **576**, 80–84 (2019).

128. Xue H, Wang YD, Dai YY, Kim W, Jussila H et al. A MoSe₂/WSe₂ heterojunction-based photodetector at telecommunication wavelengths. *Adv Funct Mater* **28**, 1804388 (2018).
129. Wang GC, Li L, Fan WH, Wang RY, Zhou SS et al. Interlayer coupling induced infrared response in WS₂/MoS₂ heterostructures enhanced by surface plasmon resonance. *Adv Funct Mater* **28**, 1800339 (2018).
130. Jo SH, Lee HW, Shim J, Heo K, Kim M et al. Highly efficient infrared photodetection in a gate-controllable van der waals heterojunction with staggered bandgap alignment. *Adv Sci* **5**, 1700423 (2018).
131. Ross JS, Rivera P, Schaibley J, Lee-Wong E, Yu HY et al. Interlayer exciton optoelectronics in a 2D heterostructure p–n junction. *Nano Lett* **17**, 638–643 (2017).
132. Zhang KN, Zhang TN, Cheng GH, Li TX, Wang SX et al. Interlayer transition and infrared photodetection in atomically thin type-II MoTe₂/MoS₂ van der waals heterostructures. *ACS Nano* **10**, 3852–3858 (2016).
133. Li ZD, Lu XB, Leon DFC, Lyu ZY, Xie HC et al. Interlayer exciton transport in MoSe₂/WSe₂ heterostructures. *ACS Nano* **15**, 1539–1547 (2021).
134. Yuan L, Zheng BY, Kunstmann J, Brumme T, Kuc AB et al. Twist-angle-dependent interlayer exciton diffusion in WS₂-WSe₂ heterobilayers. *Nat Mater* **19**, 617–623 (2020).
135. Liu YD, Dini K, Tan QH, Liew T, Novoselov KS et al. Electrically controllable router of interlayer excitons. *Sci Adv* **6**, eaba1830 (2020).
136. Unuchek D, Ciarrocchi A, Avsar A, Sun Z, Watanabe K et al. Valley-polarized exciton currents in a van der Waals heterostructure. *Nat Nanotechnol* **14**, 1104–1109 (2019).
137. Jauregui LA, Joe AY, Pistunova K, Wild DS, High AA et al. Electrical control of interlayer exciton dynamics in atomically thin heterostructures. *Science* **366**, 870–875 (2019).
138. Ciarrocchi A, Unuchek D, Avsar A, Watanabe K, Taniguchi T et al. Polarization switching and electrical control of interlayer excitons in two-dimensional van der Waals heterostructures. *Nat Photonics* **13**, 131–136 (2019).
139. Unuchek D, Ciarrocchi A, Avsar A, Watanabe K, Taniguchi T et al. Room-temperature electrical control of exciton flux in a van der Waals heterostructure. *Nature* **560**, 340–344 (2018).
140. Jiang CY, Rasmita A, Ma H, Tan QH, Huang ZM et al. Room-temperature bipolar valleytronic transistor in MoS₂/WSe₂ heterostructures. [arXiv:2102.03756](https://arxiv.org/abs/2102.03756).
141. Green MA, Dunlop ED, Hohl-Ebinger J, Yoshita M, Kopidakis N et al. Solar cell efficiency tables (Version 58). *Prog Photovolt Res Appl* **29**, 657–667 (2021).
142. Saliba M, Correa-Baena JP, Grätzel M, Hagfeldt A, Abate A. Perovskite solar cells: from the atomic level to film quality and device performance. *Angew Chem Int Ed* **57**, 2554–2569 (2018).
143. Schileo G, Grancini G. Halide perovskites: current issues and new strategies to push material and device stability. *J Phys Energy* **2**, 021005 (2020).
144. Lekina Y, Shen ZX. Excitonic states and structural stability in two-dimensional hybrid organic-inorganic perovskites. *J Sci Adv Mater Dev* **4**, 189–200 (2019).
145. Ahmad S, Fu P, Yu SW, Yang Q, Liu X et al. Dion-jacobson phase 2D layered perovskites for solar cells with ultrahigh stability. *Joule* **3**, 794–806 (2019).
146. Cohen BE, Wierzbowska M, Etgar L. High efficiency and high open circuit voltage in quasi 2D perovskite based solar cells. *Adv Funct Mater* **27**, 1604733 (2017).
147. Dou LT, Wong AB, Yu Y, Lai ML, Kornienko N et al. Atomically thin two-dimensional organic-inorganic hybrid perovskites. *Science* **349**, 1518–1521 (2015).
148. Niu W, Eiden A, Prakash GV, Baumberg JJ. Exfoliation of self-assembled 2D organic-inorganic perovskite semiconductors. *Appl Phys Lett* **104**, 171111 (2014).
149. Dhanabalan B, Castelli A, Palei M, Spirito D, Manna L et al. Simple fabrication of layered halide perovskite platelets and enhanced photoluminescence from mechanically exfoliated flakes. *Nanoscale* **11**, 8334–8342 (2019).
150. Fu YP, Zheng WH, Wang XX, Hautzinger MP, Pan DX et al. Multicolor heterostructures of two-dimensional layered halide perovskites that show interlayer energy transfer. *J Am Chem Soc* **140**, 15675–15683 (2018).
151. Shi EZ, Yuan B, Shiring SB, Gao Y, Akriti et al. Two-dimensional halide perovskite lateral epitaxial heterostructures. *Nature* **580**, 614–620 (2020).
152. Akriti, Shi EZ, Shiring SB, Yang JQ, Atencio-Martinez CL et al. Layer-by-layer anionic diffusion in two-dimensional halide perovskite vertical heterostructures. *Nat Nanotechnol* **16**, 584–591 (2021).
153. Kuo MY, Spitha N, Hautzinger MP, Hsieh PL, Li J et al. Distinct carrier transport properties across horizontally vs vertically oriented heterostructures of 2D/3D perovskites. *J Am Chem Soc* **143**, 4969–4978 (2021).
154. Zhang XY, Liu XT, Li LN, Ji CM, Yao YP et al. Great amplification of circular polarization sensitivity via heterostructure engineering of a chiral two-dimensional hybrid perovskite crystal with a three-dimensional MAPbI₃ crystal. *ACS Cent Sci* **7**, 1261–1268 (2021).
155. Karpińska M, Liang MP, Kempt R, Finzel K, Kamminga M et al. Nonradiative energy transfer and selective charge transfer in a WS₂/(PEA)₂PbI₄ heterostructure. *ACS Appl Mater Interfaces* **13**, 33677–33684 (2021).
156. Wang QX, Zhang Q, Luo X, Wang JY, Zhu R et al. Optoelectronic properties of a van der waals WS₂ monolayer/2D perovskite vertical heterostructure. *ACS Appl Mater Interfaces* **12**, 45235–45242 (2020).
157. Yan ZZ, Jiang ZH, Lu JP, Ni ZH. Interfacial charge transfer in WS₂ monolayer/CsPbBr₃ microplate heterostructure. *Front Phys* **13**, 138115 (2018).
158. Wang HL, Wang XD, Chen Y, Zhang SK, Jiang W et al. Extremely low dark current MoS₂ photodetector via 2D halide perovskite as the electron reservoir. *Adv Opt Mater* **8**, 1901402 (2020).
159. Ghosh J, Mawlong LPL, Manasa GB, Pattison AJ, Theis W et al. Solid-state synthesis of stable and color tunable cesium lead halide perovskite nanocrystals and the mechanism of high-performance photodetection in a monolayer MoS₂/CsPbBr₃ vertical heterojunction. *J Mater Chem C* **8**, 8917–8934 (2020).
160. Hassan MS, Basera P, Bera S, Mittal M, Ray SK et al. Enhanced photocurrent owing to shuttling of charge carriers across 4-aminothiophenol-functionalized MoSe₂-CsPbBr₃ nanohybrids. *ACS Appl Mater Interfaces* **12**, 7317–7325 (2020).
161. Erkiliç U, Solís-Fernández P, Ji HG, Shinokita K, Lin YC et al. Vapor phase selective growth of two-dimensional perovskite/WS₂ heterostructures for optoelectronic applica-

- tions. *ACS Appl Mater Interfaces* **11**, 40503–40511 (2019).
162. Chen YY, Ma JQ, Liu ZY, Li JZ, Duan XF et al. Manipulation of valley pseudospin by selective spin injection in chiral two-dimensional perovskite/monolayer transition metal dichalcogenide heterostructures. *ACS Nano* **14**, 15154–15160 (2020).
163. Ma C, Shi YM, Hu WJ, Chiu MH, Liu ZX et al. Heterostructured $\text{WS}_2/\text{CH}_3\text{NH}_3\text{PbI}_3$ photoconductors with suppressed dark current and enhanced photodetectivity. *Adv Mater* **28**, 3683–3689 (2016).
164. Song XF, Liu XH, Yu DJ, Huo CX, Ji JP et al. Boosting two-dimensional $\text{MoS}_2/\text{CsPbBr}_3$ photodetectors via enhanced light absorbance and interfacial carrier separation. *ACS Appl Mater Interfaces* **10**, 2801–2809 (2018).
165. Yang TF, Wang X, Zheng BY, Qi ZY, Ma C et al. Ultrahigh-performance optoelectronics demonstrated in ultrathin perovskite-based vertical semiconductor heterostructures. *ACS Nano* **13**, 7996–8003 (2019).
166. Karpińska M, Jasiński J, Kempt R, Ziegler JD, Sansom H et al. Interlayer excitons in $\text{MoSe}_2/2\text{D}$ perovskite hybrid heterostructures – the interplay between charge and energy transfer. *Nanoscale* **14**, 8085–8095 (2022).
167. Wang JT, Li JH, Zhou YC, Yu CZ, Hua YH et al. Tuning an electrode work function using organometallic complexes in inverted perovskite solar cells. *J Am Chem Soc* **143**, 7759–7768 (2021).
168. Lee PH, Wu TT, Tian KY, Li CF, Hou CH et al. Work-function-tunable electron transport layer of molecule-capped metal oxide for a high-efficiency and stable p–i–n perovskite solar cell. *ACS Appl Mater Interfaces* **12**, 45936–45949 (2020).
169. Liu XC, Choi MS, Hwang E, Yoo WJ, Sun J. Fermi level pinning dependent 2D semiconductor devices: challenges and prospects. *Adv Mater* **34**, 2108425 (2022).
170. Yim C, Passi V, Lemme MC, Duesberg GS, Coileáin CÓ et al. Electrical devices from top-down structured platinum diselenide films. *npj 2D Mater Appl* **2**, 5 (2018).
171. Afzal AM, Iqbal MZ, Dastgeer G, Ahmad AU, Park B. Highly sensitive, ultrafast, and broadband photo-detecting field-effect transistor with transition-metal dichalcogenide van der waals heterostructures of MoTe_2 and PdSe_2 . *Adv Sci* **8**, 2003713 (2021).
172. Schulman DS, Arnold AJ, Das S. Contact engineering for 2D materials and devices. *Chem Soc Rev* **47**, 3037–3058 (2018).
173. Alzaid M. Recent progress in the role of two-dimensional materials as an efficient charge transport layer in perovskite solar cells. *Int J Energy Res* **45**, 12598–12613 (2021).
174. Mahmood K, Khalid A, Ahmad SW, Qutab HG, Hameed M et al. Electro spray deposited MoS_2 nanosheets as an electron transporting material for high efficiency and stable perovskite solar cells. *Sol Energy* **203**, 32–36 (2020).
175. Jung DH, Oh YJ, Nam YS, Lee H. Effect of layer number on the properties of stable and flexible perovskite solar cells using two dimensional material. *J Alloys Compd* **850**, 156752 (2021).
176. Singh R, Giri A, Pal M, Thiyagarajan K, Kwak J et al. Perovskite solar cells with an MoS_2 electron transport layer. *J Mater Chem A* **7**, 7151–7158 (2019).
177. Tan CL, Cao XH, Wu XJ, He QY, Yang J et al. Recent advances in ultrathin two-dimensional nanomaterials. *Chem Rev* **117**, 6225–6331 (2017).
178. Guo HW, Hu Z, Liu ZB, Tian JG. Stacking of 2D materials. *Adv Funct Mater* **31**, 2007810 (2021).
179. Desai SB, Madhupathy SR, Amani M, Kiriya D, Hettick M et al. Gold-mediated exfoliation of ultralarge optoelectronically-perfect monolayers. *Adv Mater* **28**, 4053–4058 (2016).
180. Liu F, Wu WJ, Bai YS, Chae SH, Li QY et al. Disassembling 2D van der waals crystals into macroscopic monolayers and reassembling into artificial lattices. *Science* **367**, 903–906 (2020).
181. Zhang Y, Yao YY, Sendeku MG, Yin L, Zhan XY et al. Recent progress in CVD growth of 2D transition metal dichalcogenides and related heterostructures. *Adv Mater* **31**, 1901694 (2019).
182. Wang SX, Cui XH, Jian C, Cheng HW, Niu MM et al. Stacking - engineered heterostructures in transition metal dichalcogenides. *Adv Mater* **33**, 2005735 (2021).
183. Liu LX, Zhai TY. Wafer-scale vertical van der Waals heterostructures. *InfoMat* **3**, 3–21 (2021).
184. Zhou JD, Lin JH, Huang XW, Zhou Y, Chen Y et al. A library of atomically thin metal chalcogenides. *Nature* **556**, 355–359 (2018).
185. Lin HR, Zhou CK, Tian Y, Siegrist T, Ma BW. Low-dimensional organometal halide perovskites. *ACS Energy Lett* **3**, 54–62 (2018).
186. Jagielski J, Kumar S, Yu WY, Shih CJ. Layer-controlled two-dimensional perovskites: synthesis and optoelectronics. *J Mater Chem C* **5**, 5610–5627 (2017).
187. Shamsi J, Urban AS, Imran M, De Trizio L, Manna L. Metal halide perovskite nanocrystals: synthesis, post-synthesis modifications, and their optical properties. *Chem Rev* **119**, 3296–3348 (2019).
188. Ha ST, Liu XF, Zhang Q, Giovanni D, Sum TC et al. Synthesis of organic-inorganic lead halide perovskite nanoplatelets: towards high-performance perovskite solar cells and optoelectronic devices. *Adv Opt Mater* **2**, 838–844 (2014).
189. Kim HS, Im SH, Park NG. Organolead halide perovskite: new horizons in solar cell research. *J Phys Chem C* **118**, 5615–5625 (2014).
190. Protesescu L, Yakunin S, Bodnarchuk MI, Krieg F, Caputo R et al. Nanocrystals of cesium lead halide perovskites (CsPbX_3 , X = Cl, Br, and I): novel optoelectronic materials showing bright emission with wide color gamut. *Nano Lett* **15**, 3692–3696 (2015).
191. Schmidt LC, Pertegás A, González-Carrero S, Malinkiewicz O, Agouram S et al. Nontemplate synthesis of $\text{CH}_3\text{NH}_3\text{PbBr}_3$ perovskite nanoparticles. *J Am Chem Soc* **136**, 850–853 (2014).
192. Niu L, Liu XF, Cong CX, Wu CY, Wu D et al. Controlled synthesis of organic/inorganic van der waals solid for tunable light-matter interactions. *Adva Mater* **27**, 7800–7808 (2015).
193. Wang YP, Shi YF, Xin GQ, Lian J, Shi J. Two-dimensional van der waals epitaxy kinetics in a three-dimensional perovskite halide. *Cryst Growth Des* **15**, 4741–4749 (2015).
194. Wang GM, Li DH, Cheng HC, Li YJ, Chen CY et al. Wafer-scale growth of large arrays of perovskite microplate crystals for functional electronics and optoelectronics. *Sci Adv* **1**, e1500613 (2015).
195. Liu JY, Xue YZ, Wang ZY, Xu ZQ, Zheng CX et al. Two-dimensional $\text{CH}_3\text{NH}_3\text{PbI}_3$ perovskite: synthesis and optoelectronic application. *ACS Nano* **10**, 3536–3542 (2016).
196. Ávila J, Momblona C, Boix PP, Sessolo M, Bolink HJ. Vapor-deposited perovskites: the route to high-performance solar cell

- production. *Joule* **1**, 431–442 (2017).
197. Ono LK, Leyden MR, Wang SH, Qi YB. Organometal halide perovskite thin films and solar cells by vapor deposition. *J Mater Chem A* **4**, 6693–6713 (2016).
 198. Febriansyah B, Lekina Y, Kaur J, Hooper TJN, Harikesh PC et al. Formation of corrugated $n=1$ 2D tin iodide perovskites and their use as lead-free solar absorbers. *ACS Nano* **15**, 6395–6409 (2021).
 199. Ng YF, Febriansyah B, Jamaludin NF, Giovanni D, Yantara N et al. Design of 2D templating molecules for mixed-dimensional perovskite light-emitting diodes. *Chem Mater* **32**, 8097–8105 (2020).
 200. Lan CY, Zhou ZY, Wei RJ, Ho JC. Two-dimensional perovskite materials: from synthesis to energy-related applications. *Mater Today Energy* **11**, 61–82 (2019).
 201. Cheng ZY, Lin J. Layered organic–inorganic hybrid perovskites: structure, optical properties, film preparation, patterning and templating engineering. *CrystEngComm* **12**, 2646–2662 (2010).
 202. Febriansyah B, Lekina Y, Ghosh B, Harikesh PC, Koh TM et al. Molecular engineering of pure 2D lead-iodide perovskite solar absorbers displaying reduced band gaps and dielectric confinement. *ChemSusChem* **13**, 2693–2701 (2020).
 203. Stoumpos CC, Cao DH, Clark DJ, Young J, Rondinelli JM et al. Ruddlesden–popper hybrid lead iodide perovskite 2D homologous semiconductors. *Chem Mater* **28**, 2852–2867 (2016).
 204. Tian H, Zhao LF, Wang XF, Yeh YW, Yao N et al. Extremely low operating current resistive memory based on exfoliated 2D perovskite single crystals for neuromorphic computing. *ACS Nano* **11**, 12247–12256 (2017).
 205. Lédée F, Trippé-Allard G, Diab H, Audebert P, Garrot D et al. Fast growth of monocrystalline thin films of 2D layered hybrid perovskite. *CrystEngComm* **19**, 2598–2602 (2017).
 206. Chen ZH, Zhang Q, Zhu ML, Wang XY, Wang QX et al. Synthesis of two - dimensional perovskite by inverse temperature crystallization and studies of exciton states by two - photon excitation spectroscopy. *Adv Funct Mater* **30**, 2002661 (2020).
 207. Saikumar I, Ahmad S, Baumberg JJ, Prakash GV. Fabrication of excitonic luminescent inorganic–organic hybrid nano- and microcrystals. *Scr Mater* **67**, 834–837 (2012).
 208. Gerwien A, Schildhauer M, Thumser S, Mayer P, Dube H. Direct evidence for hula twist and single-bond rotation photo-products. *Nat Commun* **9**, 2510 (2018).
 209. Xiao X, Dai J, Fang YJ, Zhao JJ, Zheng XP et al. Suppressed ion migration along the in-plane direction in layered perovskites. *ACS Energy Lett* **3**, 684–688 (2018).
 210. Liu YC, Zhang YX, Yang Z, Ye HC, Feng JS et al. Multi-inch single-crystalline perovskite membrane for high-detectivity flexible photosensors. *Nat Commun* **9**, 5302 (2018).
 211. Yaffe O, Chernikov A, Norman ZM, Zhong Y, Velauthapillai A et al. Excitons in ultrathin organic-inorganic perovskite crystals. *Phys Rev B* **92**, 045414 (2015).
 212. Chen JN, Gan L, Zhuge FW, Li HQ, Song JZ et al. A ternary solvent method for large-sized two-dimensional perovskites. *Angew Chem Int Ed* **56**, 2390–2394 (2017).
 213. Hintermayr VA, Richter AF, Ehrat F, Döblinger M, Vanderlinden W et al. Tuning the optical properties of perovskite nanoplatelets through composition and thickness by ligand-assisted exfoliation. *Adv Mater* **28**, 9478–9485 (2016).
 214. Zhang Y, Zhang LY, Zhou CW. Review of chemical vapor deposition of graphene and related applications. *Acc Chem Res* **46**, 2329–2339 (2013).
 215. Lee YH, Zhang XQ, Zhang WJ, Chang MT, Lin CT et al. Synthesis of large-area MoS₂ atomic layers with chemical vapor deposition. *Adv Mater* **24**, 2320–2325 (2012).
 216. Lan CY, Zhou ZY, Zhou ZF, Li C, Shu L et al. Wafer-scale synthesis of monolayer WS₂ for high-performance flexible photodetectors by enhanced chemical vapor deposition. *Nano Res* **11**, 3371–3384 (2018).
 217. Sun JY, Lu C, Song YZ, Ji QQ, Song XJ et al. Recent progress in the tailored growth of two-dimensional hexagonal boron nitride via chemical vapour deposition. *Chem Soc Rev* **47**, 4242–4257 (2018).
 218. Chen ZZ, Wang YP, Sun X, Guo YW, Hu Y et al. Van der waals hybrid perovskite of high optical quality by chemical vapor deposition. *Adv Opt Mater* **5**, 1700373 (2017).
 219. Wang YG, Huang XW, Wu D, Zhuo RR, Wu EP et al. A room-temperature near-infrared photodetector based on a MoS₂/CdTe p–n heterojunction with a broadband response up to 1700 nm. *J Mater Chem C* **6**, 4861–4865 (2018).
 220. Zhang ZP, Wang SS, Liu XF, Chen YH, Su CL et al. Metal halide perovskite/2D material heterostructures: syntheses and applications. *Small Methods* **5**, 2000937 (2021).
 221. Lu JP, Carvalho A, Liu HW, Lim SX, Neto AHC et al. Hybrid bilayer WSe₂-CH₃NH₃PbI₃ organolead halide perovskite as a high-performance photodetector. *Angew Chem Int Ed* **55**, 11945–11949 (2016).
 222. Xia KL, Wu WQ, Zhu MJ, Shen XY, Yin Z et al. CVD growth of perovskite/graphene films for high-performance flexible image sensor. *Sci Bull* **65**, 343–349 (2020).
 223. Suk JW, Kitt A, Magnuson CW, Hao YF, Ahmed S et al. Transfer of CVD-grown monolayer graphene onto arbitrary substrates. *ACS Nano* **5**, 6916–6924 (2011).
 224. Jeong HJ, Kim HY, Jeong SY, Han JT, Baeg KJ et al. Improved transfer of chemical-vapor-deposited graphene through modification of intermolecular interactions and solubility of poly(methylmethacrylate) layers. *Carbon* **66**, 612–618 (2014).
 225. Van Ngoc H, Qian YT, Han SK, Kang DJ. PMMA-etching-free transfer of wafer-scale chemical vapor deposition two-dimensional atomic crystal by a water soluble polyvinyl alcohol polymer method. *Sci Rep* **6**, 33096 (2016).
 226. Bae S, Kim H, Lee Y, Xu XF, Park JS et al. Roll-to-roll production of 30-inch graphene films for transparent electrodes. *Nat Nanotechnol* **5**, 574–578 (2010).
 227. Barin GB, Song Y, De Fátima Gimenez I, Filho AGS, Barreto LS et al. Optimized graphene transfer: influence of polymethylmethacrylate (PMMA) layer concentration and baking time on graphene final performance. *Carbon* **84**, 82–90 (2015).
 228. Liang XL, Sperling BA, Calizo I, Cheng GJ, Hacker CA et al. Toward clean and crackless transfer of graphene. *ACS Nano* **5**, 9144–9153 (2011).
 229. Cheng HC, Wang GM, Li DH, He QY, Yin AX et al. Van der waals heterojunction devices based on organohalide perovskites and two-dimensional materials. *Nano Lett* **16**, 367–373 (2016).
 230. Huang X, Qi XY, Boey F, Zhang H. Graphene-based composites. *Chem Soc Rev* **41**, 666–686 (2012).
 231. Muduli S, Pandey P, Devatha G, Babar R, M T et al. Photoluminescence quenching in self-assembled CsPbBr₃ quantum

- dots on few-layer black phosphorus sheets. *Angew Chem Int Ed* **57**, 7682–7686 (2018).
232. Xu YF, Yang MZ, Chen BX, Wang XD, Chen HY et al. A CsPbBr₃ perovskite quantum dot/graphene oxide composite for photocatalytic CO₂ reduction. *J Am Chem Soc* **139**, 5660–5663 (2017).
233. Jung M, Ji SG, Kim G, Seok II S. Perovskite precursor solution chemistry: from fundamentals to photovoltaic applications. *Chem Soc Rev* **48**, 2011–2038 (2019).
234. Chao LF, Niu TT, Gao WY, Ran CX, Song L et al. Solvent engineering of the precursor solution toward Large - area production of perovskite solar cells. *Adv Mater* **33**, 2005410 (2021).
235. Febriansyah B, Koh TM, Rana PJS, Hooper TJN, Ang ZZ et al. Hybrid 2D [Pb(CH₃NH₂)₂]_n coordination polymer precursor for scalable perovskite deposition. *ACS Energy Lett* **5**, 2305–2312 (2020).
236. Yoo JJ, Seo G, Chua MR, Park TG, Lu YL et al. Efficient perovskite solar cells via improved carrier management. *Nature* **590**, 587–593 (2021).
237. Kim YH, Kim S, Kakekhani A, Park J, Park J et al. Comprehensive defect suppression in perovskite nanocrystals for high-efficiency light-emitting diodes. *Nat Photonics* **15**, 148–155 (2021).
238. John RA, Shah N, Vishwanath SK, Ng SE, Febriansyah B et al. Halide perovskite memristors as flexible and reconfigurable physical unclonable functions. *Nat Commun* **12**, 3681 (2021).
239. Kang DH, Pae SR, Shim J, Yoo G, Jeon J et al. An ultrahigh-performance photodetector based on a perovskite-transition-metal-dichalcogenide hybrid structure. *Adv Mater* **28**, 7799–7806 (2016).
240. Peng B, Yu GN, Zhao YW, Xu Q, Xing GC et al. Achieving ultrafast hole transfer at the monolayer MoS₂ and CH₃NH₃PbI₃ perovskite interface by defect engineering. *ACS Nano* **10**, 6383–6391 (2016).
241. Tang GQ, You P, Tai QD, Yang AN, Cao JP et al. Solution-phase epitaxial growth of perovskite films on 2D material flakes for high-performance solar cells. *Adv Mater* **31**, 1807689 (2019).
242. Fang C, Wang HZ, Shen ZX, Shen HZ, Wang S et al. High-performance photodetectors based on lead-free 2D ruddlesden–popper perovskite/MoS₂ heterostructures. *ACS Appl Mater Interfaces* **11**, 8419–8427 (2019).
243. Fu QD, Wang XL, Liu FC, Dong YX, Liu ZR et al. Ultrathin ruddlesden–popper perovskite heterojunction for sensitive photodetection. *Small* **15**, 1902890 (2019).
244. Ma JQ, Fang C, Chen C, Jin L, Wang JQ et al. Chiral 2D perovskites with a high degree of circularly polarized photoluminescence. *ACS Nano* **13**, 3659–3665 (2019).
245. Wang QX, Wee ATS. Upconversion photovoltaic effect of WS₂/2D perovskite heterostructures by two-photon absorption. *ACS Nano* **15**, 10437–10443 (2021).
246. Xiao JT, Zhang L, Zhou H, Shao ZY, Liu JX et al. Type-II interface band alignment in the vdW PbI₂–MoSe₂ heterostructure. *ACS Appl Mater Interfaces* **12**, 32099–32105 (2020).
247. Lee Y, Kwon J, Hwang E, Ra CH, Yoo WJ et al. High-performance perovskite-graphene hybrid photodetector. *Adv Mater* **27**, 41–46 (2015).
248. Wang YS, Zhang YP, Lu Y, Xu WD, Mu HR et al. Hybrid graphene-perovskite phototransistors with ultrahigh responsivity and gain. *Adv Opt Mater* **3**, 1389–1396 (2015).
249. Spina M, Lehmann M, Náfrádi B, Bernard L, Bonvin E et al. Microengineered CH₃NH₃PbI₃ nanowire/graphene phototransistor for low-intensity light detection at room temperature. *Small* **11**, 4824–4828 (2015).
250. Sun ZH, Aigouy L, Chen ZY. Plasmonic-enhanced perovskite–graphene hybrid photodetectors. *Nanoscale* **8**, 7377–7383 (2016).
251. Xie C, Yan F. Perovskite/poly(3-hexylthiophene)/graphene multiheterojunction phototransistors with ultrahigh gain in broadband wavelength region. *ACS Appl Mater Interfaces* **9**, 1569–1576 (2017).
252. Shao YC, Liu Y, Chen XL, Chen C, Sarpkaya I et al. Stable graphene-two-dimensional multiphase perovskite heterostructure phototransistors with high gain. *Nano Lett* **17**, 7330–7338 (2017).
253. Koppens FHL, Mueller T, Avouris P, Ferrari AC, Vitiello MS et al. Photodetectors based on graphene, other two-dimensional materials and hybrid systems. *Nat Nanotechnol* **9**, 780–793 (2014).
254. Mueller T, Xia FN, Avouris P. Graphene photodetectors for high-speed optical communications. *Nat Photonics* **4**, 297–301 (2010).
255. Wu HL, Si HN, Zhang ZH, Kang Z, Wu PW et al. All-inorganic perovskite quantum dot-monolayer MoS₂ mixed-dimensional van der waals heterostructure for ultrasensitive photodetector. *Adv Sci* **5**, 1801219 (2018).
256. Bai F, Qi JJ, Li F, Fang YY, Han WP et al. A High-performance self-powered photodetector based on monolayer MoS₂/perovskite heterostructures. *Adv Mater Interfaces* **5**, 1701275 (2018).
257. Peng ZY, Xu JL, Zhang JY, Gao X, Wang SD. Solution-processed high-performance hybrid photodetectors enhanced by perovskite/MoS₂ bulk heterojunction. *Adv Mater Interfaces* **5**, 1800505 (2018).
258. Zhang DD, Yu RM. Perovskite-WS₂ nanosheet composite optical absorbers on graphene as high-performance phototransistors. *Front Chem* **7**, 257 (2019).
259. Liu X, Li CL, Dai TF, Tao Z, Zhou WX et al. Infrared phototransistor induced by MoS₂ quantum dots encapsulated in lead iodide perovskite. *IEEE Electron Device Lett* **40**, 746–749 (2019).
260. Yang D, Cao MH, Zhong QX, Li PL, Zhang XH et al. All-inorganic cesium lead halide perovskite nanocrystals: synthesis, surface engineering and applications. *J Mater Chem C* **7**, 757–789 (2019).
261. Xiang WC, Tress W. Review on recent progress of all - inorganic metal halide perovskites and solar cells. *Adv Mater* **31**, 1902851 (2019).
262. Yettapu GR, Talukdar D, Sarkar S, Swarnkar A, Nag A et al. Terahertz conductivity within colloidal CsPbBr₃ perovskite nanocrystals: remarkably high carrier mobilities and large diffusion lengths. *Nano Lett* **16**, 4838–4848 (2016).
263. Guo LJ, Gu YS, Yang Z, Tian S, San X et al. CsPbBr₃ QDs modified vertically layered MoS₂/Si heterojunction for fast UV–vis–NIR spectrum flexible photodetectors. *Adv Mater Interfaces* **8**, 2002231 (2021).
264. Xu Q, Yang Z, Peng DF, Xi JG, Lin P et al. WS₂/CsPbBr₃ van der waals heterostructure planar photodetectors with ultrahigh on/off ratio and piezo-phototronic effect-induced strain-gated characteristics. *Nano Energy* **65**, 104001 (2019).

265. Wang ZL. Piezopotential gated nanowire devices: piezotronics and piezo-phototronics. *Nano Today* **5**, 540–552 (2010).
266. Yang Q, Guo X, Wang WH, Zhang Y, Xu S et al. Enhancing sensitivity of a single ZnO micro-/nanowire photodetector by piezo-phototronic effect. *ACS Nano* **4**, 6285–6291 (2010).
267. Hu YF, Chang YL, Fei P, Snyder RL, Wang ZL. Designing the electric transport characteristics of ZnO micro/nanowire devices by coupling piezoelectric and photoexcitation effects. *ACS Nano* **4**, 1234–1240 (2010).
268. Noh T, Shin HS, Seo C, Kim JY, Youn J et al. Significant enhancement of photoresponsive characteristics and mobility of MoS₂-based transistors through hybridization with perovskite CsPbBr₃ quantum dots. *Nano Res* **12**, 405–412 (2019).
269. Lin RC, Li XB, Zheng W, Huang F. Balanced photodetection in mixed-dimensional phototransistors consisting of CsPbBr₃ quantum dots and few-layer MoS₂. *ACS Appl Nano Mater* **2**, 2599–2605 (2019).
270. Yu XC, Yu P, Wu D, Singh B, Zeng QS et al. Atomically thin noble metal dichalcogenide: a broadband mid-infrared semiconductor. *Nat Commun* **9**, 1545 (2018).
271. Oyedele AD, Yang SZ, Liang LB, Poretzky AA, Wang K et al. PdSe₂: pentagonal two-dimensional layers with high air stability for electronics. *J Am Chem Soc* **139**, 14090–14097 (2017).
272. Wu D, Wang YG, Zeng LH, Jia C, Wu EP et al. Design of 2D layered PtSe₂ heterojunction for the high-performance, room-temperature, broadband, infrared photodetector. *ACS Photonics* **5**, 3820–3827 (2018).
273. Long MS, Wang Y, Wang P, Zhou XH, Xia H et al. Palladium diselenide long-wavelength infrared photodetector with high sensitivity and stability. *ACS Nano* **13**, 2511–2519 (2019).
274. Zeng LH, Lin SH, Lou ZH, Yuan HY, Long H et al. Ultrafast and sensitive photodetector based on a PtSe₂/silicon nanowire array heterojunction with a multiband spectral response from 200 to 1550 nm. *NPG Asia Mater* **10**, 352–362 (2018).
275. Zhao YD, Qiao JS, Yu ZH, Yu P, Xu K et al. High-electron-mobility and air-stable 2D layered PtSe₂ FETs. *Adv Mater* **29**, 1604230 (2017).
276. Wu D, Guo JW, Du J, Xia CX, Zeng LH et al. Highly polarization-sensitive, broadband, self-powered photodetector based on graphene/PdSe₂/germanium heterojunction. *ACS Nano* **13**, 9907–9917 (2019).
277. Walmsley TS, Andrews K, Wang TJ, Haglund A, Rijal U et al. Near-infrared optical transitions in PdSe₂ phototransistors. *Nanoscale* **11**, 14410–14416 (2019).
278. Zhang ZX, Zeng LH, Tong XW, Gao Y, Xie C et al. Ultrafast, self-driven, and air-stable photodetectors based on multilayer PtSe₂/perovskite heterojunctions. *J Phys Chem Lett* **9**, 1185–1194 (2018).
279. Zeng LH, Chen QM, Zhang ZX, Wu D, Yuan HY et al. Multilayered PdSe₂/perovskite schottky junction for fast, self-powered, polarization-sensitive, broadband photodetectors, and image sensor application. *Adv Sci* **6**, 1901134 (2019).
280. Wang HL, Chen Y, Lim E, Wang XD, Yuan SJ et al. High-performance lead-free two-dimensional perovskite phototransistors assisted by ferroelectric dielectrics. *J Mater Chem C* **6**, 12714–12720 (2018).
281. He JG, Yang Y, He Y, Ge C, Zhao Y et al. Low noise and fast photoresponse of few-layered MoS₂ passivated by MA₃Bi₂Br₉. *ACS Photonics* **5**, 1877–1884 (2018).
282. Gu X, Cui W, Li H, Wu ZW, Zeng ZY et al. A solution-processed hole extraction layer made from ultrathin MoS₂ nanosheets for efficient organic solar cells. *Adv Energy Mater* **3**, 1262–1268 (2013).
283. Giri A, Park G, Yang H, Pal M, Kwak J et al. Synthesis of 2D metal chalcogenide thin films through the process involving solution-phase deposition. *Adv Mater* **30**, 1707577 (2018).
284. Yun JM, Noh YJ, Yeo JS, Go YJ, Na SI et al. Efficient work-function engineering of solution-processed MoS₂ thin-films for novel hole and electron transport layers leading to high-performance polymer solar cells. *J Mater Chem C* **1**, 3777–3783 (2013).
285. Najafi L, Taheri B, Martín-García B, Bellani S, Di Girolamo D et al. MoS₂ quantum dot/graphene hybrids for advanced interface engineering of a CH₃NH₃PbI₃ perovskite solar cell with an efficiency of over 20%. *ACS Nano* **12**, 10736–10754 (2018).
286. Akama T, Okita W, Nagai R, Li C, Kaneko T et al. Schottky solar cell using few-layered transition metal dichalcogenides toward large-scale fabrication of semitransparent and flexible power generator. *Sci Rep* **7**, 11967 (2017).
287. Wang DA, Elumalai NK, Mahmud MA, Yi HM, Upama MB et al. MoS₂ incorporated hybrid hole transport layer for high performance and stable perovskite solar cells. *Synth Met* **246**, 195–203 (2018).
288. Kim YG, Kwon KC, Le QV, Hong K, Jang HW et al. Atomically thin two-dimensional materials as hole extraction layers in organolead halide perovskite photovoltaic cells. *J Power Sources* **319**, 1–8 (2016).
289. Kakavelakis G, Paradisanos I, Paci B, Generosi A, Papachatzakis M et al. Extending the continuous operating lifetime of perovskite solar cells with a molybdenum disulfide hole extraction interlayer. *Adv Energy Mater* **8**, 1702287 (2018).
290. Dasgupta U, Chatterjee S, Pal AJ. Thin-film formation of 2D MoS₂ and its application as a hole-transport layer in planar perovskite solar cells. *Sol Energy Mater Sol Cells* **172**, 353–360 (2017).
291. Huang P, Wang ZW, Li YF, Zhang KC, Yuan LG et al. Water-soluble 2D transition metal dichalcogenides as the hole-transport layer for highly efficient and stable p-i-n perovskite solar cells. *ACS Appl Mater Interfaces* **9**, 25323–25331 (2017).
292. Malek NAA, Alias N, Umar AA, Zhang X, Li XG et al. Enhanced charge transfer in atom-thick 2H-WS₂ nanosheets' electron transport layers of perovskite solar cells. *Sol RRL* **4**, 2000260 (2020).
293. Zhao EL, Gao LG, Yang SZ, Wang LK, Cao JM et al. *In situ* fabrication of 2D SnS₂ nanosheets as a new electron transport layer for perovskite solar cells. *Nano Res* **11**, 5913–5923 (2018).
294. Zhao XJ, Liu SS, Zhang HT, Chang SY, Huang WC et al. 20% efficient perovskite solar cells with 2D electron transporting layer. *Adv Funct Mater* **29**, 1805168 (2019).
295. Wang TY, Zheng FY, Tang GQ, Cao JP, You P et al. 2D WSe₂ flakes for synergistic modulation of grain growth and charge transfer in Tin-based perovskite solar cells. *Adv Sci* **8**, 2004315 (2021).
296. Cao JP, Tang GQ, You P, Wang TY, Zheng FY et al. Enhanced performance of planar perovskite solar cells induced by van der Waals epitaxial growth of mixed perovskite films on WS₂ flakes. *Adv Funct Mater* **30**, 2002358 (2020).
297. Liu ZY, Liu KK, Zhang FP, Jain SM, He TW et al. CH₃NH₃PbI₃: MoS₂ heterostructure for stable and efficient inverted

- perovskite solar cell. *Sol Energy* **195**, 436–445 (2020).
298. Luan BQ, Zhou RH. Wettability and friction of water on a MoS₂ nanosheet. *Appl Phys Lett* **108**, 131601 (2016).
299. Cicero G, Calzolari A, Corni S, Catellani A. Anomalous wetting layer at the Au(111) surface. *J Phys Chem Lett* **2**, 2582–2586 (2011).
300. Levita G, Righi MC. Effects of water intercalation and tribochemistry on MoS₂ lubricity: an ab initio molecular dynamics investigation. *ChemPhysChem* **18**, 1475–1480 (2017).
301. Capasso A, Matteocci F, Najafi L, Prato M, Buha J et al. Few-layer MoS₂ flakes as active buffer layer for stable perovskite solar cells. *Adv Energy Mater* **6**, 1600920 (2016).
302. Liang MY, Ali A, Belaidi A, Hossain MI, Ronan O et al. Improving stability of organometallic-halide perovskite solar cells using exfoliation two-dimensional molybdenum chalcogenides. *npj 2D Mater Appl* **4**, 40 (2020).
303. Song QJ, Wang HF, Pan XC, Xu XL et al. Anomalous in-plane anisotropic Raman response of monoclinic semimetal 1 T'-MoTe₂. *Sci Rep* **7**, 1758 (2017).
304. Lekina Y, Febriansyah B, Fan XF, You L, Morris S et al. Strong optical, electrical, and raman in-plane anisotropy in corrugated two-dimensional perovskite. *J Phys Chem C* **125**, 22630–22642 (2021).
305. Xia J, Yan JZ, Wang ZH, He YM, Gong Y et al. Strong coupling and pressure engineering in WSe₂-MoSe₂ heterobilayers. *Nat Phys* **17**, 92–98 (2021).
306. Lin KB, Xing J, Quan LN, De Arquer FPG, Gong XW et al. Perovskite light-emitting diodes with external quantum efficiency exceeding 20 per cent. *Nature* **562**, 245–248 (2018).
307. Chiba T, Hayashi Y, Ebe H, Hoshi K, Sato J et al. Anion-exchange red perovskite quantum dots with ammonium iodine salts for highly efficient light-emitting devices. *Nat Photonics* **12**, 681–687 (2018).
308. Zhao BD, Bai S, Kim V, Lamboll R, Shivanna R et al. High-efficiency perovskite-polymer bulk heterostructure light-emitting diodes. *Nat Photonics* **12**, 783–789 (2018).
309. Cao Y, Wang NN, Tian H, Guo JS, Wei YQ et al. Perovskite light-emitting diodes based on spontaneously formed sub-micrometre-scale structures. *Nature* **562**, 249–253 (2018).
310. Pospischil A, Furchi MM, Mueller T. Solar-energy conversion and light emission in an atomic monolayer p-n diode. *Nat Nanotechnol* **9**, 257–261 (2014).
311. Baugher BWH, Churchill HOH, Yang YF, Jarillo-Herrero P. Optoelectronic devices based on electrically tunable p-n diodes in a monolayer dichalcogenide. *Nat Nanotechnol* **9**, 262–267 (2014).
312. Dobusch L, Schuler S, Perebeinos V, Mueller T. Thermal light emission from monolayer MoS₂. *Adv Mater* **29**, 1701304 (2017).
313. Kong LM, Zhang XY, Li YG, Wang HR, Jiang YZ et al. Smoothing the energy transfer pathway in quasi-2D perovskite films using methanesulfonate leads to highly efficient light-emitting devices. *Nat Commun* **12**, 1246 (2021).
314. Jiang YZ, Cui MH, Li SS, Sun CJ, Huang YM et al. Reducing the impact of auger recombination in quasi-2D perovskite light-emitting diodes. *Nat Commun* **12**, 336 (2021).
315. Quan LN, Ma DX, Zhao YB, Voznyy O, Yuan HF et al. Edge stabilization in reduced-dimensional perovskites. *Nat Commun* **11**, 170 (2020).
316. Li TT, Guo W, Ma L, Li WS, Yu ZH et al. Epitaxial growth of wafer-scale molybdenum disulfide semiconductor single crystals on sapphire. *Nat Nanotechnol* **16**, 1201–1207 (2021).
317. Lin HH, Zhu Q, Shu DJ, Lin DJ, Xu J et al. Growth of environmentally stable transition metal selenide films. *Nat Mater* **18**, 602–607 (2019).
318. Rogalski A, Kopytko M, Martyniuk P. Two-dimensional infrared and terahertz detectors: outlook and status. *Appl Phys Rev* **6**, 021316 (2019).
319. Ubrig N, Ponomarev E, Zultak J, Domaretskiy D, Zólyomi V et al. Design of van der Waals interfaces for broad-spectrum optoelectronics. *Nat Mater* **19**, 299–304 (2020).
320. Park NG, Zhu K. Scalable fabrication and coating methods for perovskite solar cells and solar modules. *Nat Rev Mater* **5**, 333–350 (2020).
321. Han JH, Kwak M, Kim Y, Cheon J. Recent advances in the solution-based preparation of two-dimensional layered transition metal chalcogenide nanostructures. *Chem Rev* **118**, 6151–6188 (2018).
322. Shi L, Bucknall P, Young TL, Zhang M, Hu L et al. Gas chromatography-mass spectrometry analyses of encapsulated stable perovskite solar cells. *Science* **368**, eaba2412 (2020).
323. Khenkin MV, Katz EA, Abate A, Bardizza G, Berry JJ et al. Consensus statement for stability assessment and reporting for perovskite photovoltaics based on ISOS procedures. *Nat Energy* **5**, 35–49 (2020).
324. Xiao K, Lin RX, Han QL, Hou Y, Qin ZY et al. All-perovskite tandem solar cells with 24.2% certified efficiency and area over 1 cm² using surface-anchoring zwitterionic antioxidant. *Nat Energy* **5**, 870–880 (2020).
325. Lin RX, Xiao K, Qin ZY, Han QL, Zhang CF et al. Monolithic all-perovskite tandem solar cells with 24.8% efficiency exploiting comproportionation to suppress Sn(II) oxidation in precursor ink. *Nat Energy* **4**, 864–873 (2019).
326. Manzeli S, Ovchinnikov D, Pasquier D, Yazyev OV, Kis A. 2D transition metal dichalcogenides. *Nat Rev Mater* **2**, 17033 (2017).
327. Klein A, Jaegermann W. Review—electronic properties of 2D layered chalcogenide surfaces and interfaces grown by (quasi) van der Waals epitaxy. *ECS J Solid State Sci Technol* **9**, 093012 (2020).
328. Park NG. Perovskite solar cell: research direction for next 10 years. *ACS Energy Lett* **4**, 2983–2985 (2019).
329. Yuan J, Liu HL, Wang SR, Li XG. How to apply metal halide perovskites to photocatalysis: challenges and development. *Nanoscale* **13**, 10281–10304 (2021).
330. Madi M, Tahir M, Tasleem S. Advances in structural modification of perovskite semiconductors for visible light assisted photocatalytic CO₂ reduction to renewable solar fuels: a review. *J Environ Chem Eng* **9**, 106264 (2021).
331. Wang F, Liu XY, Zhang ZG, Min SX. A noble-metal-free MoS₂ nanosheet-coupled MAPbI₃ photocatalyst for efficient and stable visible-light-driven hydrogen evolution. *Chem Commun* **56**, 3281–3284 (2020).
332. Park Y, Lee S, Park HJ, Baac HW, Yoo G et al. Hybrid metal-halide perovskite-MoS₂ phototransistor. *J Nanosci Nanotechnol* **16**, 11722–11726 (2016).
333. Chandrasekar PV, Yang SY, Hu JM, Sulaman M, Saleem MI et al. A one-step method to synthesize CH₃NH₃PbI₃: MoS₂ nano-hybrids for high-performance solution-processed photodetectors in the visible region. *Nanotechnology* **30**, 085707 (2019).

334. Li ZB, Li JN, Ding D, Yao HZ, Liu L et al. Direct observation of perovskite photodetector performance enhancement by atomically thin interface engineering. *ACS Appl Mater Interfaces* **10**, 36493–36504 (2018).
335. Zhang LW, Shen SL, Li M, Li LY, Zhang JB et al. Strategies for air - stable and tunable monolayer MoS₂ - based hybrid photodetectors with high performance by regulating the fully inorganic trihalide perovskite nanocrystals. *Adv Opt Mater* **7**, 1801744 (2019).
336. Sun B, Xi S, Liu ZY, Liu XY, Wang ZY et al. Sensitive, fast, and stable photodetector based on perovskite/MoS₂ hybrid

film. *Appl Surf Sci* **493**, 389–395 (2019).

337. González-Carrero S, Galian RE, Pérez-Prieto J. Organometal halide perovskites: bulk low-dimension materials and nanoparticles. *Part Part Syst Charact* **32**, 709–720 (2015).

Acknowledgements

J. H. Teng acknowledges A*STAR for funding support in Grants A20E5c0084, A2083c0058 and CRF SC25/21-110318.

Competing interests

The authors declare no competing financial interests.